Tip Leakage Flow Downstream of a Compressor Cascade with Moving End Wall

Yu Wang

Thesis submitted to the Faculty of the Virginia Polytechnic Institute and State University
in partial fulfillment of the requirements for the degree of

Masters of Science
In
Aerospace Engineering

William J. Devenport, Chair
Joseph A. Schetz
Roger L. Simpson

February 20, 2000
Blacksburg, Virginia

Tip Leakage Flow Downstream of a Compressor Cascade With Moving End Wall

Yu Wang

(ABSTRACT)

A large-scale moving end-wall system has been designed and built at the Aerospace and Ocean Engineering Department of Virginia Tech. This system forms part of a low-speed linear compressor cascade wind tunnel, where it is used to simulate the effects of the relative motion between the blade tips and casing upon the flow. Detailed 4-sensor hot wire measurements were made at various locations downstream the cascade. The results are presented in term of mean flow field and turbulence flow field. In order to reveal the effects of moving end wall, the results also compared with the results obtained with stationary end wall.

Acknowledgements

I want to specially thank my advisor, and mentor, Dr. William J. Devenport for his support and guidance in the pass years. I don't know how to express my feelings. I think I'm very lucky to have the opportunity to work with him.

I would like to my friend Ruolong Ma, who helped me taking data in the noise tunnel during the most difficult periods. And Chittappa Mutthanna and Semere Bereketab who gave me a lot of help in the lab during the past 3 years.

I would also like to thank Dr. Joesph A. Schetz and Dr. Roger L. Simpson, as my committee members, they gave me a lot of valuable suggestions to my thesis. Dr. Schetz also let us use his motor controller, which help us a lot.

I will never froget the people in AOE workshop, Greg Dudding, Kent Morris , Gary Stafford and Brus Stanger. Their great job and experience help me to make the moving wall running.

Finally, I want to express my gratitude to my wife, Haiyuan, without her love and emotional support, I will never achieve my goals.

This study was made possible with support from NASA Langley through grant number NAG-1-1801 under the supervision of Dr. Joe Posey.

The experience of study in AOE gave me so much benefits, I will never forget our Lab 7 in my entire life.

Yu Wang

Table of Contents

Chapter 1 Introduction

The flow field inside the rotors of aircraft engines is very complex and is a subject of much research. The understanding of such flows is important to both aerodynamic theory and high performance aircraft engine design. Many parts of the engine flows are dominated by tip leakage flows. Due to the clearance between the rotor blades and casings, the tip leakage flow is driven by the pressure difference between the pressure side and suction side of the blade. In some cases, the tip leakage flow may roll-up and form a discrete vortex. In a typical turbofan (figure 1-1), the tip leakage flow could be found in fan, compressor and turbine flow fields. The tip leakage flow has some important effects on the performance of aircraft engines. For example, it produces a substantial proportion of the total loss. The flow field downstream of a rotor is strongly influenced by tip-leakage vortices and the interaction between these vortices and the surrounding flows can be a significant source of noise (e.g. Hanson *et al* 1997). In a typical turbofan, with an upstream rotor and downstream stator, non-uniform flow in the rotor wake impinging on the stator generates much of the noise radiated by the engine. In such cases, the random turbulent components generate broadband noise. To accurately predict this broadband noise, detailed knowledge of the turbulence flow field downstream the compressor rotor is needed. Tip leakage flows are very complicated by their interaction with the passage flow and the boundary layer developed from the end wall. With the rapid progress of computer and CFD technologies in recent years, many researchers have tended to use numerical investigation to solve this problem. But currently, the turbulence structure generated by this phenomenon is not well understood and remains difficult to predict. Experimental study still plays an important role in the study of tip leakage flows. It can give us detailed views of the fundamentals of such flow phenomena, and can also provides valuable data to establish and modify the models used in numerical investigation.

Most experimental studies of tip-leakage vortices described in open literature have used either a linear cascade with stationary end wall or a rotating configuration. . Linear cascades produce vortices that are fixed in the laboratory frame of reference and

that are large enough to be probed in detail using conventional instrumentation. Figure 1-2 is a simple presentation of the linear cascade flow filed. Storer *et al* (1989) used a five-blade compressor cascade. The chord of blade was 300mm, the Reynolds number based on the chord length was 5×10^5. The velocity field inside the passage was measured by a five-hole probe. The results showed the relationship between the tip leakage flow and the total pressure loss. An apparently optimum tip clearance size between 0.5% and 1.0% was observed. At large tip clearance (2% chord), the secondary flow vector showed clear circular motion around the vortex core.

Kang et al (1993) built a linear compressor cascade with seven NASA 65-1810 blades. The Reynolds number based on the chord length and inflow was 2.9×10^5. A Five-hole probe was used to make measurements at 16 traverse planes from 7.5% chord upstream of the leading edge to 50% chord downstream the trailing edge. To reveal the effects of the tip gap size, three different tip clearances (1.0, 2.0 and 3.0 percent of chord) are used. In their results, the tip-leakage vortex was seen as have distinctive core both in the secondary velocity vectors and the total pressure coefficient contours. At small clearance, a weak horseshoe vortex was formed from the blade leading edge, and two other small vortices that developed from the separation of the pressure and suction side were observed in the tip region. It was also found that the vorticity of the tip leakage vortex increases rapidly near the leading edge and reaches it highest values at a short distance downstream of the leading edge. From this point, the vorticity gradually decreases toward the exit and the downstream. The circulation of tip-leakage vortex increases along with the increasing of tip clearance. As the tip leakage vortex travels to downstream, the vortex center moves away from both the end wall and the blade suction side surface.

Even though the linear cascade reveals some important characteristics of tip leakage flows, experimental studies with rotors show significant differences between the linear cascade flow and the rotor flow. In linear compressor cascade with tip clearance, the tip leakage flow almost always rolls-up and forms discrete tip leakage vortex. In rotors, the situation is much different. Lakshminarayana *et al* (1995) compared several experimental investigations that used different rotor configurations. It was found that a lot of parameters might influence the formation of tip leakage vortex in rotors. Some of

them are: configuration (single stage, rotor alone), inlet flow turbulence, wall boundary layer thickness, tip clearance, Reynolds number, etc.

Davino *et al* (1982) made tri-axial hot-wire probe measurement to get the three velocity components and the turbulence information in a single stage compressor rotor. The rotor has modified NASA 65 series blades with tip chord 15.41cm. The tip clearance was 0.245cm. In his results, a concentration of high turbulence intensity region was observed where the tip leakage flow roll-up and interaction with the case boundary layer and passage flow. The interference region (the region occupied by tip-leakage vortex) was also observed to grow with axial distance. Most of the turbulence intensity components decay to nearly free-stream values within half-a-chord downstream of the rotor blade trailing edge.

Lakshminarayana and Pandya *et al* (1984), used stationary two sensor hotwire probe in the same experiment facility as Davino *et al* (1982). The inlet velocity was 28.37m/s (design condition) and 26.28m/s (off condition), the blade tip speed was 51.5m/s and 43.8m/s respectively. The measurements presented that the local lift coefficient or pressure difference that was modified under off-design condition had a significant effect on the leakage velocities in the rotor. It was concluded that in order to understand the leakage flow and the formation of tip leakage vortex, it was essential to carry out detailed three-dimensional measurement by nonintrusive techniques in the gap region as well as away from it.

The same facility mentioned above was also used in Lakshminarayana and Zhang *et al* (1987) with a laser Doppler Velocimeter (LDV) and a Kiel probe to study the flow with two different tip clearance heights. The leakage flow tended to roll up to form a discrete vortex at larger tip clearance, but in both cases, no discrete tip leakage vortex was observed downstream the rotor.

In the experimental study in Lakshminarayana and Zaccaria et al (1995) in the same facility. A five-hole probe was used with a rotating-probe traverse mechanism that allowed a circumferential traverse to be done. The data show intensive mixing between the tip leakage flow and the passage flow but it didn't show a clear circular flow pattern in the tip leakage flow region.

Inoue et al (1988) used a rotor-alone configuration. The rotor had NASA 65 series blades, the chord at the tip was 224.5mm. The rotation speed was 1300rpm which achieved the blade tip speed 30m/s. Instead of using probe in a rotating frame, they used single hotwire probe that was fixed on the casing. Ensemble-average and phase-locked measurements technology were used to get the flow pattern in the tip gap and downstream of the rotor. In order to obtain the three-component velocity vector with single hotwire probe, the probe was rotated on its axis at 20 different positions at each survey plane. From the phase-locked flow patterns, the circular motion pattern if the tip leakage vortex was clearly defined. As the tip clearance increases, a stronger leakage vortex comes into existence at a more downstream location. The centrifugal force in the boundary layer on the pressure surface did not appear since outward flow was not observed over a large portion of the suction surface.

Stauter *et al* (1993) used two-color, five-beam LDV system to make three-component velocity measurements in a two-stage axial compressor model. Measurements were made at 18 different axial locations both inside the passage and downstream the second stage rotor (axial position 0.42 axial chord to 1.297 axial chord from the blades leading edge). From the crosswise vectors, the roll-up and the tip leakage vortex center were well defined but the center of the axial velocity deficit did not coincide with the apparent center of the vortex rollup.

The different behavior of tip leakage flows in linear cascades and rotors suggest that the linear cascade does not simulate all the significant features of an actual turbomachinery. For the formation and development of tip-leakage vortices the most important omission is probably the relative motion between the blade tips and the end wall. Because the tip-leakage vortex is generated and developed in the region adjacent to the end wall, it is reasonable to think that the interaction between this vortex and the boundary layer generated by the moving end wall may play an important role in the generation and development of downstream turbulence structure.

One way of improving linear cascade models is introducing relative motion between the blade and end wall. Graham et al (1985) used a water tunnel with linear turbine cascade and moving end wall. The cascade consisted of 5 transparent Plexiglas blades. A smooth rubber belt driven by a compressed air motor ran beneath the blades to

simulate blade-shroud relative motion. The width of the belt just covered the section from the blades' leading edge plane to the trailing edge plane. The gap flow was observed with dye injection. From his results, it was found that increasing the belt speed reduced the clearance flow, and at tight clearances (1.2% or 0.6%), leakage flow could be cut off by increasing the belt speed.

Yaras and Sjolander (1992) used a 5-blade linear turbine cascade with blade chord of 250mm. A smooth synthetic rubber belt ran beneath the blades. The belt was 22.7" wide and extended 120mm (0.48 chord lengths) upstream of the leading edge plane and 255mm (1.02 chord lengths) downstream of the trailing edge plane. An AC motor drove the belt with a variable-frequency controller and the maximum tangential speed was about 19m/s. By comparing the results between moving and stationary end wall a substantial decrease in the gap flow rate was found as a result of the wall motion. At the test condition matching the flow coefficient of the actual turbine, the reduction was about 50 percent. This tip-gap flow rate reduction is due to a general reduction in the pressure difference driving the fluid into the gap. From their further research into the structure of the downstream flow field (Yaras *et al.*, 1992), it was found the strength of tip vortex was reduced considerably with the introduction of wall motion. The passage vortex adjacent to the tip-leakage vortex was enhanced by the scraping effect of the blades on the end-wall boundary layer. Another phenomenon observed was the dragging of the two vortices toward the suction side of the passage, partly blocking the tip-gap. This blockage seems to raise the pressure at the gap outlet, thereby reducing the pressure difference for the leakage flow.

In a compressor cascade, the direction of rotation is opposite to that for turbines and is in the same direction as the tip-leakage flow. One might therefore expect the tip-leakage vortex to be intensified and shifted toward the pressure side of the passage. However, we are unaware any previous studies using moving end walls in linear compressor cascade tunnels. Furthermore, most previous studies of compressor tip-leakage vortices have been restricted to mean-flow measurements, and there is not much understanding of turbulence structure, particularly at downstream of the blades where noise generation occurs.

The present study is part of broader program of research being conducted into the turbulence structure of flow downstream of a linear compressor cascade with tip leakage (Muthanna *et al*, 1998, Wenger *et al*, 1999). Detailed three-component velocity, turbulence, spectral measurements and flow visualization have been performed at a number of downstream positions and various tip clearances with a stationary end wall. Muthanna (1998) provided the detailed results and discussion of mean flow and turbulence flow fields.

The present study as performed in the same linear cascade wind tunnel facility, but the stationary end all has replaced by a newly designed moving-wall system to simulate the relative motion between the blade tip and the engine casing. This study is intended to complement Muthanna and Wenger's investigations by investigating the influence of relative motion on the tip leakage flow phenomenon and also to provide data use for the development and testing prediction schemes. The application of our measurements is to the development of the fan wake flow in large bypass ratio engines and its potential for the generation of noise through interaction with the stator vanes.

Chapter 2 Apparatus and Instrumentation

The Virginia Tech Low Speed Cascade Wind Tunnel was used. This facility was built for the compressor-cascade studies of Muthanna (1998). The stationary end wall used by Muthanna was replaced by a moving end wall system to simulate the relative motion between the compressor blade tip and the engine case. Detailed measurements of the flow field downstream of the cascade were made by using hot wire anemometry.

2.1 The Linear Compressor Cascade

Figure 2-1 is the picture of the test section of the Virginia Tech Low Speed Cascade Wind Tunnel. Figure 2-2 shows the layout and dimensions of the linear compressor cascade. This wind tunnel is driven by a centrifugal fan, which is powered by a 15hp AC motor. Air from the fan passes through a diffuser, a settling chamber and a 3.88:1 contraction before entering the 30"×12" rectangular section that guides the flow onto the cascade. Flow at the test section entrance is closely uniform with a variation in velocity of 1% across the section and of low turbulence intensity of 0.2%. The cascade (figure 2-3) consists of 8 cantilevered GE rotor B section blades mounted on a structure built into the upper section that allows individual adjustment of each tip gap height. Table 2-1 lists the blade section coordinates normalized on chord, figure 2-4 shows the shape of blade section. The blades are fabricated from aluminum and have a chord of 10" and an effective span of just under 10" (figure 2-5). The cascade configuration has a rectangular cross section of 65" ×10". The blade spacing is 9.29". The stagger angle of the cascade is 56.93°. The inlet angle of the cascade is 65.1°. The blade tip gaps are adjustable, the design tip gap being 1.65% of the chord, or 0.165". The approach free steam velocity was 26m/s (measured by Pitot static probe mounted at upstream section), giving a Reynolds number of about 400,000 based on the chord and approach free stream velocity. Just upstream of the cascade, 1-inch high suction slots (figure 2-6) on the upper and lower end walls remove the relatively thick boundary layers growing here. The new,

Table 2-1: Blade Co-ordinates (normalized on chord)

Lower surface		Upper surface	
x/c	y/c	x/c	y/c
0.000000	0.000000	0.000000	0.000000
0.000435	0.000596	0.000060	-0.001491
0.001413	0.001047	0.000923	-0.003169
0.002926	0.001323	0.002598	-0.005009
0.004966	0.001388	0.005091	-0.006975
0.007524	0.001209	0.008414	-0.009021
0.010599	0.000777	0.012579	-0.011102
0.014200	0.000137	0.017595	-0.013180
0.019048	-0.000748	0.023465	-0.015238
0.029117	-0.002550	0.030187	-0.017291
0.039178	-0.004300	0.037745	-0.019400
0.049233	-0.006001	0.045855	-0.021590
0.096961	-0.013419	0.093151	-0.033478
0.144562	-0.019783	0.140592	-0.043940
0.192059	-0.025156	0.188155	-0.053027
0.239468	-0.029599	0.235822	-0.060789
0.286809	-0.033171	0.283572	-0.067278
0.334100	-0.035929	0.331389	-0.072544
0.381356	-0.037929	0.379254	-0.076640
0.428588	-0.039220	0.427156	-0.079613
0.475794	-0.039826	0.475098	-0.081487
0.522983	-0.039750	0.523069	-0.082262
0.570167	-0.038991	0.571058	-0.081938
0.617353	-0.037568	0.619059	-0.080492
0.664516	-0.035603	0.667097	-0.077670
0.711679	-0.032997	0.715151	-0.073277
0.758887	-0.029596	0.763179	-0.067158
0.806192	-0.025241	0.811130	-0.059163
0.853654	-0.019769	0.858947	-0.049143
0.901342	-0.013007	0.906564	-0.036954
0.949328	-0.004778	0.953911	-0.022461
0.959464	-0.002843	0.963827	-0.019107
0.969617	-0.000834	0.973727	-0.015645
0.979787	0.001253	0.983610	-0.012072
0.989977	0.003419	0.993477	-0.008389
0.993047	0.004088	0.996438	-0.007260
0.997043	0.003561	0.999467	-0.004667
1.000000	0.000000	1.000000	0.000000

tangentially uniform, boundary layers that grow from the suction slot leading edges are tripped by a boundary layer trip (0.38”-wide strip of 0.02”-diameter glass sanding beads spread in a single layer) located at 5.34” upstream from the blades leading edge line (2.25” axially). The thickness of this boundary layer is about 0.25” as it crosses the leading edge plane of the cascade midway between the blades. Similar boundary layer trips, 0.25” wide, were attached 1” downstream of the leading edges of the blades to eliminate any unsteadiness or non-uniformity that might result from natural transition here.

The angles of the wind-tunnel sidewalls downstream of the cascade are adjustable, enabling the turning angle of the flow to be set so as to eliminate any net tangential pressure gradient. A turning angle of 11.5^{o} eliminated almost all this pressure gradient and produced a closely periodic flow through and downstream of the middle three passages of the cascade (see section 2.7). Screens attached to the downstream end of the test section (figure 2-7) were used to raise the pressure in the test section above atmospheric to ensure the proper operation of the boundary layer suction slots. Further details of the cascade and wind tunnel are given by Muthanna *et al*, 1998.

2.2 The Moving Wall System

The moving wall system was designed to fit into the cascade tunnel and replace the stationary wall with the minimum re-construction of the cascade wind tunnel itself. To completely cross the 7 flow passages and clear the test section structure, the upper surface of the moving belt had to be at least 175" long. In order to extend at least two-chord lengths axially downstream of the trailing edge plane of the blades as well as a short distance upstream (to provide some skew in the inlet boundary layer), the belt had to be at least 27" wide (figure 2-9). To simulate the rotational speed of the compressor rotor being modeled, the wall speed had to match the tangential velocity of the free stream (figure 2-9). The terms tangential and axial are used here to mean parallel and perpendicular to the leading edge plane respectively, by analogy with an actual turbomachine. With a free stream velocity of 26m/s, the belt speed is $26.0 \times cos 24.9° = 23.6$m/s. The belt vibration had to be minimal compared to the tip gap, and a moving wall

system that could be run continuously over a 2 hours period (typical time taken for a complete set of hot-wire measurements in one plane) was needed.

Basically, the moving wall system is a moving belt driven by rollers and supported by a slide bed. Figure 2-8 is a schematic of the moving wall system installed in the wind tunnel. To provide the passage for the moving belt, two gaps are made between sidewall and the moving wall surface. The height of these gaps is 0.25", the gap length is 42" measured from the trailing edge line of blades

2.2.1 Main Frame

The rollers are mounted on a steel frame (figure 2-10). The main frame of the moving wall system is a 184'×36" rectangle frame made from welded 6'×2"×0.25" steel box section. All other parts are installed on this frame whose rigidity fixes the relative positions of the rollers. The frame is braced using 5 cross beams made of 3'×1.25'×0.25" "C"-section steel channel. Ten legs, also made from this channel, are designed to support the main frame. The distances between these legs are non-uniform in order to avoid conflicting with existing tunnel structure. During the assembly, it was found there is no enough space to mount the first leg at downstream side. So only 9 legs were used. The top of the main frame is nominally 42" from the ground. Bolts attached to the legs allowed the height of the main frame to be adjusted. These bolts can be also used to adjust the level of main frame. After adjustment, the legs are fixed to the laboratory floor using 3/8" anchors to reduce the vibration of the whole system.

2.2.2 Moving Belt

The choice of the belt material is very critical. Yaras and Sjolander (1992) used synthetic rubber belt. Such belts are very durable, but they are also quite thick (>1/8") and heavy so that their inertia can make them a hazard if the belt system fails at high speed. They are also not easy to join on site, which can make installation a lengthy process. In our system we chose instead to use belts fabricated from Mylar film. This kind of film is inexpensive and available in various thickness and widths. The 0.01" thick film, which we chose, has very high tensile strength and low flexibility under tension. This characteristic is important to keep the belt tracking at high speed. The mass of the

belt is much smaller than the rubber belt, so it carries much less momentum and risk. An important advantage of the Mylar belt is that it can easily be joined after it is installed on the roller system. To join the belt, two ends of the belt are over-lapped by 1.5", and welded using a soldering iron at several hundred of points (figure 2-11). The welding points are 3 to 4mm in diameter, the two ends of belt are melt together at these points and give high strength to shear stress. This join is easily peeled, so scotch tape is used to cover the joint surface. It takes about 2 hours to build and install a new belt by this method.

The joint region of the belt is 0.02" thick and 1.5" wide. The overlapped region is only about 0.5% of the whole belt length. The overlap makes a 0.01” step, which is 6% of the tip-gap size. This step may introduce some disturbance to the flow field.

The windward edge of the belt, which lies just upstream of the leading edge plane of the cascade, is protected using a 1.25"-wide cover made of 0.005"-thick Mylar film (Figure 2-9). The cover prevents the edge of the belt from being lifted by the oncoming flow, at the cost of a 0.005"- step experienced by the end-wall boundary layer as it flows from the stationary to moving sections of the end wall. Figure 2-10 is the picture of moving wall system installed in the cascade wind tunnel.

2.2.3 Rollers

Two 8"-diameter 30”-wide high-procession rollers manufactured by Timesavers Inc. were mounted at either end of the frame. These type of rollers are commonly found in industrial sanding machines, where they are used to propel sanding belts of similar dimensions and at similar speeds to the present moving end wall. Both rollers were dynamically balanced at 2000rpm by the manufacturer. The drive roller (top right of figure 2-8) has a flat surface lagged by 0.2-inch thick rubber. The driven roller has a 3/1000" crown at its center to improve the tracking capability of the belt. The drive roller is mounted on a pair of SealMaster® RPB-208-4 split bearings. The driven roller is mounted on a pair of SealMaster® 12T2000D take-up bearings and a Dodge® CP400 take-up frame (figure 2-12). The adjustment nuts on the frame are used to set the tension of the belt during operation.

2.2.4 Slider Bed and Belt Suction

A slider bed (platen) is used to support the belt as it passes underneath the blade tips and maintain the size of tip-gap. The plat was originally to be built from high-density polyethylene (HDPE) – a material similar to Teflon. Initial tests, however, showed that the HDPE had a tendency to bond to the Mylar belt at higher speeds and so a ¾"-thick fin-form plywood bed was used instead. This kind of plywood has an epoxy finished smooth surface, is easy to machine and generates relatively little static electricity when using a plastic belt.

A commonly used method to hold a moving belt flat is by using suction. Yaras and Sjolander (1992) built a suction box on the back of their slider bed. In our configuration this was unnecessary because the screens at the test section exit already provided sufficient pressure difference across the bed. With screens, the pressure difference inside and outside the tunnel is 0.154 inch of water. To make use of this pressure difference, some 80 suction grooves were cut into the upper surface of the bed. The layout of the grooves is figure 2-12. 1/8" diameter holes were drilled through the plate to connect the grooves to ambient (figure 2-13). The upstream parts of the 7 long grooves (roughly parallel to the downstream flow direction) begin near the pressure side of blades and extend to downstream. These grooves are designed to dampen the belt vibration and maintain the tip gap size. The running test showed that these grooves are unnecessary except the one near blade 2. And too much suction will introduce large fraction drag and reduce the lifetime of the belt. So these long grooves (except the one near blade 2) were blocked by taping the holes underneath of the bed.

2.2.5 Belt Drive and Speed Control

The belt is driven by a 15HP AC synchronous motor. The power transmission from the motor to the drive roller is accomplished using a pair of Browning® 32HQ200 gear belt pulleys and a 2-inch wide Goodyear® gear belt that could transfer up to 30horsepower. The transmission ratio between the shafts of motor and driving roller is 1:1. The gear belt transmission doesn't need precision adjustment and so only a simple motor base is needed.

A TOSHIBA® Tosvert-130G2+ digital variable-frequency motor controller is used to control the motor speed. The output frequency of the motor controller can be varied from 0 to 83Hz, corresponding to roller rotation speeds of up to 2420rpm and linear belt speeds of up to 25.7 m/s. Figure 2-13 shows the motor and motor controller.

2.2.6 Belt speed measurement – the speed meter

A speed meter was developed to measure the moving wall speed directly. Figure 2-14 is the schematic of the circuit. The speed meter has two modules: the sensor module and processing module. The sensor module includes an infrared LED, an infrared photo diode and an OP-amplifier and Schmitt trigger. The sensor module is installed about 0.5" above the belt surface. The LED emits infrared light to the belt. The light reflected from the belt surface is picked up by the photodiode. This signal is amplified and output to a Schmitt trigger. Two plastic mirrors made from pieces of discarded CD-ROM discs are glued on the surface of the belt. The mirrors are ¼" wide, 1.5" long and 0.05" thick. The distance between the mirrors is measured. When properly adjusted (by adjusting the distance between sensor and belt surface, or adjusting the gain of amplifier), the Schmitt trigger outputs two narrow pulses when the mirror pair passes. The belt speed can then be obtained by measuring the time between these two pulses. In the processing module, these two pulses are transferred to a single pulse by using a D flip-flop (edge triggered). The width of this pulse is measured by counting a clock signal. This clock signal is generated by a high-precision 1.544MHz quartz oscillator and a "divide by 16 circuit" (i.e. the counting signal has a frequency of 96.5kHz). The counted number is displayed on the front panel by 3 LED 7-segment displays. Figure 2-15 is the picture of the speed meter. As designed, this speed meter gives a timing read-out once every 5 revolutions of the belt. The processing module doesn't convert the countered clock pulse numbers to the belt speed but this is easily obtained from the relationship

$$V_{belt} = \frac{D_{morrors} \times f_{clock}}{N}$$

In which:

V_{belt} – The speed of moving belt (in m/s)

$D_{morrors}$ – The distance between the two mirrors (in m)

f_{clock} – The frequency of counter clock (96.5kHz)

N – The Read-out of the counter

This speed meter also provides two interfaces with the laboratory computer. One is a 16-bit parallel data port. The data format is table 2-2. Bit 0 to 11 is the binary value of the clock counter. Bit 14 and 15 are two status bits. Bit 14 is 1 when the counter is being reset. Bit 15 is 1 when the counter is counting the clock pulses. So the data in bit 0 to 11 is valid only when both Bit 14 and 15 are 0. The other is a BNC connector that outputs the signal direct from the optical sensor module. The first signal is used as the belt-speed measurement. The second could be sampled and recorded along with hot-wire signals to provide a record from which the relative position of the sensor, mirrors, the belt joint and hot-wire probe can be inferred. This signal could used to eliminate hot-wire measurements made over the belt join during data processing (although that was not done in this study).

Table 2-2 The data format of speed meter output

bit 15 bit 0

REST	CONT	0	0	A11	A10	A9	A8	A7	A6	A5	A4	A3	A2	A1	A0

2.3 Operation of the Moving-Wall System

2.3.1 Start, Speed up and Tracking Control

The operation of the moving wall system includes adjustment and monitoring of the belt tracking. The belt speed is controlled by a digital motor controller. The belt position is maintained by adjusting the tension on the two sides of the belt using the take-up bearings.

The belt tracking is particularly difficult to maintain when the belt is being accelerated to or decelerated from its operating speed. We found it necessary to gradually speed up the belt in steps of about 10% of its final speed in order to maintain control of the belt tracking. In practice, it takes 4-5 minutes to speed up the belt from 0 to 23.5m/s. The belt speed is read from the speed meter.

The suction applied using the grooves in the slider bed holds the belt flat but also causes a great deal of drag on the belt. The friction force between the drive roller and the belt must be large enough to overcome this drag, and the belt strength has to be sufficient to overcome the resulting tension (hence the choice of 0.01" Mylar, as opposed to smaller). With the belt running, the abrasion of the Mylar belt on the slider bed produces some fine powder. This powder becomes coated on the drive roller's rubber surface and can reduce the friction factor between the drive roller and belt. This effect can be countered by spraying the drive roller with a standard belt dressing (e.g. Prestone® Belt Dressing) before installation of the belt. The belt dressing can be applied on the roller and continues to be effective for 1 or 2 hours. Any surplus dressing should be removed before operation of the belt, to prevent the slider bed from becoming coated and producing unnecessary drag.

We were concerned that the friction with the Mylar belt would generate large amounts of static electricity (the system does bear resemblance to a large Van de Graaf generator). Static electricity can damage instrumentation and is a fire hazard. However, for whatever reason, we found that grounding of the main frame and rollers and the use of the plywood slider bed (as opposed to the HDPE version) reduced the static electricity build up on the belt passing over the slider bed to undetectable levels. Some static electricity build up is produced on the return side of the belt but this remains at safe levels.

2.3.2 Safety Issues

The large scale and high speed make the moving wall system a danger both to the human body and the expensive hot wire probes used. The following safety precautions should be followed:

(a) The rotating parts of moving wall, such as pulleys, gear belt, must be covered.

(b) Inspect the tunnel and make sure nothing left inside the tunnel before starting the moving wall.

(c) The wind tunnel must be on during the moving wall running at high speed. The reason is that without the suction effect applied by the flow the belt will jump vertically and may hit the blade tip or sidewall.

(d) For the same reason as (c), the back screen must be in position when the moving wall is running.

(e) To avoid damaging the hot wire probe, the height between the probe and the moving wall surface should not less than 0.2".

(f) The probe should be at least 5" above the moving wall during the wall speed up and stop.

(g) The belt tracking should be monitored at all times.

2.4 Characteristics of the moving-wall system

2.4.1 Belt vibration

The amplitude of the belt vibration as it passes underneath the blade tips was measured by imaging the tip of one of the center blades (blade 5) and its reflection in the belt. Any vertical motion of the belt is apparent in vertical motion of the reflection. Initially a cathetometer was used to measure the belt vibration in this way, but the amplitude of the vibration was found to be smaller than the resolution of this device (<50 microns). A camera with magnifying lenses was therefore used to take close-up pictures of the tip reflection. Some 30 pictures were taken with an exposure time of 1/500 second, during which the belt would have moved about 5cm horizontally. Figure 2-17 is a typical picture from this set illustrating the blade tip, its reflection and the instantaneous tip gap. A high-resolution film scanner (2400dpi) was used to scan the negative films and measure the tip-gap size by counting the image pixels. Averaging tip gap measurements from the complete set of photographs we estimate the r.m.s. amplitude of vibration to have been 0.0022±0.0004", approximately 1.3% of the design tip-gap of 0.165". Figure 2-18 is a picture taken with the belt running but wind tunnel turned off (i.e. without belt suction) The belt is lifting by about 35% of the tip-gap size illustrating the necessity of suction.

2.4.2 Belt speed stability

Belt speed stability was not found to be a significant problem once we had begun to use the belt-dressing compound on the drive roller. Over a typical run time of 1.5 hours

the belt-speed (measured using the speed meter, see above) was found to vary by about ±0.1%.

2.4.3 Belt surface temperature

Belt temperature is another issue of concern. Heat is generated by the friction between the belt and the slider bed. If the temperature of belt surface were to rise significantly, it would generate a thermal boundary layer disrupting hot-wire measurements, and possibly altering the tip leakage flow. Two thermocouples mounted above the belt some 6" upstream of its leeward side to sense any temperature gradient in the flow produced by belt heating. One thermocouple was mounted 0.1" above the belt surface (well within any likely thermal boundary layer), the other was placed in the main stream 5" above the belt surface. Table 2-3 lists the results of temperature measurements. There appears to be no significant temperature difference due to belt heating. Indeed the belt remains cool to the touch even after extended periods of operation.

Table 2-3 Temperature Measurements

Time of Belt Running(min)	0.1" station (°F)	0.5" station(°F)
0*	79.1	79.0
5	80.3	80.1
10	80.3	80.2
15	80.4	80.2
20	80.5	80.3
25	80.6	80.4

*-- Both the Wind tunnel and the Moving wall are off

2.5 Hot wire Probe and Hotwire Anemometry

Two types of hot wire probe were used in the experiments. The TSI model 1218-T1.5 single hotwire probe is a right angle probe used to take the boundary layer

measurements. The four-sensor hotwire probe (type AVOP-4-100) manufactured by Auspex Corporation is used to measure the three-component velocity and velocity fluctuation. Figure 2-19 is the diagram of the four-sensor probe. The probe is a miniature Kovaznay type probe with four sensors arranged in two orthogonal X-wire arrays on eight stainless steel prongs. Each sensor is made from etched tungsten wire of 5 microns in diameter. The measurement volume for the four-sensor probe is about $0.5mm^3$.
Each sensor is operated with a Dantec 56C17/56C01 constant temperature anemoneter unit. This system could give a frequency response greater than 20kHz when optimized properly. Signals from each sensor are amplified by 10× amplifiers. A low-pass RC filter inside the amplifier limited the highest frequency less than 50kHz. Muthanna et al (1998) gave the details of the examination of frequency response. The results show that the sensors have a flat amplitude response from 0 to a 3dB point close to 22kHz.
When making the measurements in the wind tunnel, the analog signals from the hotwire anemometer are digitalized and recorded by an Analogic HSDAS-12 12 bit A/D converter board installed in a lab computer. The A/D converter board has 8 channels that allowed taking the four-sensor signals simultaneously. Velocity calibration of the probe was performed in a TSI jet calibrator using Kings Law to correlate the output voltage with the cooling flow velocity. The 3 velocity components are reduced from the 4 sensor velocities by using a lookup table obtained by direct angle calibration. Detailed description of direct angle calibration method is given by Wittmer *et al* (1998).

2.6 Traverse system

A two-axis traverse system was built specifically for the cascade tunnel. Figure 2-20 is a picture of the traverse. The traverse has two individual moving axes that allow the probe to be moved vertically and horizontally. Each axis is driven by a stepper motor manufactured by Compumotor (model S75-83-MO) and controlled by a Compumotor IF-1 3-channel stepper motor controller. The stepper motor controller communicated with the lab computer through an RS232 serial port. The resolution of programmable traverse movement is 0.001".

2.7 Cascade Calibration and Setup

Before any measurements could be made, the wind tunnel had to be calibrated. The most important issues here are the setting of the blade tip gap and of the cascade turning angle. Blade tip gap is set by adjusting each blade individually using precision gauge blocks. During adjusting care was taken to ensure that the blade remained perpendicular to the end wall, and that the distance between the blades remained equal to the norminal blade separation of 9.29". The tip gaps could be changed by adding shims under the blade support structure. Table 2-4 shows the tip gaps measured after the setup completed.

Table 2-4 Blade Tip Gaps

Blade #	Leading Edge (inch)	Mid Chord (inch)	Trailing Edge (inch)
2	0.166	0.166	0.165
3	0.165	0.166	0.167
4	0.166	0.165	0.164
5	0.165	0.165	0.165
6	0.166	0.165	0.165
7	0.164	0.166	0.166

The turning angle is defined as the angle of flow downstream of the blade row relative to the flow upstream of the blade row. When the sidewall is parallel to the downstream flow, the tangential pressure gradients across the cascade will be eliminated. To get the pressure distribution across the cascade, a Pitot-static probe was mounted on the computer-controlled traverse and was used to take measurements of the static and stagnation pressure across the cascade. The Pitot-static probe is located at plane 4.54" axially downstream of the blade trailing edge line and 0.5" and 5" above the end wall (0.092 and 0.92 of the axial chord c_a. It was found that the pressure gradient was eliminated when the sidewall turning angle was set to 11.5°. Figure 2-20 shows results of the pressure measurements in terms of the pressure coefficients defined by:

Stagnation Pressure Coefficient:

$$C_{p_o} = \frac{P_0 - P_\infty}{P_{\infty 0} - P_\infty}$$

Static Pressure Coefficient:

$$C_p = \frac{P - P_\infty}{P_{\infty 0} - P_\infty}$$

In these equations, P_0 and P are the stagnation and static pressure measured by the moving Pitot probe, $P_{¥0}$ and $P_{¥}$ are the stagnation and static pressure measured by a reference Pitot probe located at the upstream section of the wind tunnel. In figure 2-21, the horizontal axis is the probe position on z-axis of the coordinate system shown in figure 3-1 and normalized by the axial blade chord c_a = 5.46". The results show zero pressure gradient and good periodicity across the of blade row.

Chapter 3 Results and Discussion

Four sensor hot wire measurements were taken to give a detailed description of the mean and turbulent flow field downstream of the compressor cascade. The coordinate system used to present the results is given in figure 3-1. In this coordinate system, the origin is located on the lower end-wall midway between the leading edges of blades 4 and 5. The x-axis is perpendicular to the blade row leading edge line and the positive direction corresponding to downstream. The y-axis is perpendicular to the end-wall and positive into the flow. The *z*-axis is aligned with the blade row leading edge line. All distances are normalized on the axial chord of the blade $c_a = 5.46"$.

Measurements were taken at 3 different axial locations $x/c_a = 1.51$, $x/c_a = 2.74$ and $x/c_a = 3.75$ downstream of the central passage (between blades 4 and 5) over a tangential (*z)* distance equivalent to 150% of the distance between blade for the design tip gap of 0.165". The measurement planes are shown in figure 3-2. Measurements at 1 axial station $x/c_a = 2.74$ were also made for two other tip gaps of 0.083" and 0.330". All measurements were made both with and without wall motion. Velocities are presented in terms of the mean components *U, V, W* and the fluctuating components *u, v, w*. The mean streamwise velocity *U* is aligned with the mainstream flow direction downstream the cascade. According to the cascade turning angle (11.5°), *U* makes a 53.6° angle with the x-axis. All the velocity results are normalized on cascade inflow free stream velocity $U_¥$. This was monitored using a Pitot static probe mounted at upstream end of the test section. The Pitot static probe was located 6" above the lower end wall of upstream section and 72" upstream of the passage between blade 7 and 8. The velocity at the Pitot static is not exactly $U_¥$ because of some diffusion occurring in the vicinity of the suction slots. The flow decelerates by 3% at the suction slot, but the mean flow direction remains closely aligned with tunnel axis (verified by four-sensor hot-wire measurements in suction slot-region). The Pitot-static velocities were therefore multiplied by 0.97 to obtain $U_¥$.

Relative uncertainties for the velocity measurements were computed for 20:1 odds (95% confidence), and listed in table 3-1.

Table 3-1 Uncertainties in the measurements calculated at 20:1 odds

Quantity	Uncertainty (20:1)
U, V, W	$\pm$ 1% $U_{¥}$
$\overline{u^2}$	$\pm 3\% \overline{u^2}$
$\overline{v^2}$ $\overline{w^2}$	$\pm 6\% \overline{v^2}$, $\pm 6\% \overline{w^2}$
$\overline{uv}$ $\overline{vw}$ $\overline{uw}$	$\pm 3\% \sqrt{u^2 v^2}$
tke (k)	$\pm$ 3.5% k

The moving wall system described in chapter 2 was used to simulate the relative motion between the blade tip and engine casing. During all the measurements with moving wall, its speed was fixed at 23.5m/s. This corresponds to the tangential component of the inlet flow speed of $U_{¥}$ = 26m/s. At all 3 measurement stations, measurements were taken in both moving and stationary wall cases.

3.1 Inflow Boundary Layer

Single hot wire measurements were made to examine the inflow field and inlet boundary layer profiles. The measurement points are shown in Figure 3-3. The 3 profiles are located at $x/c_a = 0$ and in the same relative position of passage 3, 4 and 5 (z/c_a =1.95, z/c_a =0.248 and z/c_a =-1.453). Figure 3-4 shows the boundary layer mean velocity profiles. Figure 3-5 shows the turbulence intensity profiles. Velocity is normalized on $U_{¥}$.. The turbulence intensity $\overline{u^2}$ is normalized on U_{∞}^2. The height above the end wall surface is normalized on c_a. These boundary layer profiles appear very similar to each other, which is evidence for the uniformity of the inflow field. The boundary layer parameters, boundary thickness d , displacement thickness d^* and momentum thickness q are given in table 3-2.

Table 3-2 Boundary Layer Parameters

	d/c_a	d^*/c_a	q/c_a
Passage #3, z/ c_a =1.95o	0.046	2.10×10^{-2}	1.69×10^{-2}
Passage #4, z/ c_a =0.248	0.048	2.15×10^{-2}	1.75×10^{-2}
Passage #5, z/ c_a = -1.453	0.047	2.12×10^{-2}	1.72×10^{-2}

3.2 Mean Flow Field

3.2.1 Overall Flow Structure

Figures 3-6a to 3-8a present contours of mean streamwise velocity *U* at 3 downstream locations with end wall motion. The contour variables are normalized on the inlet free stream velocity $U_{¥}$. Figure 3-6b to 3-8b are the mean cross-flow vectors (*V, W*). *V* and *W* are also normalized on $U_{¥}$ and the relative magnitude of these vectors could be compared with the reference vector ($0.5U/U_{¥}$) indicated on each plot. In both sets of plots, the vertical axis is height above the lower end wall normalized by axial chord (c_a =5.46"). The horizontal axes corresponding to the *z* direction in figure 3-1, also normalized on c_a. In order to reveal the flow that observer looking from the downstream to upstream direction, the aspect ratio of axes are adjusted in all cross section plots.

The figures clearly show the overall flow structure downstream the compressor cascade. The two vertical striped regions are the wakes of blades. The right hand one is the wake of blade 5; the left hand one is the wake of blade 4. At the first station ($x/c_a = 1.51$), the center of the blade 4's wake located at $z/c_a = -1.33$. At the last location ($x/c_a = 3.75$), the center of blade 4's wake located at $z/c_a = -4.15$. Connecting these two points suggests an angle of 11.61° with the inflow direction, which agrees with the turning angle of the flow measured from the geometry of sidewall. At the second location ($x/c_a = 2.74$), the wake center is located at $z/c_a = -2.60$ which is on the same straight line connecting the wake center at the other two stations. At all three positions, the distance between the two wakes is $1.7\,c_a$ (9.29") that is consistent with the blade spacing.

The tip-leakage vortex flow from blade 4 dominates the lower half region and produces large axial velocity deficit. The averaged mainstream velocity could be estimated approximately by considering the cascade flow as 2-dimensional incompressible flow and applying the continuum relation on it. With the inlet flow angle 65.1° and turning angle11.5°, the exit angle is 36.4°. From the equation:

$$U_{¥} \cos(\text{inlet angle}) = U_{downstream} \sin(\text{exit angle})$$

The downstream mean stream velocity is $0.71U_{¥}$. This value agrees with the measured result of $0.705U_{¥}$, which was obtained by integral the mean stream wise velocity over the whole cross-section. At the other two downstream locations: $x/c_a = 2.74$ and $x/c_a = 3.75$, the mean value is $0.695U_{¥}$ and $0.693U_{¥}$. This slight deceleration maybe caused by the mass flow leaked from the two gaps between sidewall and the moving wall surface described in chapter 2.

Table 3-3 Averaged Mean Streamwise Velocity

$x/c_a = 1.51$ (Moving Wall)	0.7057	$x/c_a = 1.51$ *(Stationary Wall)*	0.7022
$x/c_a = 2.74$ (Moving Wall)	0.6976	*$x/c_a = 2.74$ (Stationary Wall)*	0.6892
$x/c_a = 3.75$ (Moving Wall)	0.6959	*$x/c_a = 3.75$ (Stationary Wall)*	0.6964

3.2.2 Tip Leakage Vortex

The tip leakage vortex is clearly visible on the meanstream wise velocity contours as the region of large velocity deficit at the lower region near the end wall. At $x/c_a = 1.51$, the crosswise velocity vectors also show strong circular motion around the vortex core. At $x/c_a = 1.51$, the vortex from blade 4 is located between the wakes of blades 4 and 5 but has begun to mix with the wake of blade 5. At $x/c_a = 2.74$, the vortex center is further to the right and the maximum velocity deficit point is located at the same z position of the wake center of blade 5. At $x/c_a = 3.75$), the vortex center moved to the

right of the wake center of blade 5. At the second and third location, the tip-leakage flow from blade 3 also occupies an important part of the passage between blade 4 and 5. When traveling downstream, the vortex also becomes larger and influences a larger area of the flow field near the lower end wall.

Considering the tip leakage vortex from blade 4, the peak mean stream wise velocity deficit (compared to the mainstream velocity, normalized on approach free stream velocity $U_{¥}$) and the location at which it occurs are listed in table 3-4.

Table 3-4 Peak Velocity Deficit normalized on $U_{¥}$

	Peak velocity deficit	y/c_a	z/c_a
$x/c_a = 1.51$	0.33	0.11	-2.66
$x/c_a = 2.74$	0.19	0.14	-4.25
$x/c_a = 3.75$	0.12	0.23	-5.85

The peak deficit drops rapidly as the vortex develops downstream and there is a 2.9 fold decrease during the total $2.24\ c_a$ axial distance. The shape of the region that has large velocity deficit is also changed during the development of vortex downstream. At $x/c_a = 1.51$, the vortex core region is a well defined small round region. At $x/c_a = 2.74$ and $x/c_a = 3.75$, the vortex core is merged with another high deficit region that extends from the end wall perhaps caused by the non-slip condition.

On the crosswise velocity vectors of $x/c_a = 1.51$, the strong cross flow field clearly shows the vortex structure and the vortex core. At $x/c_a = 2.74$, the cross flow vectors are much weaker but the vortex structure is still clear. At $x/c_a = 3.75$, the vortex structure could not be seen very clearly and there no well-defined vortex core. Another phenomena is the development of the crosswise flow near the end-wall surface. From $x/c_a = 1.51$ to $x/c_a = 3.75$, the crosswise velocity vectors near the wall become parallel to the wall surface and their magnitude increases. That shows the influence of the moving-wall motion.

Another viewpoint to see the tip leakage vortex is the vorticity distribution. Figure 3-9 to 3-11 show the contours of mean streamwise vorticity defined by:

$$\Omega_x = \frac{\partial W}{\partial y_1} - \frac{\partial V}{\partial z_1}$$

The vorticity is normalized on U_{∞}/c_a.

The partial differentials are taken with respect to the coordinate directions x_1, y_1 and z_1 alligned with the mean velocity components, U, V and W (shown in figure 3-1) . All the differentials along x_1 direction are taken to be zero. The contours indicated that the tip leakage vortex decays rapidly as it develops downstream. Only at $x/c_a = 1.51$, the vortex core region is well defined. From $x/c_a = 1.51$ to $x/c_a = 3.75$, there is a 3.9 fold decrease of the vorticity at the core region. The other interesting region is the one on the upper right of the tip leakage vortex that has negative vorticity, perhaps indicating a vortex rotating in the opposite sense as the tip leakage vortex. This vortex is well defined at $x/c_a = 1.51$ to $x/c_a = 2.74$ stations, but decays more quickly than the tip leakage vortex. A 5 fold decrease of vorticity was found from $x/c_a = 1.51$ to $x/c_a = 3.75$. Also, this secondary vortex is not well defined in the cross vectors.

3.3 Turbulent flow field

3.3.1 Overall Turbulence Flow Structure

Two parameters to describe the turbulent flow field and its development downstream the compressor cascade are the turbulence kinetic energy (*tke*) and *tke* production. The *tke* is given by:

$$\frac{\overline{u^2} + \overline{v^2} + \overline{w^2}}{2}$$

Where $\overline{u^2}$, $\overline{v^2}$ and $\overline{w^2}$ are Reynolds normal stresses. Figure 3-12 to figure 3-14 presents contours of *tke* at the 3 downstream locations. The *tke* values are normalized on U_{∞}^2. The vertical and horizontal axes are normalized on the axial chord c_a. The contours of individual Reynolds' stress components (normal stress and shear stress) are given in figure 3-21 to figure 3-23. All these components are also normalized on U_{∞}^2.

The *tke* production is computed by calculating the contribution of all 6 individual stress components, it is given by the equation:

$$-\overline{u^2}\frac{\partial U}{\partial x_1}-\overline{v^2}\frac{\partial V}{\partial y_1}-\overline{w^2}\frac{\partial W}{\partial z_1}-\overline{uv}\left(\frac{\partial U}{\partial y_1}+\frac{\partial V}{\partial x_1}\right)-\overline{uw}\left(\frac{\partial U}{\partial z_1}+\frac{\partial W}{\partial x_1}\right)-\overline{vw}\left(\frac{\partial V}{\partial z_1}+\frac{\partial W}{\partial y_1}\right)$$

Where $\overline{uv}$, $\overline{vw}$ and $\overline{uw}$ are Reynolds shear stresses.

The derivatives along x_1 were taken as 0. Figure 3-15 to 3-17 show the distribution of *tke* production at the 3 downstream locations.

The shape of the contours of *tke* is similar to that of the stream wise mean velocity contours shown in figure 3-6a to 3-8a. The high turbulence regions indicate the wakes of blades 4 and 5 and the tip-leakage vortex. The overall flow structure is identical to the structure indicated by mean stream wise velocity contours. The tip leakage vortex dominates the end-wall region.

3.3.2 Tip Leakage Vortex

At $x/c_a = 1.51$, the region with highest *tke* is around the vortex core (the region of high velocity deficit). From figure 3-21, the largest contributor to tke is the component $\overline{w^2}$. For the Reynolds shear stresses, $\overline{uv}$ and $\overline{uw}$ are more dominant. At the downstream stations, another high-tke region develops at the position where the flow is lifting from the end-wall. At $x/c_a = 2.74$, the tke in the two regions has roughly the same level. At $x/c_a = 3.75$, these two regions have merged together. The tke at the vortex center decreases from 0.0129 at $x/c_a = 1.51$ to 0.0048 at $x/c_a = 3.75$. At $x/c_a = 2.74$, $\overline{u^2}$ and $\overline{w^2}$ are the dominant terms of the tke in the flow-lifting region. The dominant role of $\overline{uv}$ and $\overline{uw}$ remained unchanged.

Looking at the tke production, at $x/c_a = 1.51$, there are 3 high-production regions with roughly the same production level. Two of them are around the vortex core, the other one is the region where the tip leakage flow lifts away from the end wall. At $x/c_a = 2.74$, the production in the region around the vortex core is much less than the lifting flow region. At $x/c_a = 2.75$, the core region has merged with the lifting flow region. Comparing the shape of the *tke/tke* production contour with the shape and magnitude of

individual Reynolds stress components, the terms with largest contribution to the *tke* production appear to be $\overline{uv}$ and $\overline{uw}$.

The *tke* production also could be decomposed to two parts. The $\overline{u^2}$, $\overline{uv}$ and $\overline{uw}$ terms of the tke production equation are the contributions to the production due to the gradients in the axial velocity, (hereafter referred to as streamwise contribution), and the terms of $\overline{v^2}$, $\overline{w^2}$ and $\overline{vw}$ are referred to as crossflow contribution. Figure 3-18 to 3-20 show the contours of streamwise contribution and crossflow contribution to the tke production at the 3 downstream locations. The distribution and production magnitude clearly show that the streamwise contribution is much larger than the crossflow contributions. That means most of the turbulence is being generated by the axial deficit of the tip-leakage vortex rather than its rotating motion.

The peak magnitudes of the individual Reynolds stress components (normalized on U_∞^2) at different locations are listed in table 3-5. This table shows the decay of these components along the flow direction. It also shows the relative importance of these components. All the Reynolds stresses decay roughly at the same rate. The three Reynolds normal stress components have roughly the same magnitude. The three Reynolds shear stress components also have the same magnitude. The normal stresses are, of course, larger than shear stresses but they are in the same order, so none of these components are negligible. In the three shear stresses, only $\overline{uw}$ has both high positive and negative values, but the large peak negative value (-2.6/-2.6×10^{-3}) occurring at *x/ca=1.51* is not in the tip leakage vortex.

Table 3-5 Peak Values of Reynolds Stress Components

	x/c_a =1.51	x/c_a =2.74	x/c_a =3.75
$\overline{u^2}$	9.3×10^{-3}	5.4×10^{-3}	3.9×10^{-3}
$\overline{v^2}$	7.56×10^{-3}	4.1×10^{-3}	3.2×10^{-3}
$\overline{w^2}$	1.1×10^{-2}	5.0×10^{-3}	3.7×10^{-3}
$\overline{uv}$	7.3×10^{-4}/-3.5×10^{-3}	0.75×10^{-4}/-2.4×10^{-3}	-1.8×10^{-3}
$\overline{vw}$	1.62×10^{-4}/-2.8×10^{-3}	2.48×10^{-4}/-1.7×10^{-3}	2.4×10^{-4}/-1.16×10^{-3}
$\overline{uw}$	3.3×10^{-3}/-2.6×10^{-3}	2.2×10^{-3}/ -0.7×10^{-3}	1.5×10^{-3}/ -0.5×10^{-3}

3.4 Spectral Results

Velocity spectra in the tip leakage vortex from blade 4 were also taken by using 4-sensor hotwire probe. The sampling frequency was set to 50kHz. Spectra were formed by averaging FFTs of some 50 records of length of 3000 samples. Figure 3-24 to 3-26 present the results of autospectra measured at 3 downstream locations. The autospectra G_{uu}, G_{vv}, G_{ww} are normalized on cU_∞, where c is the total blade chord length (10"). The autospectra are plotted against the nondimensionalized frequency fc/U_∞. The small picture attached on the plots shows the measurements position in the tip leakage vortex. All the spectra show the typical character of fully turbulent flows. They have roughly –5/3 slopes in the inertial subrange and the drop off at higher frequencies. In *Gvv* and *Gww* plot, there is a distinct spectral peak at a normalized frequency of about 1 that indicates some possibly organized motion in the vortex region. This peak corresponds to a frequency of 98Hz. This frequency is much different from the vortex shedding frequency in the blade wakes (about 420Hz) obtained by Muthanna (1998). No distinct spectral peaks present in the *Guu* plots. The autospectra measured at location 5 at $x/c_a = 1.51$ are lower because this point was near the edge of tip leakage vortex and almost located in the free stream.

3.5 Effects of Tip-Gap Variations

Previous studies have indicated the blade tip gap height is an important factor that influences the flow field downstream of a compressor cascade. To study the tip gap height effects in the moving end wall case, measurements are taken when both double and half the design tip gap height. As motioned at chapter 2, the blade design tip gap was 0.165". So the doubled tip gap is 0.33" and halved tip gap is 0.083". Measurements were made at $x/c_a = 2.74$ to examine the effects of tip gap.

Figures 3-27a and 3-28a show the mean streamwise velocity contours for the double and half size tip gap. The crosswise velocity vectors at double and half size tip gap are shown in figures3-27b and 3-28b. Comparing with the mean velocity contours and crosswise velocity vectors measured with the design tip gap (figures 3-7), a strong

influence of tip gap on the leakage vortex flow is visible. The size of vortex region increases with tip gap. At double tip gap, the crosswise velocity vectors showed strong circular motion around the vortex center and the vortex center is well defined. At design tip gap, the vortex center still visible at the crosswise velocity vector, but the vector magnitude of circular motion is just half of the magnitude at double tip gap. At half tip gap, the vortex center is not well defined and the vector magnitude of circular motion is much smaller showing that the tip leakage vortex is weak. The directions of crosswise velocity vectors at the bottom of the figures are roughly parallel to the end wall indicating the effect of end wall motion.

Figures 3-29 and 3-30 show the streamwise vorticity distribution at double and half tip gap. The figure shows that although the size of the vortex region increases with tip gap, the peak vorticity remains roughly the same. The counter-rotating secondary vorticity can be seen at all tip gaps.

Figures 3-31 and 3-32 show contours of tke for the double and half size tip gaps. Figures 3-33 and 3-34 are the contours of *tke* production. These figures reveal the overall structure of turbulence flow field. At half tip gap, the high *tke* levels are concentrated in a single region around the vortex core. At normal and double tip gap, there are two regions with high tke levels, one is around the vortex core, another one is the region where the tip leakage flow is lifting up away from the end wall. The tke production contours show that for all 3 different tip gaps, the maximum tke production comes from the region where the tip leakage flow is lifting away from the end wall. *tke* levels in the vortex core reduce with decreasing tip gap. Considering the streamwise and crossflow contribution (figure 3-35 and 3-36), most of the turbulence is generated by the streamwise contribution at both cases.

Figures 3-37 and 3-38 are contours of the 6 individual Reynolds stress components for the double and half-size tip gap. Table 3-6 shows the peak values of these components. In the normal stress components, $\overline{u^2}$ and $\overline{w^2}$ have the largest contribution to the tke. In the shear stress components, $\overline{uv}$ and $\overline{uw}$ have large values compared to $\overline{vw}$. All the six components will decrease when the tip gap reduced. All the six components have the same order of magnitude and are not negligible.

Table 3-6 Peak Values of Reynolds Stress Components

	Double tip gap	Normal tip gap	Half tip gap
$\overline{u^2}$	6.64×10^{-3}	5.4×10^{-3}	5.52×10^{-3}
$\overline{v^2}$	6.00×10^{-3}	4.1×10^{-3}	3.48×10^{-3}
$\overline{w^2}$	6.67×10^{-3}	5.0×10^{-3}	4.81×10^{-3}
$\overline{uv}$	$3.1\times10^{-4}/-2.82\times10^{-3}$	$0.75\times10^{-4}/-2.4\times10^{-3}$	$0.97\times10^{-4}/-2.14\times10^{-3}$
$\overline{vw}$	$3.6\times10^{-4}/-1.95\times10^{-3}$	$2.48\times10^{-4}/-1.7\times10^{-3}$	$0.64\times10^{-4}/-1.12\times10^{-3}$
$\overline{uw}$	$2.3\times10^{-3}/-1.1\times10^{-3}$	$2.2\times10^{-3}/-0.7\times10^{-3}$	$1.68\times10^{-3}/-0.64\times10^{-3}$

3.6 Effects of Moving Wall

The tip leakage flow is formed and developed at the region near the end wall, so the relative motion between blade tip and end wall is likely to play an important role to the formation and development of tip leakage vortex. To study the effects of the moving end wall, measurements are taken with stationary end wall at the same location as moving wall cases. All these measurements were made successively with the corresponding moving wall measurements, minimizing any other differences in conditions between the two.

3.6.1 Mean Flow Field

Figure 3-39 is the comparison of mean stream contours at $x/c_a = 1.51$ with and without wall motion. To make the comparison clearly, both moving wall and stationary wall cases are plotted together using the same contour levels. The contours clearly show the difference between the two cases. First, the shape of the tip leakage vortex is changed. In stationary wall case, the vortex and vortex core is round. The vortex center is located at $y/c_a = 0.15$, $z/c_a = -2.35$. In the moving wall case, the vortex and vortex core are stretched into an elliptical shape. In the moving-wall case, the vortex center is swept

further across the end-wall than in the stationary wall case and the vortex core remains nearer the end wall, indeed part of the vortex flow has began to merge with the wake of blade 5 in this case. In the stationary wall case, the vortex remains roughly half way between the wakes of blades 4 and 5, and there is almost no interaction between the vortex flow and the wake of blade 5. The peak mean streamwise velocity deficit at moving wall case is smaller than stationary wall case, which indicates that the strength of vortex is smaller in moving wall case. The contours also show that the moving end wall doesn't have much influence the part of blade wake away from the end wall.

The motion of the tip leakage vortex across the passage suggests that the vortex axis and the mainstream axis are not aligned one. Defining the vortex axis as the locus of points of peak mean streamwise vorticity, the vortex axis makes a 56.1° with the x-axis in the moving wall case, and makes a 56.6° angle with x-axis at stationary wall case. According to the 11.5° turning angle, the mean stream flow has a 53.6° angle with the x-axis, so the vortex axis has an angle of 2.5° and 2.1° in moving wall and stationary wall cases respectively.

Figure 3-40 is a comparison of crosswise mean velocity vectors for the stationary wall and moving wall cases at $x/c_a = 1.51$. The vector pattern clearly shows the formation of tip leakage vortex in both cases. The wall jet flow driven by the pressure gradient between the pressure side and suction side of blade 4 swept into the passage between blade 4 and 5, lifts up from the end wall and rolls back to form a circular motion. The two flow patterns also clearly show the effects of end wall motion. In stationary wall case, the wall jet flow lifts away from the wall at a much greater angle than in the moving wall case.

Figure 3-41 is compares the streamwise vorticity distribution at $x/c_a = 1.51$. The contour levels are the same at two cases. At stationary wall case, the vorticity value in the vortex region is larger than the moving wall case. Calculation of the circulation around the tip-leakage vortex by integrating the streamwise vortex in the vortex region (defined by a rectangle of height $0.3c_a$ and width $0.6c_a$ centered on the peak vorticity location. The rectangle region is the same in moving and stationary wall cases) gives the results is listed in table 3-7 (normalized on $U_\infty c_a$).

Table 3-7 The Circulation around the Vortex (normalized on $U_\infty c_a$)

	x/ c_a =1.51	x/ c_a =2.74	x/ c_a =3.75
Stationary Wall	3.784	2.934	2.338
Moving Wall	3.346	2.178	1.915

Again, the circulation shows that the tip-leakage vortex is stronger in the stationary wall case at all downstream locations.

3.6.2 Turbulence Flow Field

Figure 3-42 is comparison of *tke* distribution at $x/c_a = 1.51$ in the stationary wall and moving wall cases. Figure 3-43 compares *tke* production. In stationary wall case, there are two distinct regions in the tip leakage vortex that have high level of *tke*. One is around the vortex core, the other extends from the location where the cross-flow lifts away from the end wall. In moving case, these two regions seem merged together. The stationary wall has larger overall the tke production, however, the tke production contours suggest that the mechanism of turbulence generation may be similar in the two cases. The maximum contribution to the turbulence generation is in the region that flow being lifted from the end wall. The *tke* production is smaller in moving wall case, which indicated weaker lifting flow. Separate *tke* production from streamwise and crossflow contributions are compared in figure 3- 44.

Figure 3-45 is a comparison of Reynolds normal stresses. Figure 3-46 shows the Reynolds shear stresses. The distributions of $\overline{u^2}$ and $\overline{v^2}$ have appear similar in both cases except that the peak stresses are lower with wall motion. The $\overline{w^2}$ distribution is different, however, and the two distinct high level regions seen in stationary wall case are merged together in moving wall case. The peak value of $\overline{w^2}$ in moving wall case is larger.

Amongst the three Reynolds shear stress components, $\overline{uv}$ is the least influenced by the end wall motion. It has roughly the same structure and magnitude in both cases. But $\overline{vw}$ and $\overline{uw}$ clearly show the effect of moving wall. In moving wall case, the area of

high magnitude negative $\overline{vw}$ (centered at $z/c_a = 2.7$) in the stationary wall case appears much smaller with wall motion and the stress magnitudes in this region are much smaller than in the stationary wall case. The magnitude of $\overline{uw}$ is also smaller in moving wall case. The $\overline{uw}$ contours also show some evidence of the interaction between the tip leakage vortex flow and the wake of blade 5. In these two-dimensioanal contour presentations, the angle between the vortex axis and the coordinate system in which the stresses are resolved could be a factor in influencing the distributions. However, given the fact that the angle between the vortex axis and mean flow axis were almost the same in both cases, the comparison between moving and stationary wall results is still valid.

3.6.3 Development of Tip Leakage Vortex

One of the key characteristics of the tip leakage vortex flow is the circulating motion around the vortex core. Figure 3-47 compares the crosswise mean velocity vectors at 3 different locations in the stationary and moving end wall cases. The vectors show the decay of tip leakage vortex downstream. In stationary wall case, the vortex becames larger when moving downstream. Meanwhile, the magnitude of the circulaing velocity vectors becomes smaller, but the cross-sectional shape of the flow pattern remains the same. The circulating motion is roughly symmetric around the vortex center and the vortex center is well-defined at all 3 locations. In the moving wall case, the vortex flow region is distorted by the wall motion at the downstream locations. The circulating motion is no longer symmetric and the vortex flow region is stretched in the negative z direction. The vortex core is not clearly defined at $x/c_a = 2.74$ and $x/c_a = 3.75$. The vortex region distortion may be caused that the moving wall adding negative z direction momentum to the tip leakage flow near the wall that tends to disrupt the formation of the vortex structure obtained in stationary wall case. From the analysis in Muthanna (1998), it was found that the less satisfactory appearance of the vortex in the cross velocity vector may be partly because the angle between the vortex axis and the mean flow direction. But this should not be an important factor here because the vortex axis angle is almost identical in the moving and stationary wall cases.

Figure 3-48 is a comparison of the mean streamwise vorticity distributions in the stationary wall and moving wall cases. To make the comparison easier to read, the contour levels are set the same at the 3 downstream locations. In both cases, the peak vorticity decreases with distance downstream. Table 3-8 is the peak vorticity values at both cases. In the stationary wall case, the peak vorticity decreases 2.8 fold from $x/c_a = 1.51$ to $x/c_a = 2.74$, and 1.61 fold from $x/c_a = 2.74$ to $x/c_a = 3.75$. In moving wall case, the peak vorticity decrease 2.48 fold and 1.27 fold relatively. So in moving wall case, the decay of peak vorticity is slightly smaller than stationary wall case.

Table 3-8 Peak Vorticity at Different Locations

	$x/c_a = 1.51$	$x/c_a = 2.74$	$x/c_a = 3.75$
Stationary Wall	3.46	1.24	0.77
Moving Wall	2.22	0.898	0.74

Figure 3-49 is a comparison of the tke contours. Again, the contour levels are set to the same at the 3 downstream locations. The *tke* contours clearly show the shape of the vortex flow region, they also indicate the decay of *tke* levels with downstream distance. Table 3-9 compares the peak value of tke at different locations. The data show the *tke* level has a 1.78 fold drop from $x/c_a = 1.51$ to $x/c_a = 2.74$ and 1.59 fold drop from $x/c_a = 2.74$ to $x/c_a = 3.75$ in stationary wall case. In the moving wall case, the decrease is 1.88 and 1.42 fold relatively. So, in terms of vorticity and *tke* decay, there is no substantial difference between stationary wall and moving wall cases.

Table 3-9 Peak *tke* at Different Locations

	$x/c_a = 1.51$	$x/c_a = 2.74$	$x/c_a = 3.75$
Stationary Wall	1.37×10^{-2}	7.6×10^{-3}	4.8×10^{-3}
Moving Wall	1.24×10^{-2}	6.69×10^{-3}	4.7×10^{-3}

In table 3-8 and 3-9, the most obvious difference between stationary wall and moving wall case is the peak vorticity value at $x/c_a = 1.51$. This may indicate that the greatest effect of wall motion occurs at the early stages of tip leakage vortex formation

and development. There may be three possible mechanisms for the moving wall influence the tip leakage vortex:

1. The moving wall adds negative z-direction momentum to the tip leakage flow which distort and reduce the strength of the circulating motion that forms the tip leakage vortex.
2. The moving wall drag the tip leakage vortex to further the right, cause the vortex core to begin to mix with the blade wake. The wake- vortex interaction may reduce the strength of the vortex.

Chapter 4 Conclusions

A large-scale moving end-wall system has been designed and built at the Aerospace and Ocean Engineering Department of Virginia Tech. This system forms part of a low-speed linear compressor cascade wind tunnel, where it is used to simulate the effects of the relative motion between the blade tips and casing upon the flow. Four-sensor hot wire probes were used to obtain the detailed flow field information downstream the compressor cascade at three different axial locations (x/c_a*=1.51, 2.74 and 3.75*). To reveal the effect of the height of blade tip gap, the measurements were made at three different tip gap heights (0.165", 0.33", 0.083") at one of these locations (x/c_a *=2.74*). At each situation, measurements were made both with and without moving end wall. The following conclusions are made from the results:

- The moving wall system was designed, built and successfully used. A newly developed method for manufacturing belt joins made it possible to use low-cost Mylar film as the moving belt. The characteristics of the moving wall such as small vertical vibration (0.0022±0.0004"), high speed stability (±0.1%) and belt temperature easily satisfied the project requirements. The belt lifetime was satisfied the measurement requirement. A special purpose speed meter was developed and used to monitor the speed of the moving belt.
- Both with and without the wall motion, the tip leakage vortex flow, which caused by the pressure difference between the pressure side and suction side of the blade dominates the downstream flow field near the end wall. The tip leakage is a region with high mean stream velocity deficit and there is, in most cases, a significant mean circular motion around the vortex core. The tip leakage vortex is also a region of high turbulence levels. It is also the source of turbulence. Most of the turbulence is generated in the region where the tip leakage flow being lifting up from the end wall surface. Autospectra inside the vortex flow are typical characteristics of a fully turbulent flow. The tip leakage vortex decays quickly with distance downstream. The region occupied by the vortex becomes larger.

The peak magnitude of mean velocity deficit, mean stream vorticity, *tke* and Reynolds stress components all decrease. The height of blade tip gap has important effects on the size and strength of the tip leakage vortex flow.

- Comparison of the results with moving wall and stationary wall shows the substantial effects of wall motion. Generally, the moving end wall somewhat reduces the strength of the tip leakage vortex. In the moving wall case, the vortex region swept further in the direction of wall motion than in stationary wall case and the shape of vortex region also stretched by the moving wall. End wall motion also tends to disturb the flow structure in the tip leakage flow. The circular motion inside the vortex region is not clear far downstream location. At stationary wall case, the circular motion is still well defined at far downstream. The possible reasons of the moving wall effects could be:
  1. The moving wall adds negative z-direction momentum to the tip leakage flow which distort and reduce the strength of the circulating motion that forms the tip leakage vortex.
  2. The moving wall drag the tip leakage vortex to further the right, cause the vortex core to begin to mix with the blade wake. The wake- vortex interaction may reduce the strength of the vortex.

Wall motion appears to have a greater influence on the tip leakage vortex in its early stage of formation. Although the moving wall only directly influences the flow near the end wall surface due to the non-slip condition, it changes the overall flow structure by changing the formation of tip leakage vortex flow. The moving wall has no effect to the wake flow of the blades.

Chapter 5 Reference

- Davino R. M., "Characteristics of the Flow in the Annulus-Wall Region of an Axial-Flow Compressor Rotor Blade Passage", AIAA-82-0413, AIAA 20th Aerospace Sciences Meeting, Orlando, Florida, January 11-14, 1982

- Devenport W. J., Rife M. C., Liapis S. I. and Follin G. J., "The Structure and Development of a Wing-tip Vortex", ASME: Journal of Fluid Mechanics, vol. 312, pp. 67-106, 1996.

- Graham J. A. H., "Investigation of a Tip Clearance Cascade in a Water Analogy Rig", Beijing International Gas Turbine Symposium and Exposition, Beijing, September 1-7, 1985

- Hason D. B., "Quantification of Inflow Turbulence for Prediction of Cascade Broadband Noise", Paper #990544 Fifth International Congress on Sound and Vibration, Adelaide, Australia, December 15-18, 1997

- Inoue M., Kuroumaru M., "Structure of Tip Clearance Flow in an Isolated Axial Compressor Rotor", ASME 88-GT-251

- Kang S., Hirsch C., "Tip Leakage Flow in Linear Compressor Cascade", Journal of Turbomachinery, October 1994, Vol. 116/657

- Kang S., Hirsch C., "Experimental Study on the Three-Dimensional Flow within a Compressor Cascade with Tip Clearance: Part I – Velocity and Pressure Fields, and Part II – The Tip Leakage Vortex", ASME Journal of Turbomachinery, October 1993, Vol. 115/435

- Lakshminarayana B., Padya A., "Tip Clearance Flow in a Compressor Rotor Passage at Design and Off-Design Conditions", ASME: Journal of Engineering for Gas Turbines and Power, July 1984, Vol. 106/570-577

- Lakshminarayana B., Zhang J., Murthy K. N. S., "An Experimental Study on The Effects of Tip Clearance on Flow Field and Loss in an Axial Flow Compressor Rotor", ISABE 87-7045

- Lakshminarayana B., Zaccaria M., Marathe B., "The Structure of Tip Clearance Flow in Axial Flow Compressors", ASME: Journal of Turbomachinery, July 1995, Vol. 117

- Muthanna C., Wittmer K. S., and Devenport W. J., "Turbulence structure of the Flow Downstream of a Compressor Cascade with Tip Leakage", AIAA 36th

Aerospace Sciences Meeting & Exhibit, Reno, Nevada, January 10-13, 1998, AIAA paper 980420-0404.

- Muthanna C., "Flowfield Downstream of a Compressor Cascade with Tip Leakage", MS Thesis, Virginia Tech, 1998.
  Avai:. http://scholar.lib.vt.edu/these/avaliable/etd-110798-235327/

- Storer J. A., "The Interaction Between Tip Clearance Flow and the Passage Flowfield in an Axial Compressor Cascade", ISABE 89-7024

- Storer J. A., Cumpsty N. A. "Tip Leakage Flow in Axial Compressors", ASME: Journal of Turbomachinery, April 1991, Vol. 113

- Stauter R. C., "Measurement of the Three-Dimensional Tip Region Flow Field in an Axial Compressor", ASME Journey of Turbomachinery, July 1993, Vol. 115/468-475

- Wenger C. W., Devenport W. J.,. Wittmer K. S., and Muthanna C., " Two-point Measurements in the Wake of a Compressor Cascade", 29th AIAA Fluid Dynamics Conference, June 15-18, 1998/ Albuquerque, NM

- Yaras M. I., Sjolander S. A., "Effects of Simulated rotation on Tip Leakage in a Planar Cascade of Turbine Blades: Part 1-Tip Gap Flow", Journal of Turbomachinery, July 1992, Vol. 114/653

- Yaras M. I., Sjolander S. A., Kind R. J., "Effects of Simulated rotation on Tip Leakage in a Planar Cascade of Turbine Blades: Part II-Downstream Flow Field and Blade Loading", Journal of Turbomachinery, July 1992, Vol. 114/661

- Yaras M. I., Sjolander S. A., "Development of the Tip-leakage Flow Downstream of a Planar Cascade of Turbine Blades: Vorticity Field", Journal of Turbomachinery, July 1990, Vol. 112/609

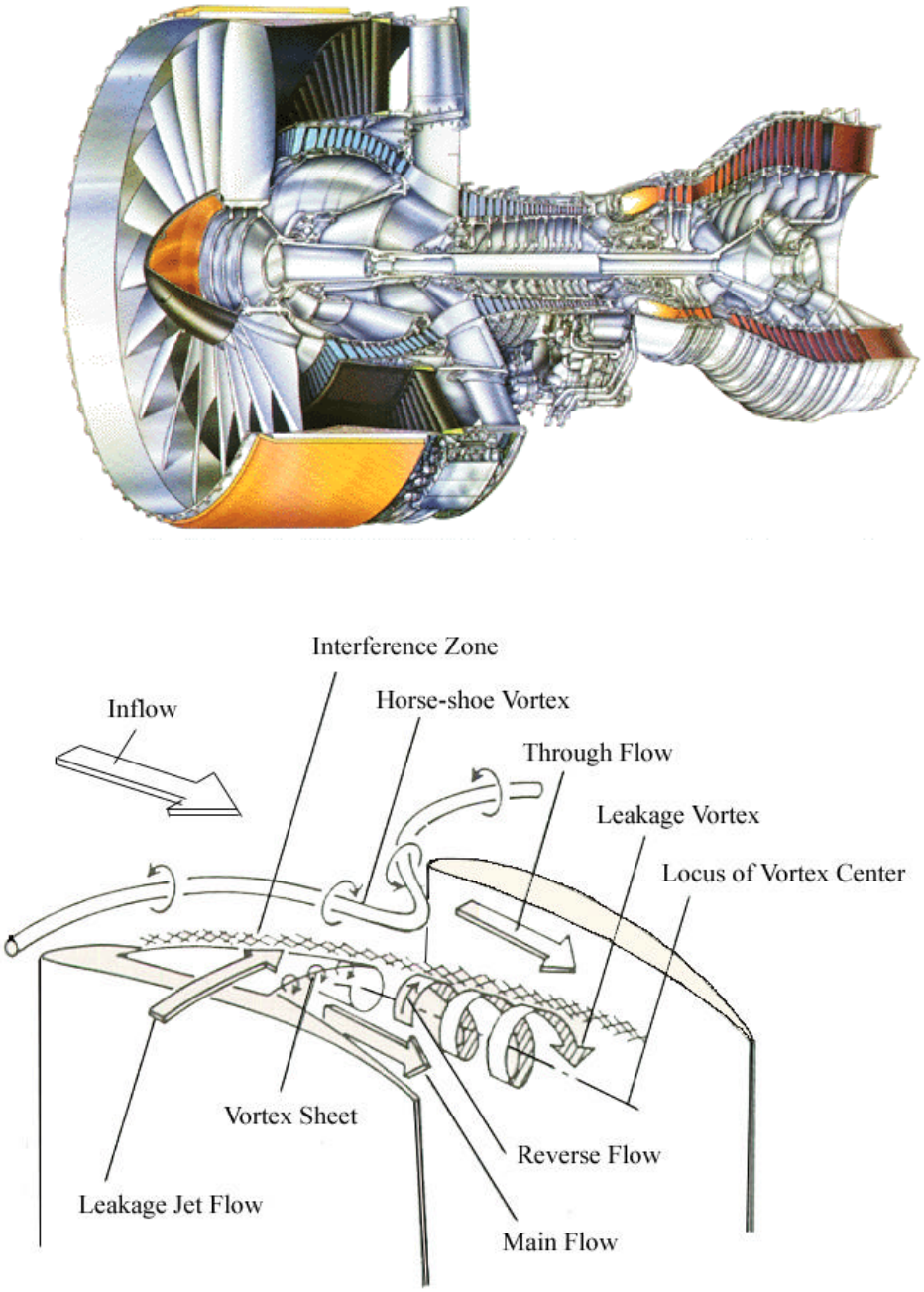

Figure 1-2 The Tip Leakage Flow Field

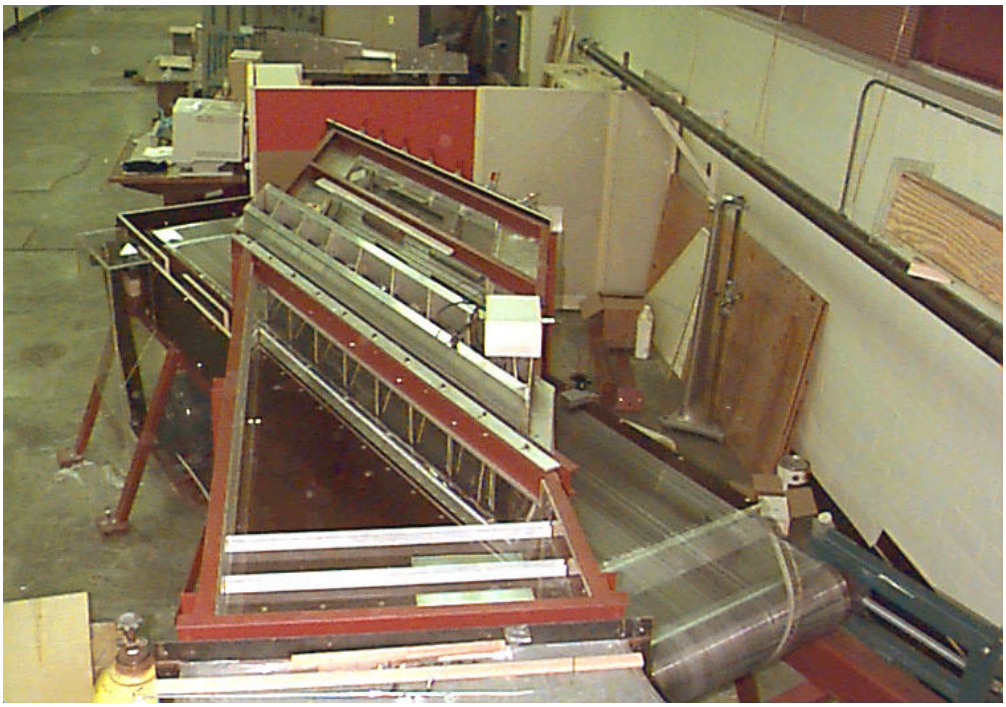

Figure 2-1 Virginia Tech Low Speed Cascade Wind Tunnel

Figure 2-3 The Compressor Cascade

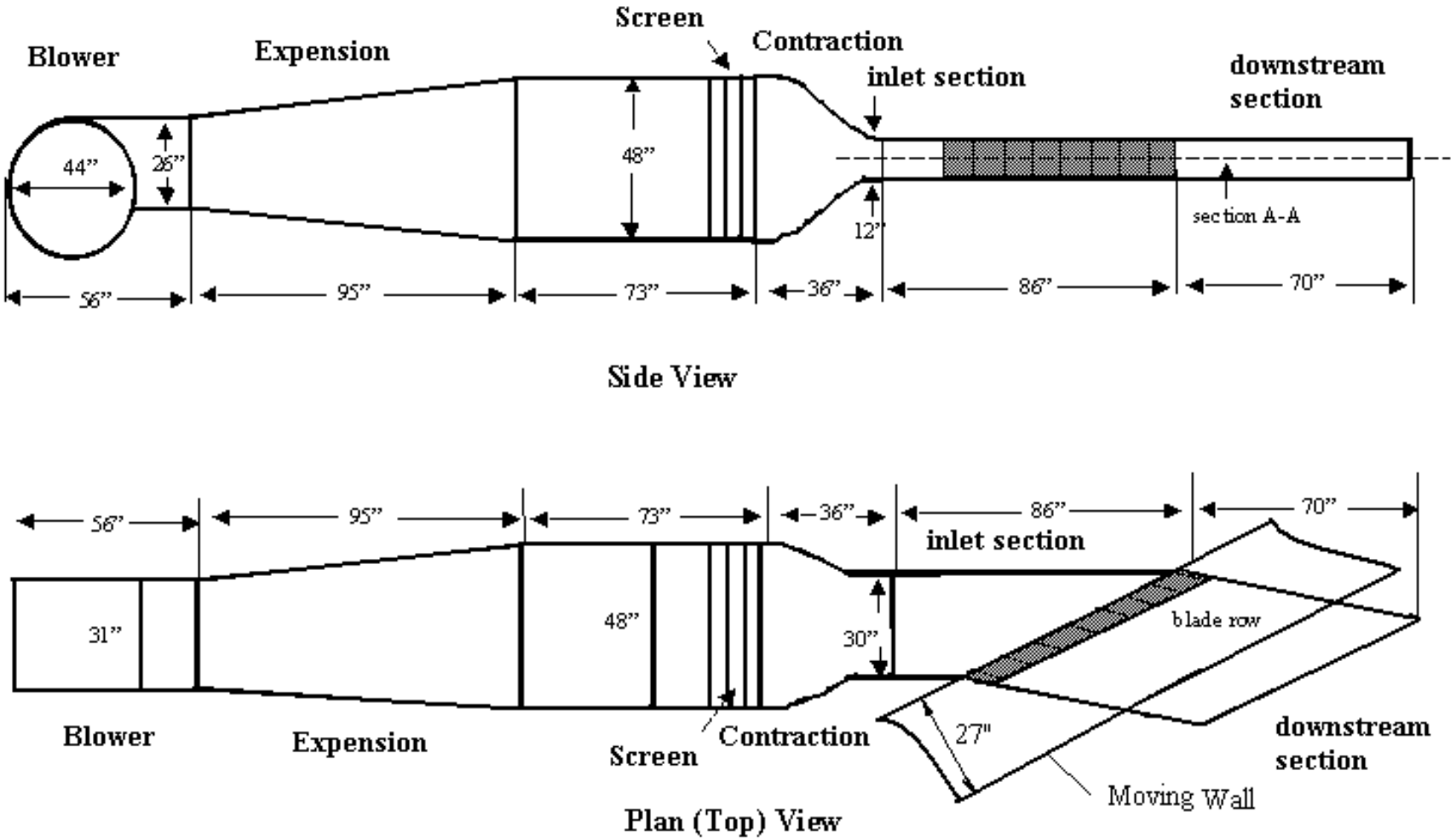

Figure 2-2 The Layout of Virginia Tech Linear Compressor Cascade

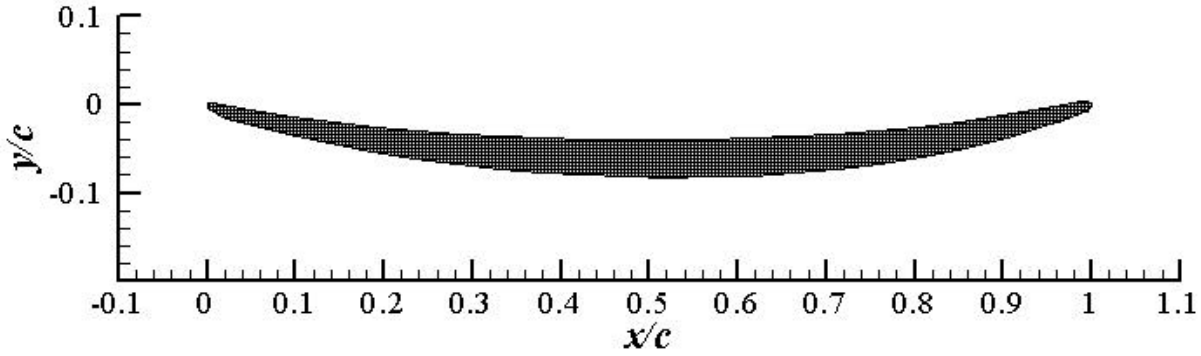

Figure 2-4 Cross Section of the GE rotor B-section Blade
Used in the cascade tunnel

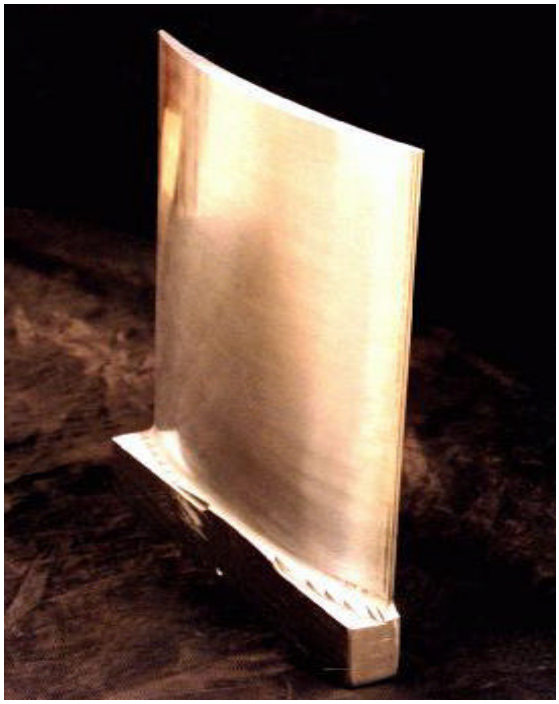

Figure 2-5 Compressor Rotor Blade

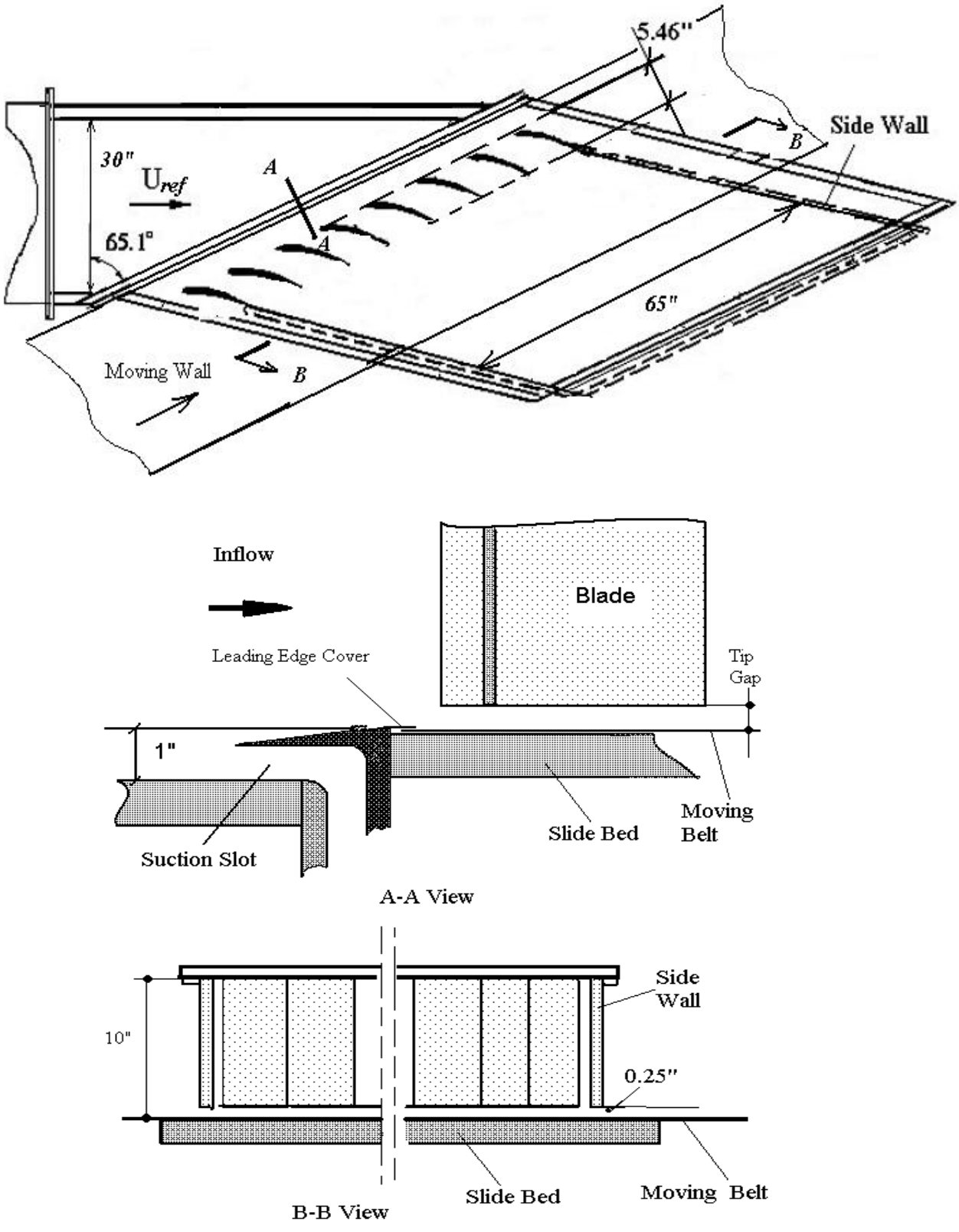

Figure 2-6 Cascade Wind Tunnel Test Section

Figure 2-7 Screen Attached at the end of Test Section

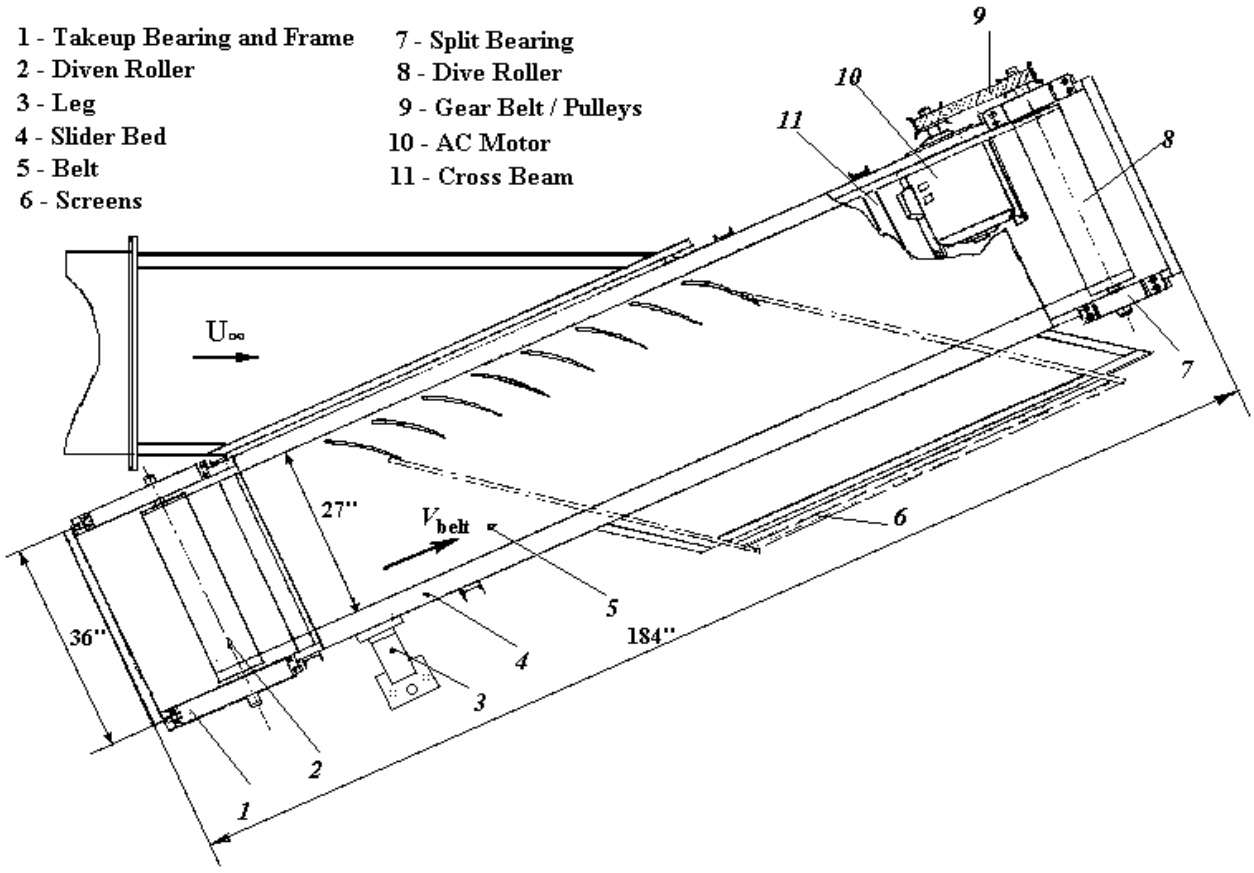

Figure 2-8 The Layout and Structure of Moving Wall System

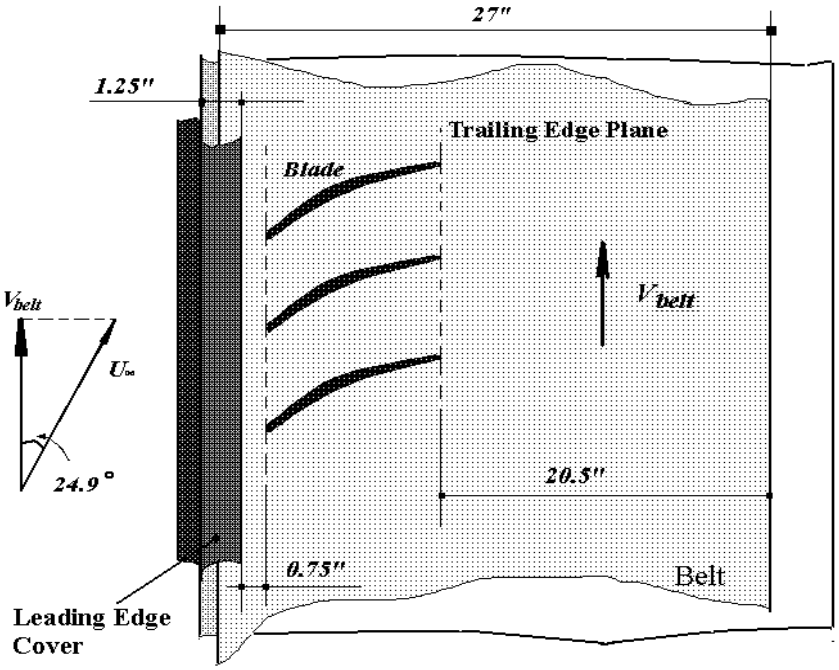

Figure 2-9 Dimension of Moving Wall

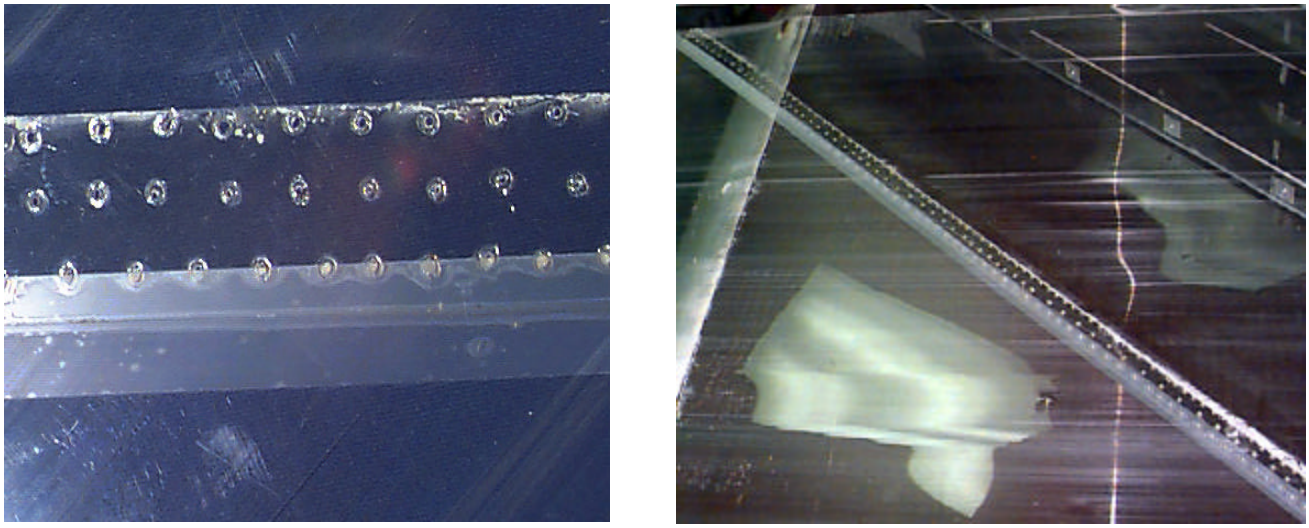

Figure 2-11 The Belt Join

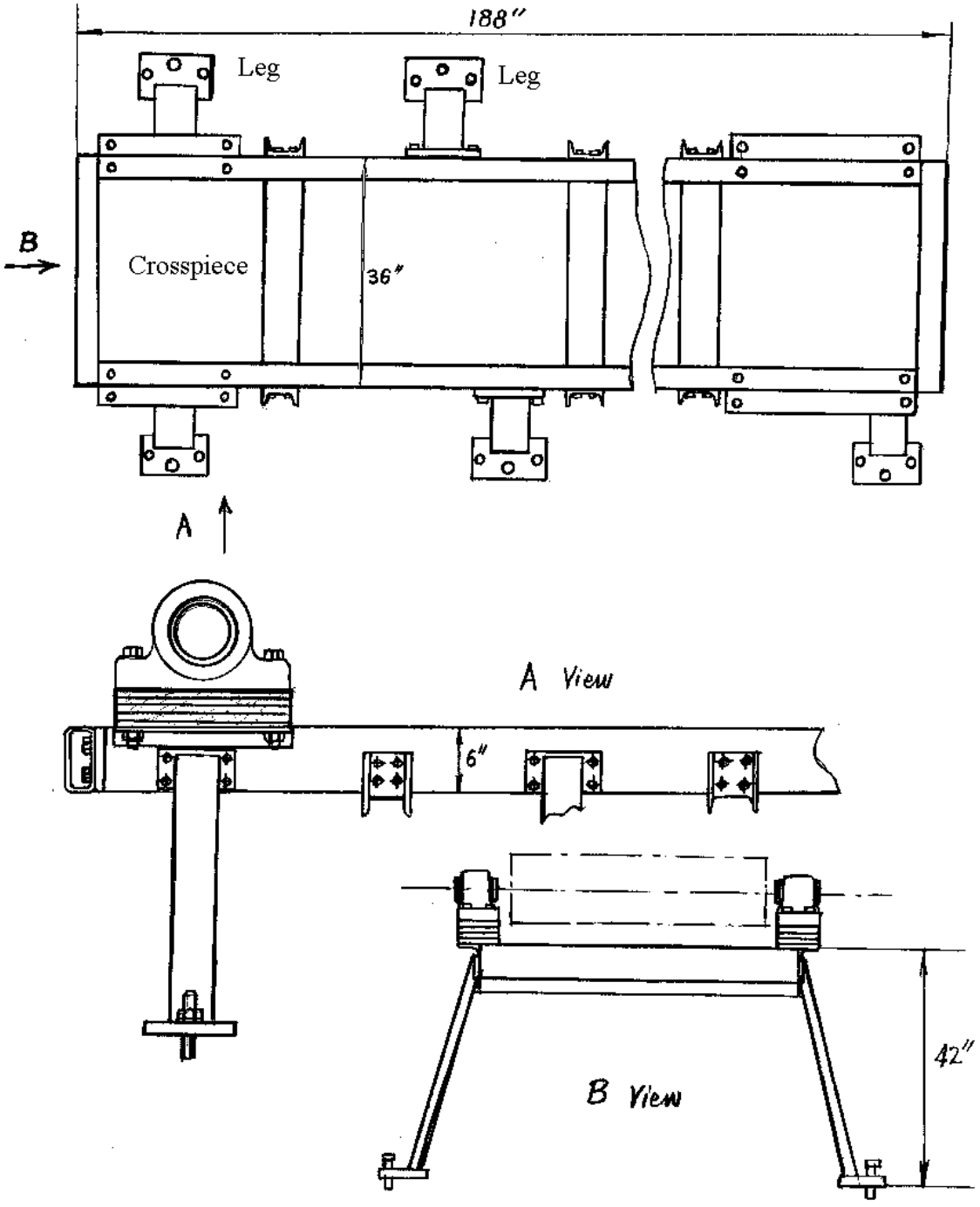

Figure 2-10 The Structure of Mainframe

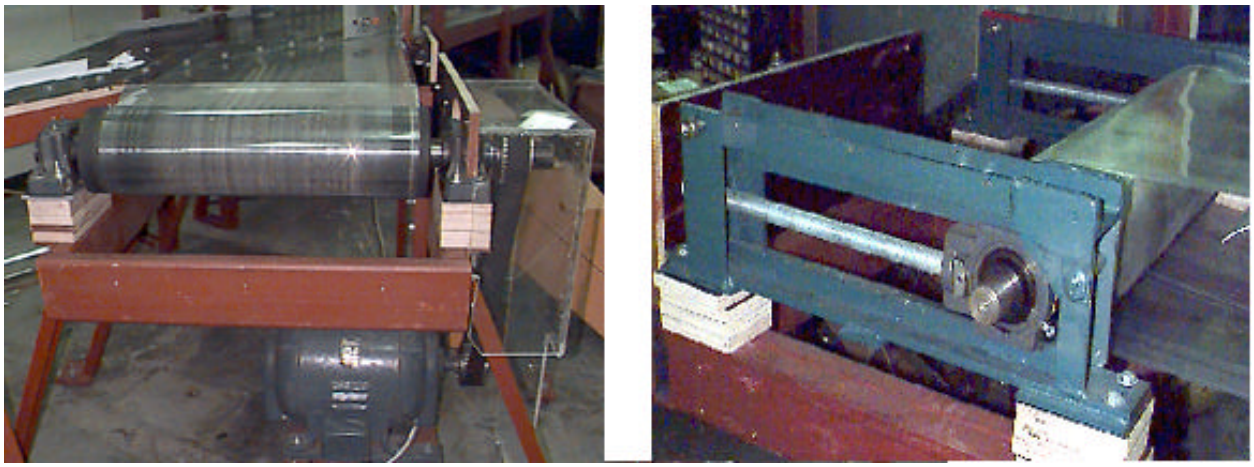

Figure 2-12 The Drive Roller (left) and Driven Roller (right)

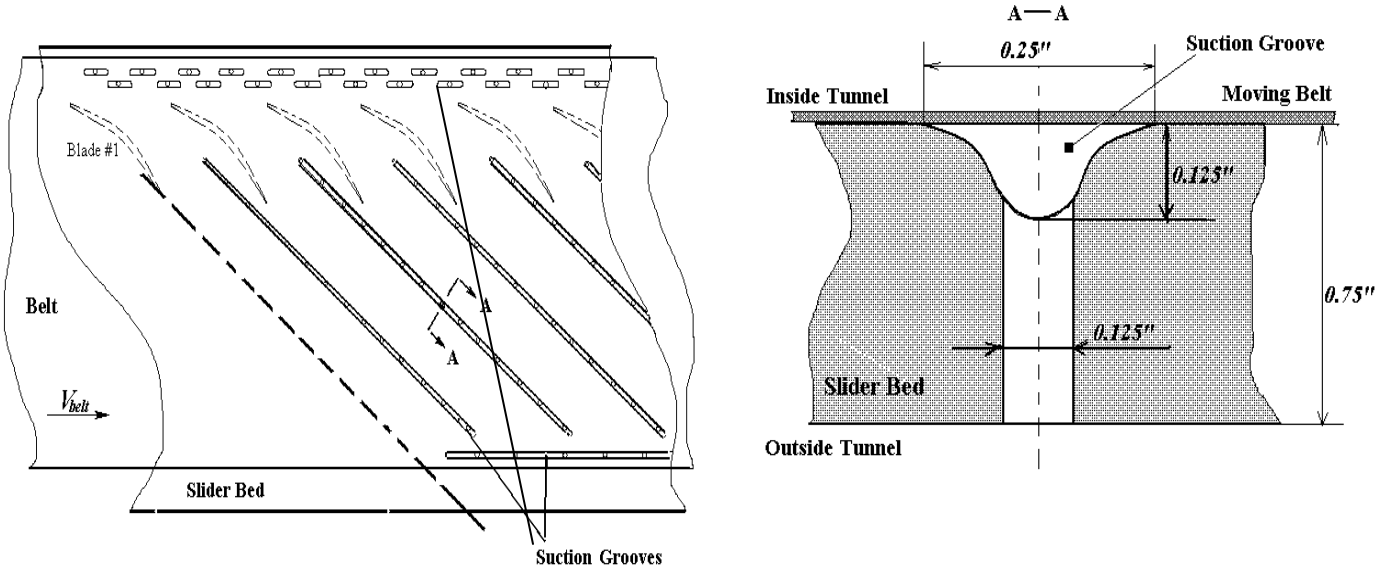

Figure 2-13 Layout and structure of the suction grooves

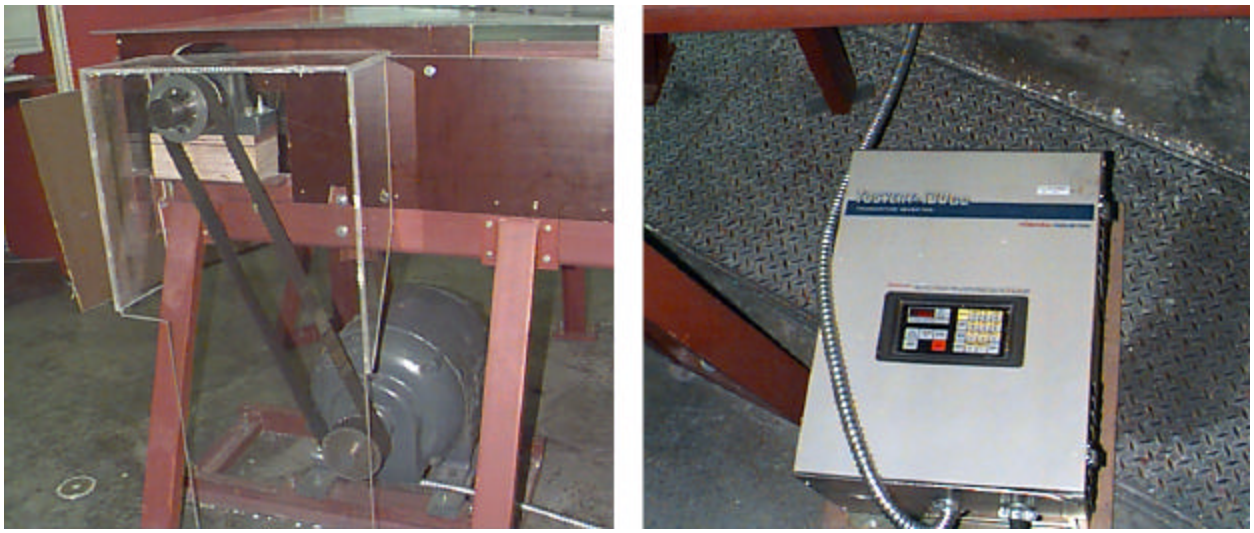

Figure 2-14 Motor and Motor Controller

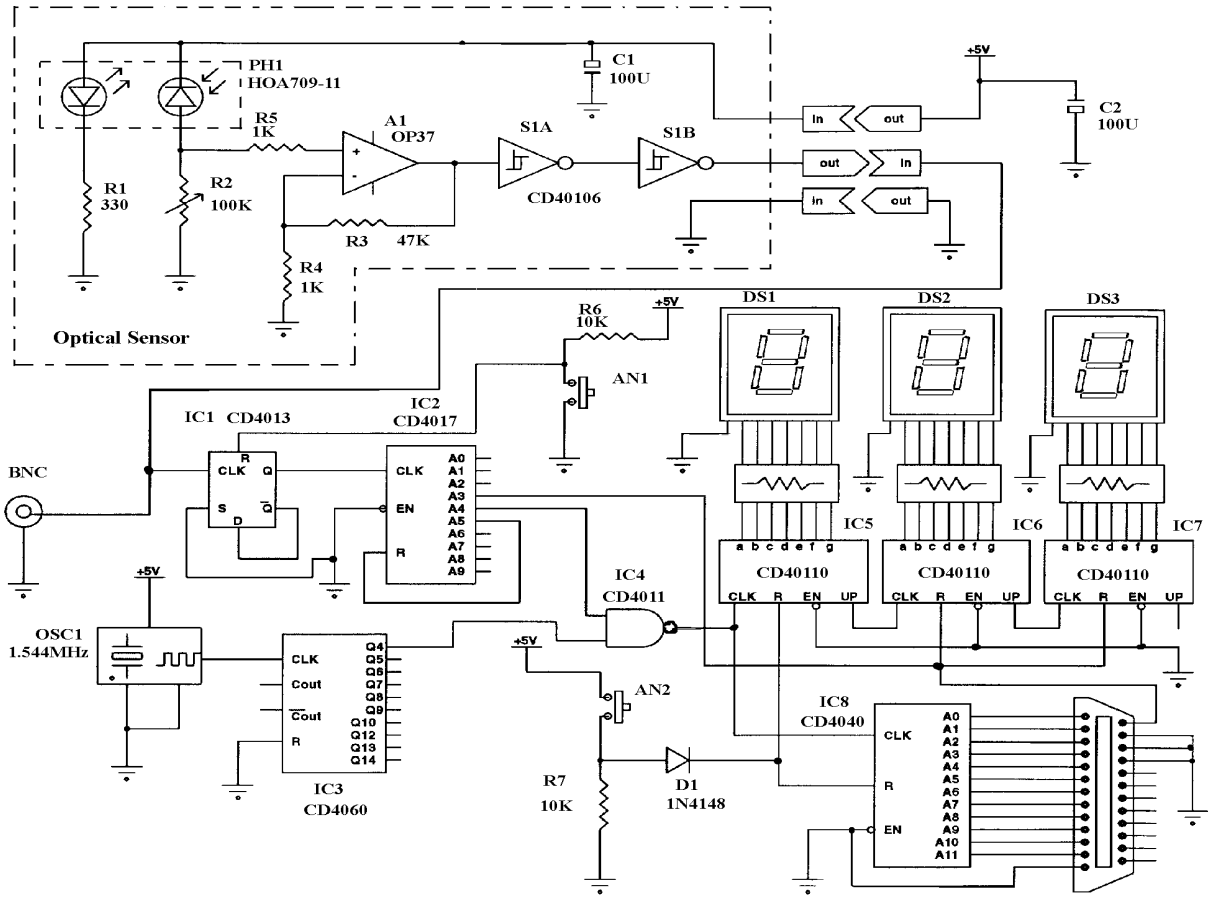

Figure 2-15 Schematic of the Belt speed meter Circuit

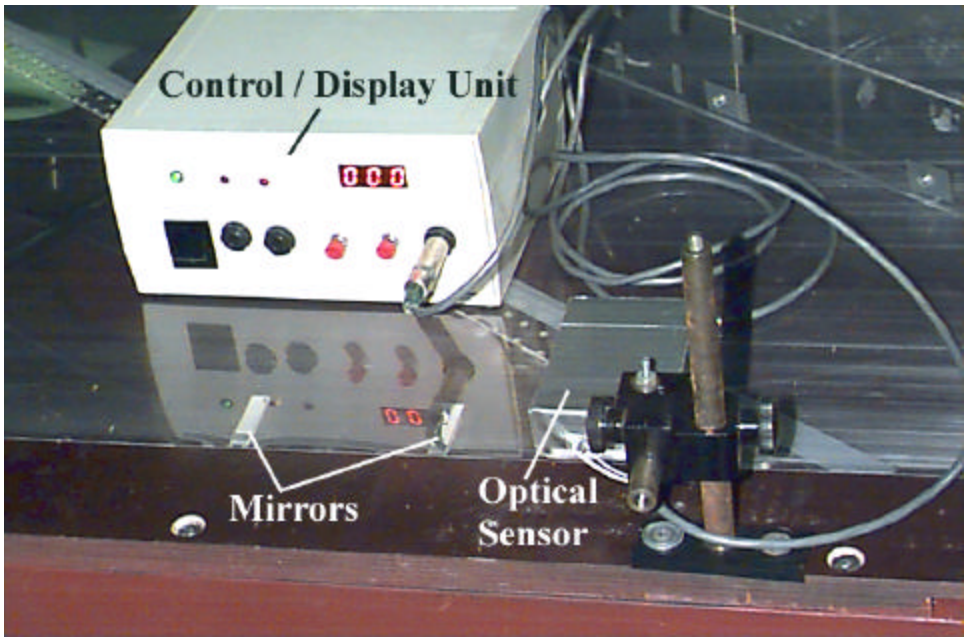

Figure 2-16 The Speed Meter

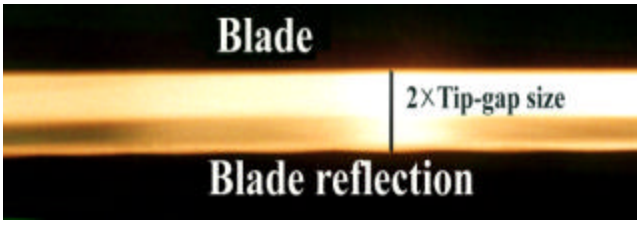

Figure 2-17 Photograph of blade 5 tip-gap (with belt and wind and wind tunnel running)

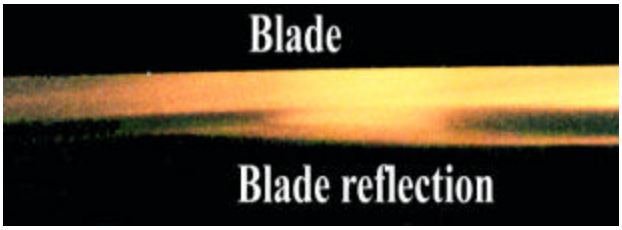

Figure 2-18 Photograph of blade 5 tip-gap (with tunnel off)

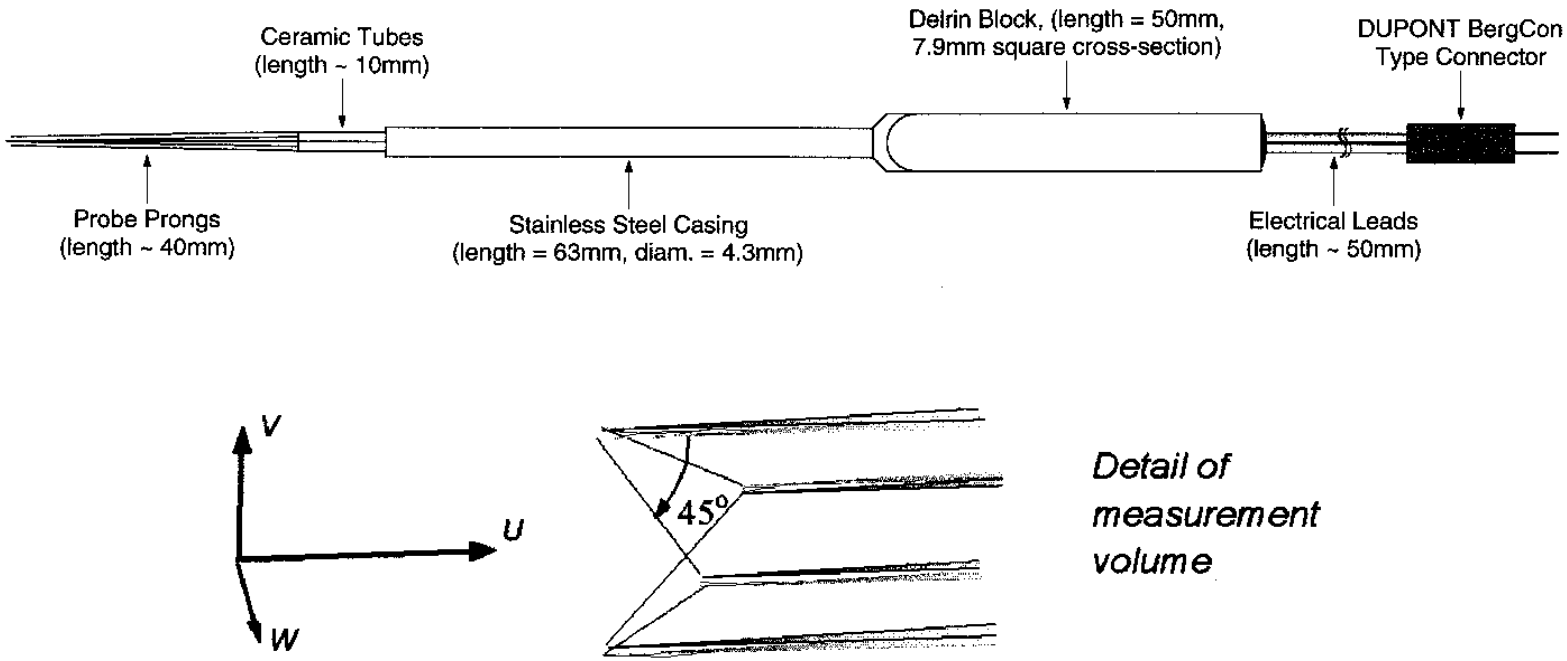

Figure 2.19 Schematic diagram of hot wire and measurement volume

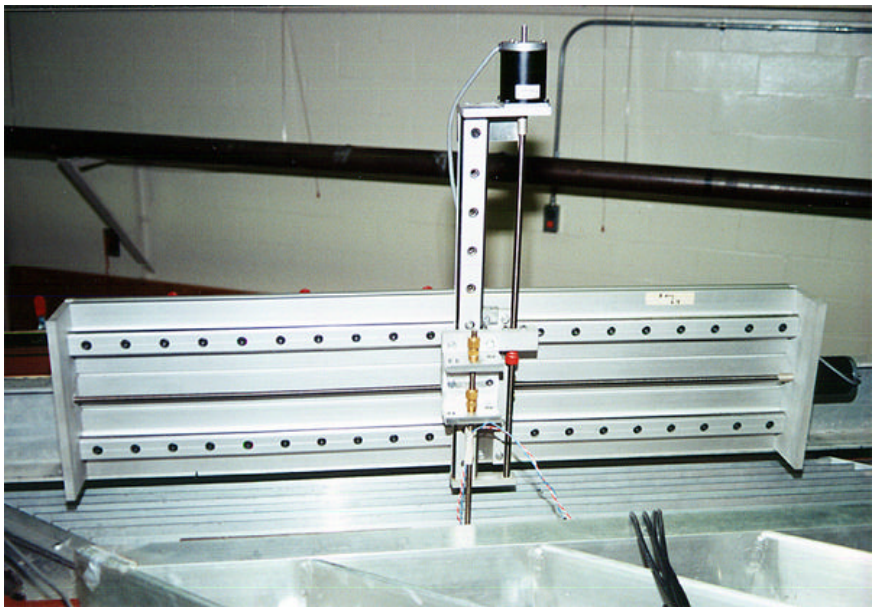

Figure 2-20 The Traverse System

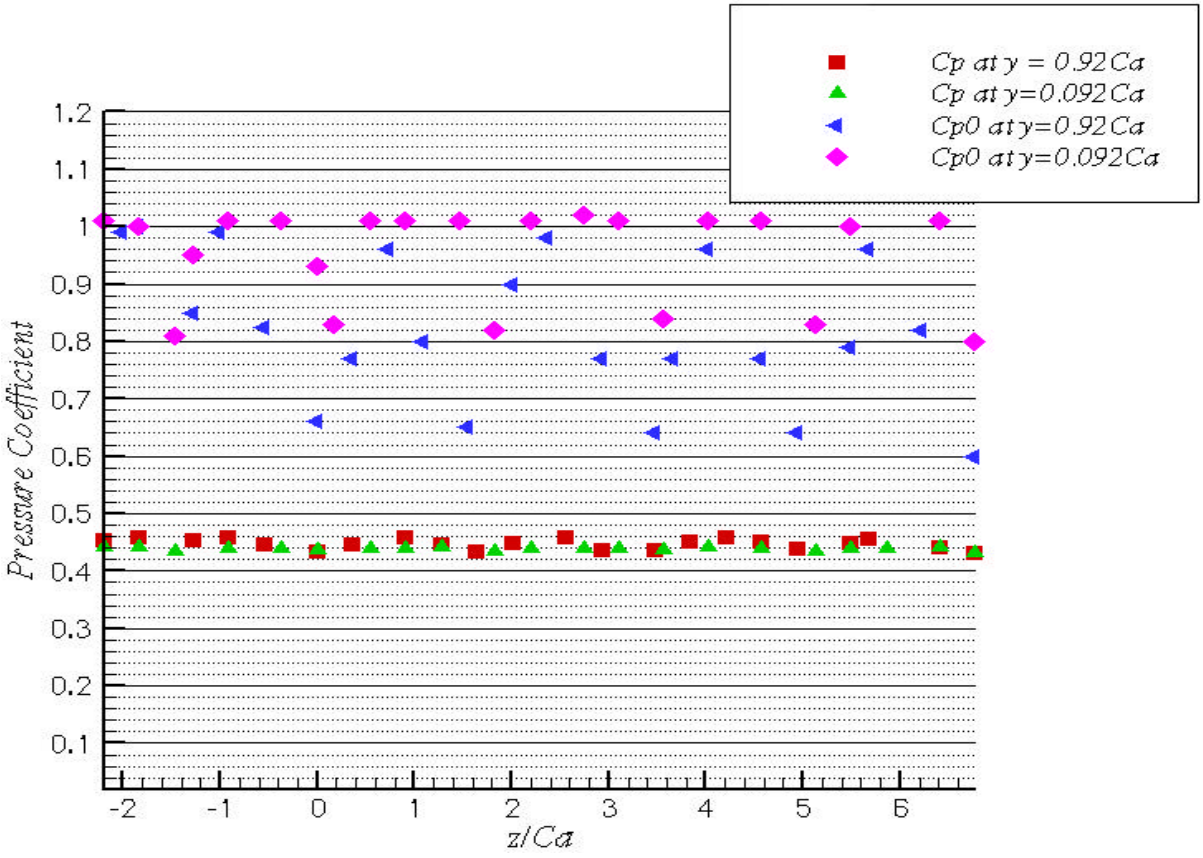

Figure 2-21 Results of the Pressure Measurements

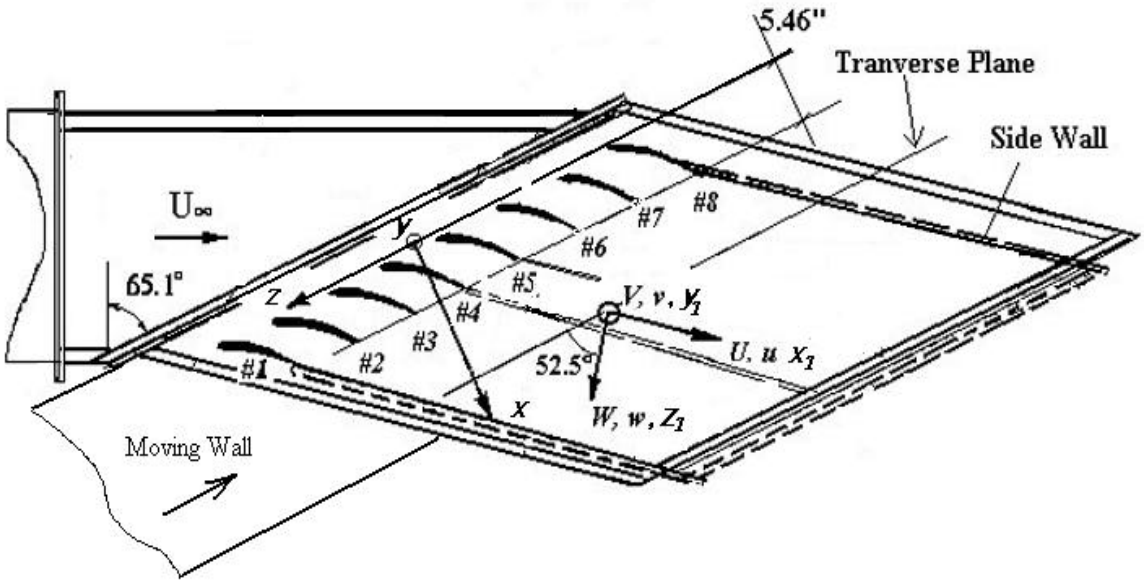

Figure 3-1 The Coordinate System

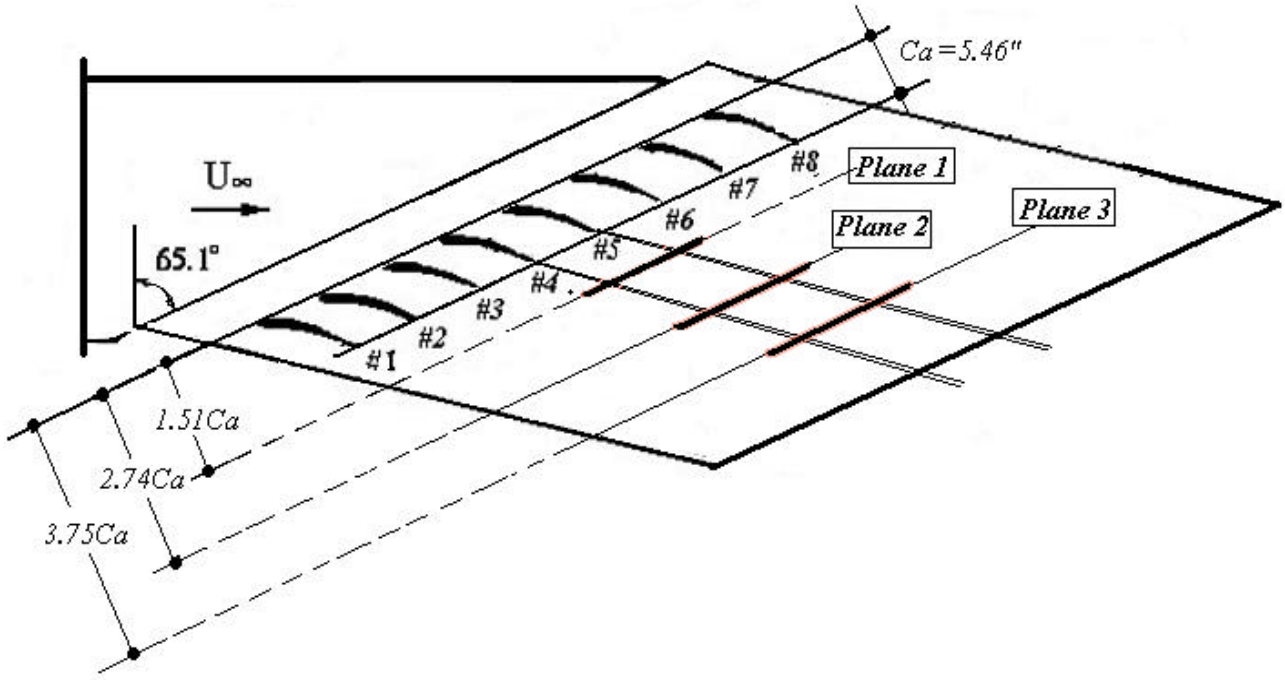

Figure 3-2 Position of Measurement Planes

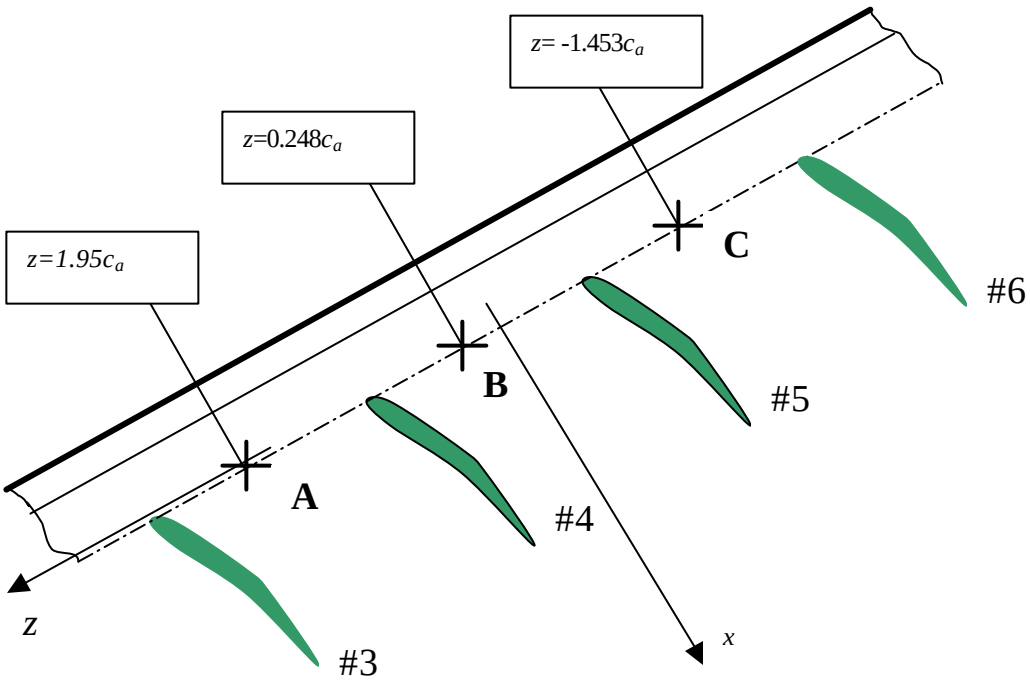

Figure 3-3 The Positions of Boundary Layer Measurements

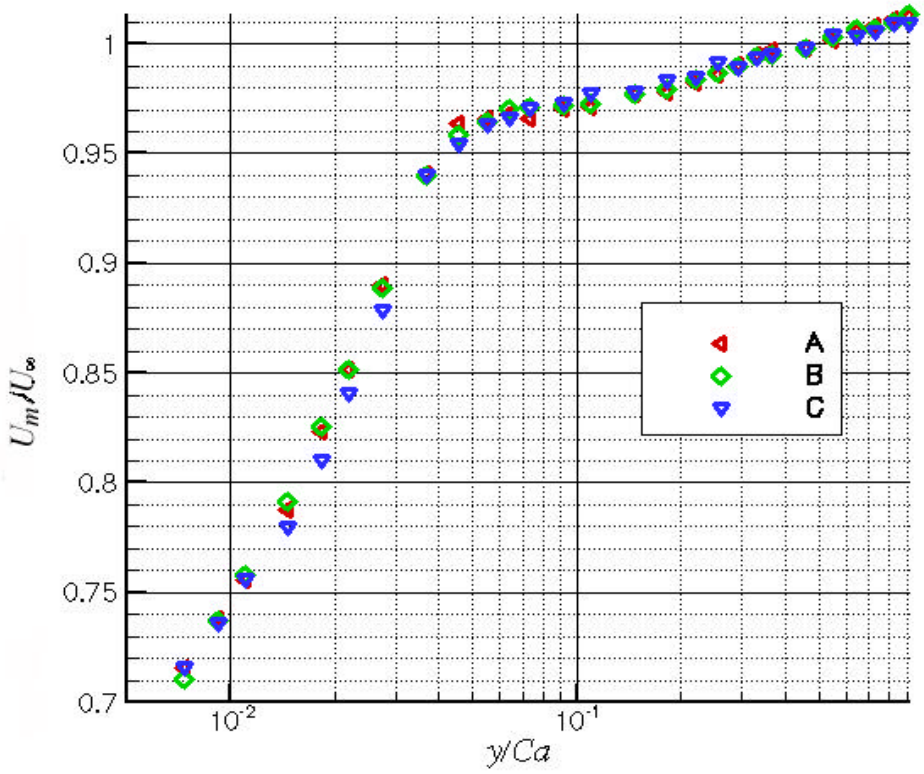

Figure 3-4 Boundary Layer Profile at 3 Positions
A: z/ c_a =1.95, B: z/ c_a =0.248 , C: z/ c_a =-1.453

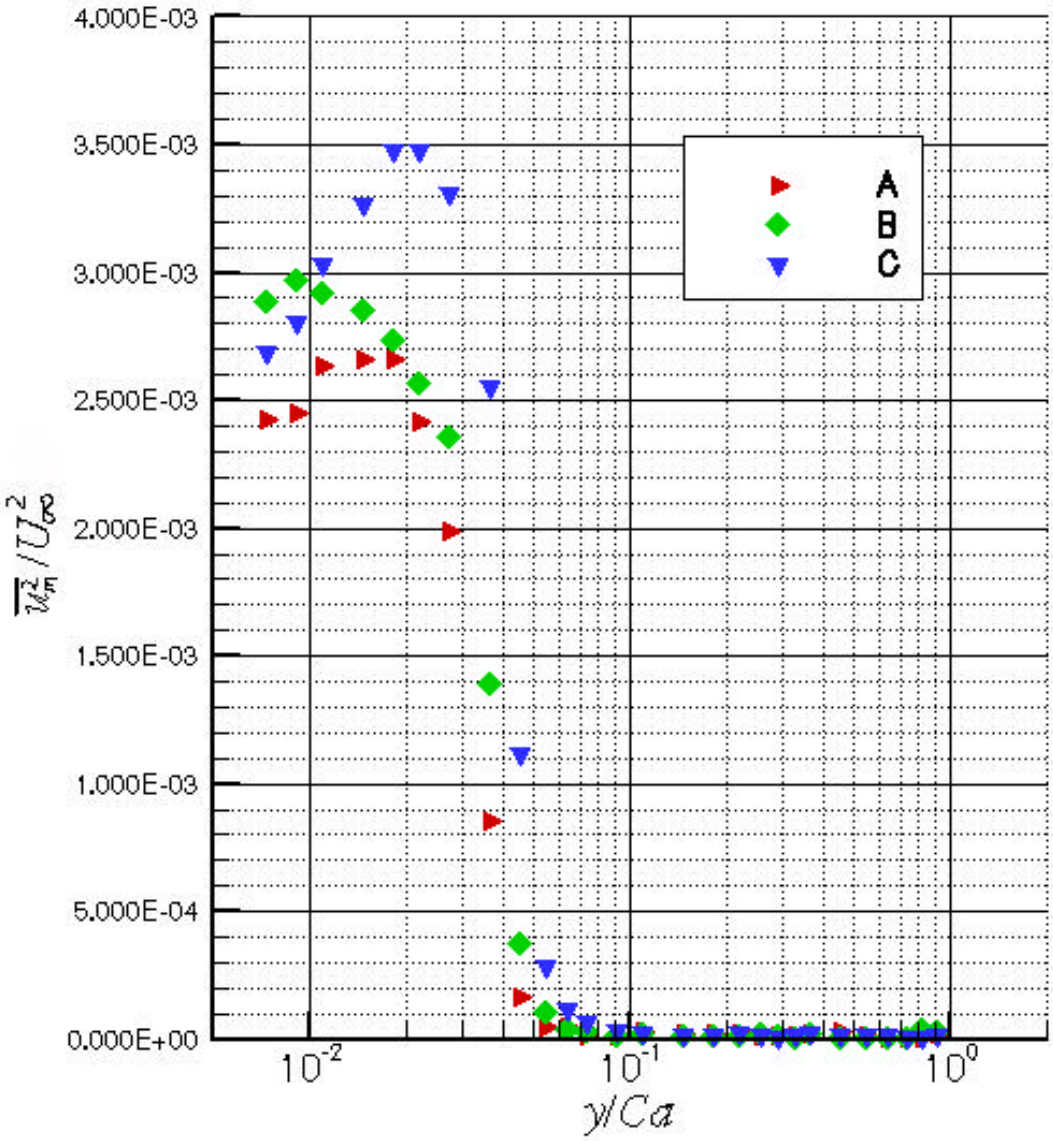

Figure 3-5 Turbulence Intensity Profiles
A: z/ c_a =1.95, B: z/ c_a =0.248 , C: z/ c_a =-1.453

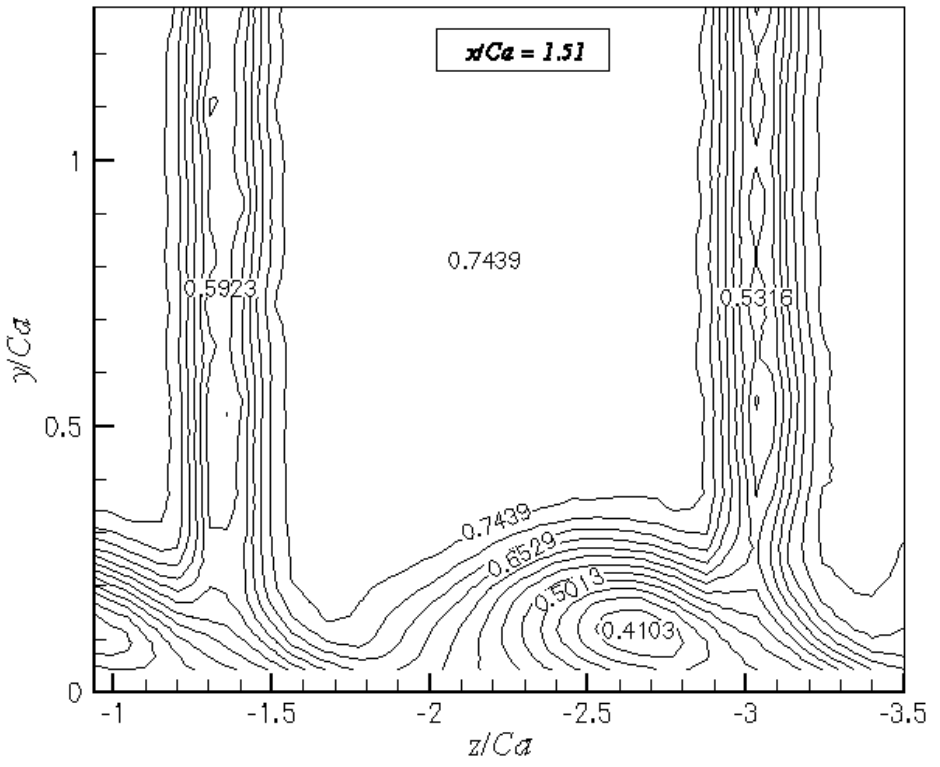

(a)

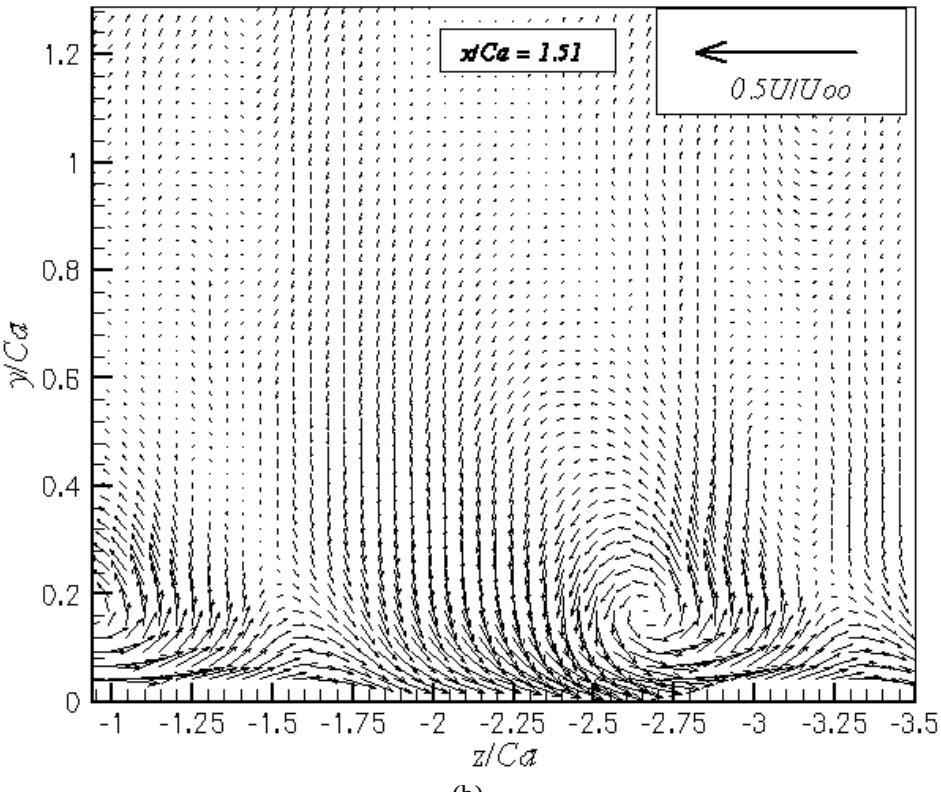

(b)

Figure 3-6 Mean Velocity at *x/Ca=1.51*

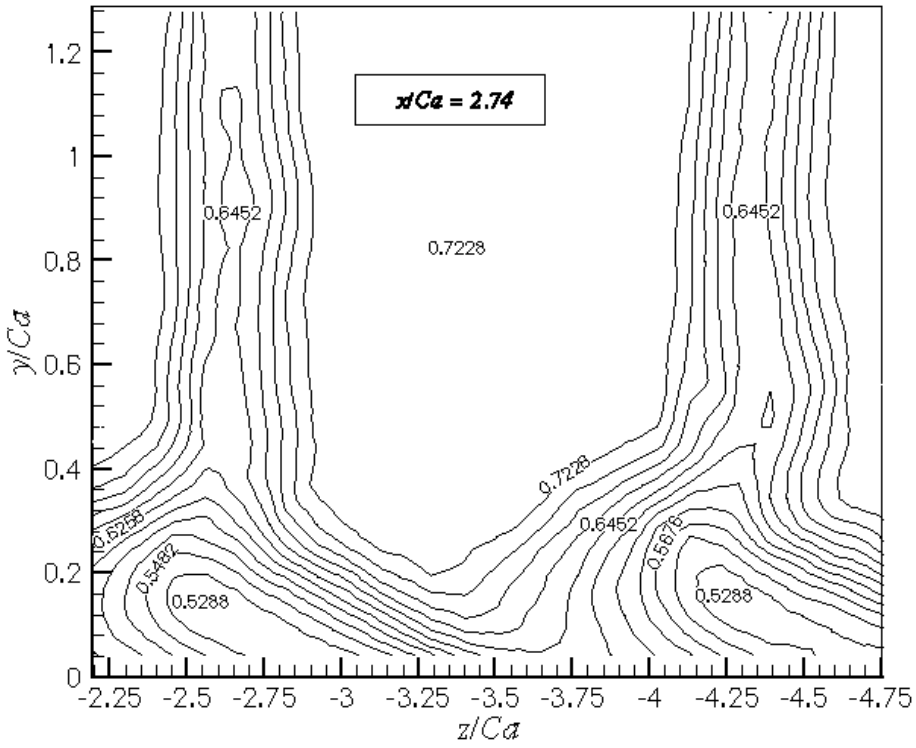

(a)

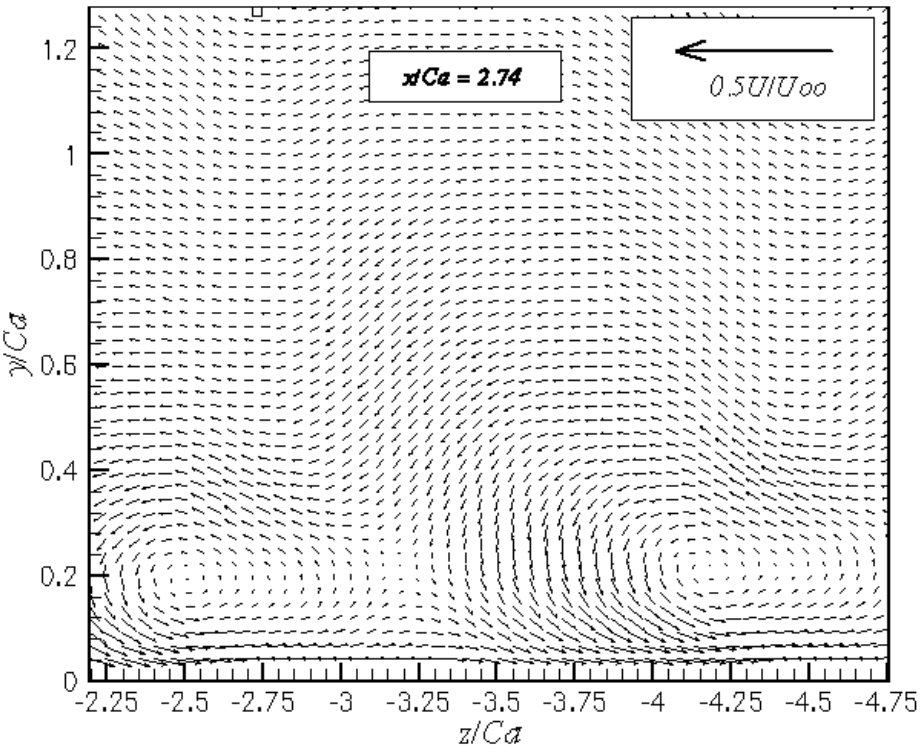

(b)

Figure 3-7 Mean Velocity at *x/Ca=2.74*

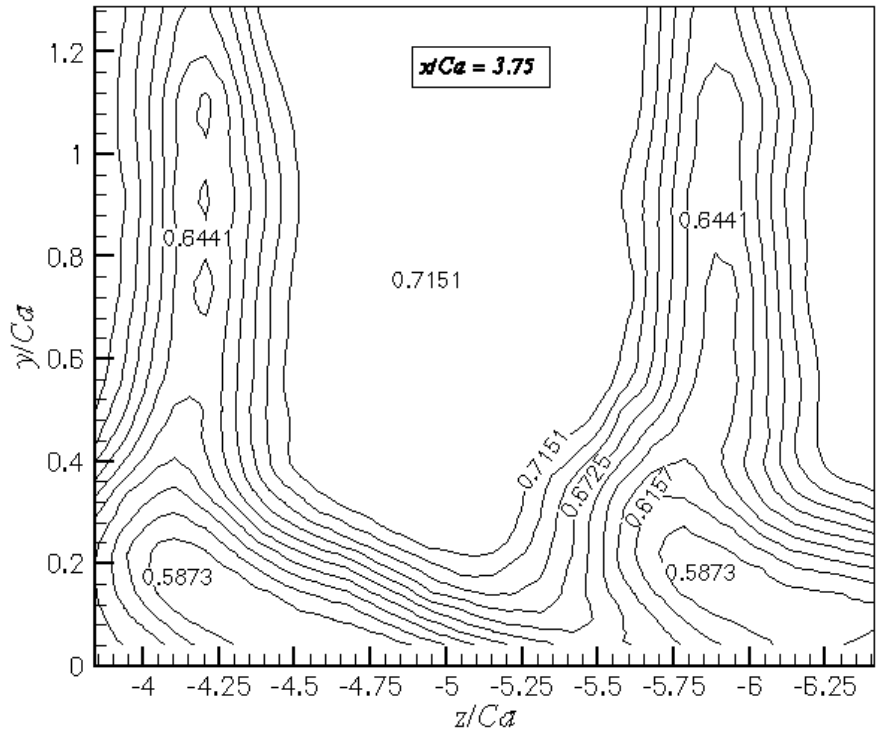

(a)

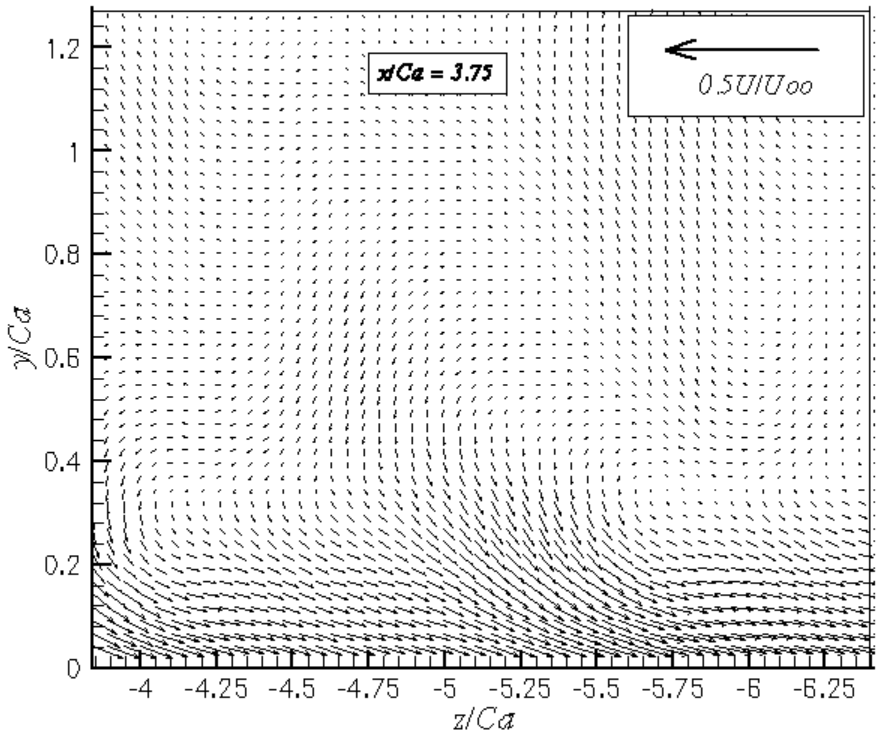

(b)

Figure 3-8 Mean Velocity at *x/Ca=3.75*

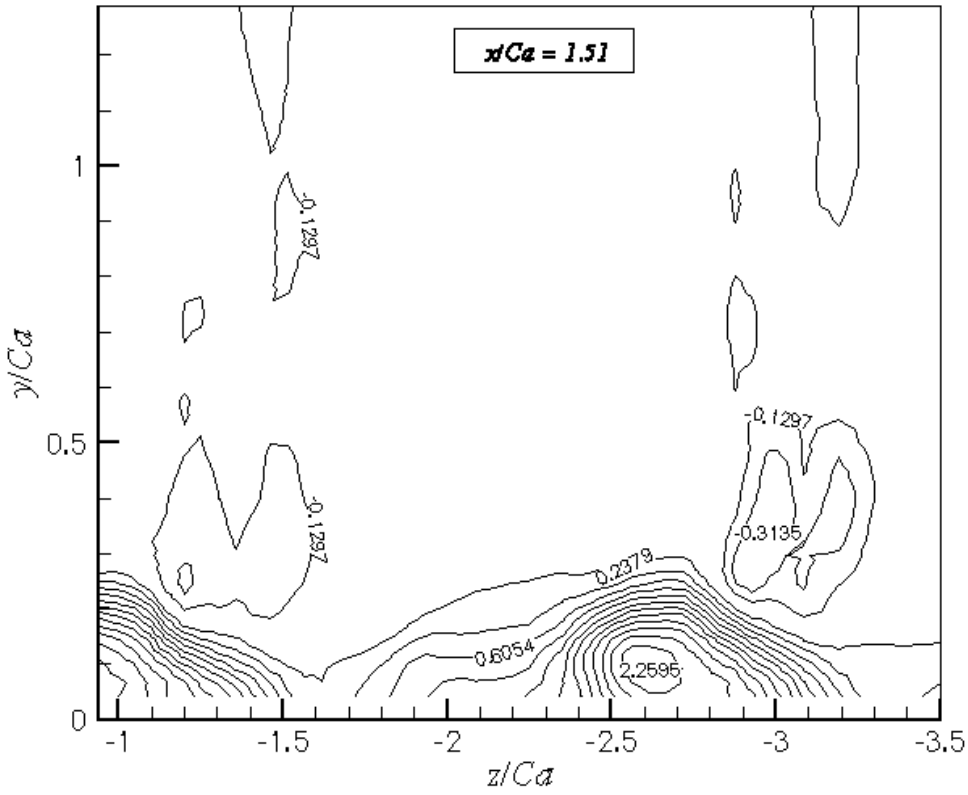

Figure 3-9 Mean Streamwise Vorticity at *x/Ca=1.51*

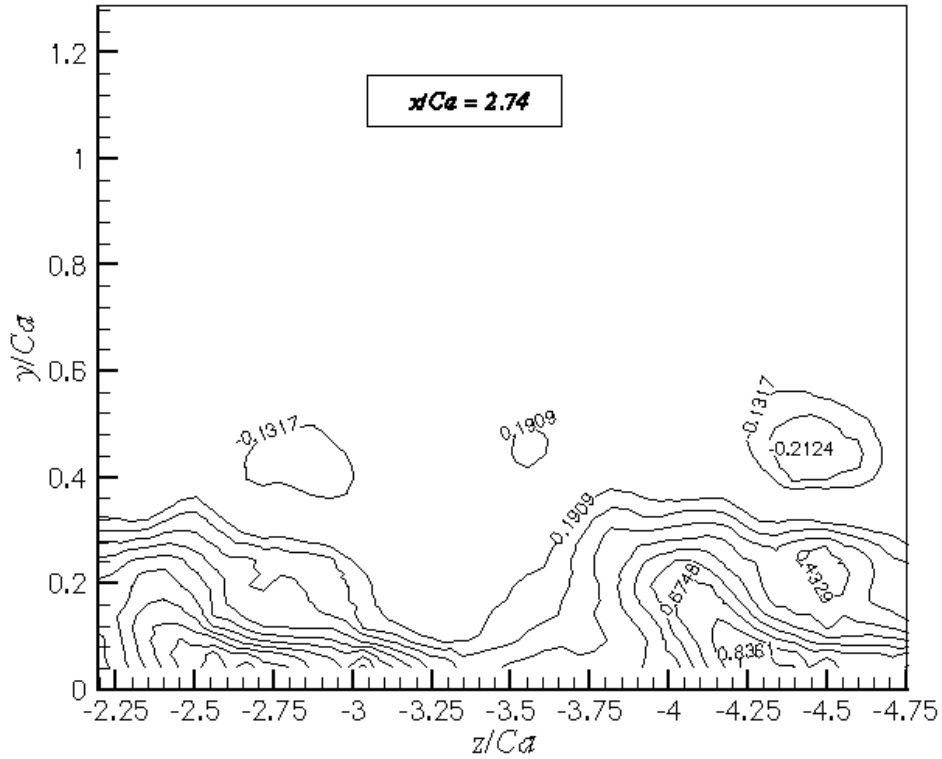

Figure 3-10 Mean Streamwise Vorticity at *x/Ca=2.74*

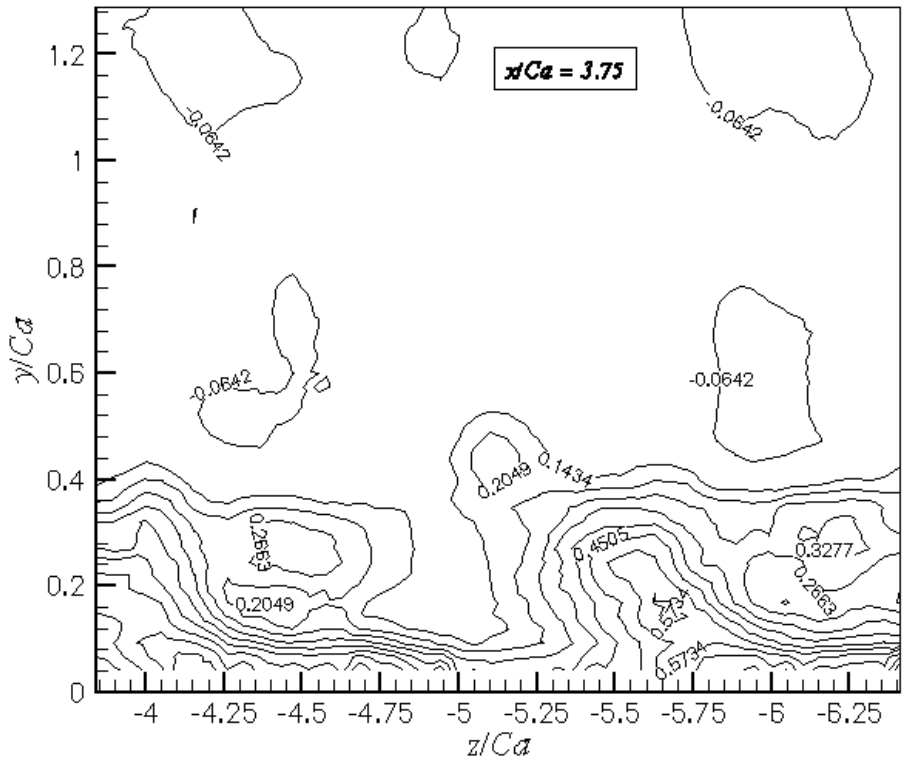

Figure 3-11 Mean Streamwise Vorticity at *x/Ca=3.75*

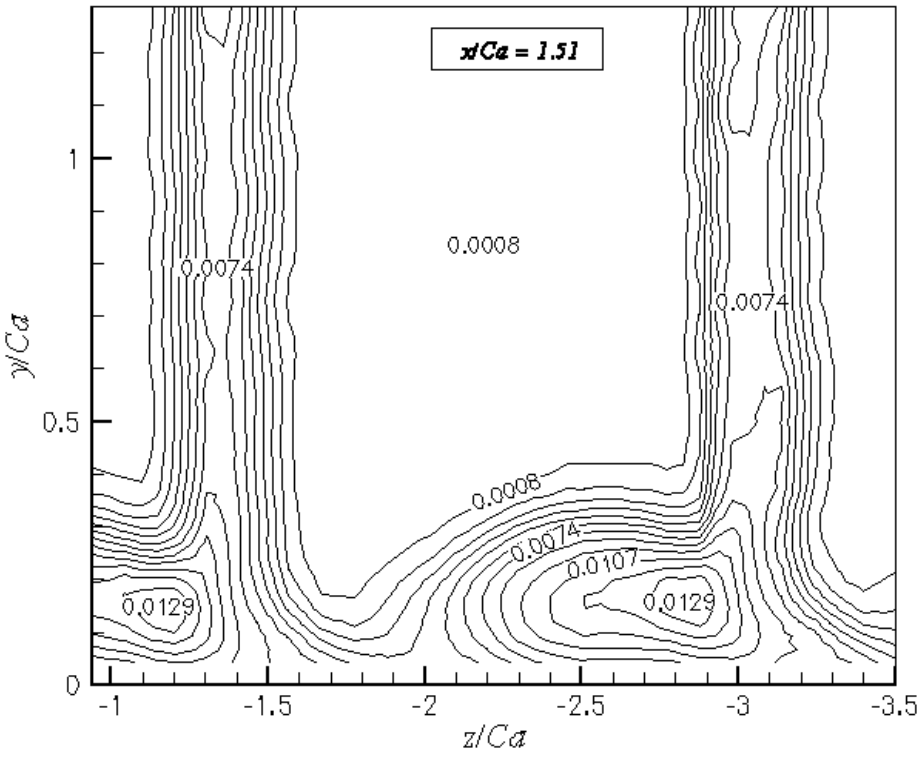

Figure 3-12 *tke* Distribution at *x/Ca =1.51*

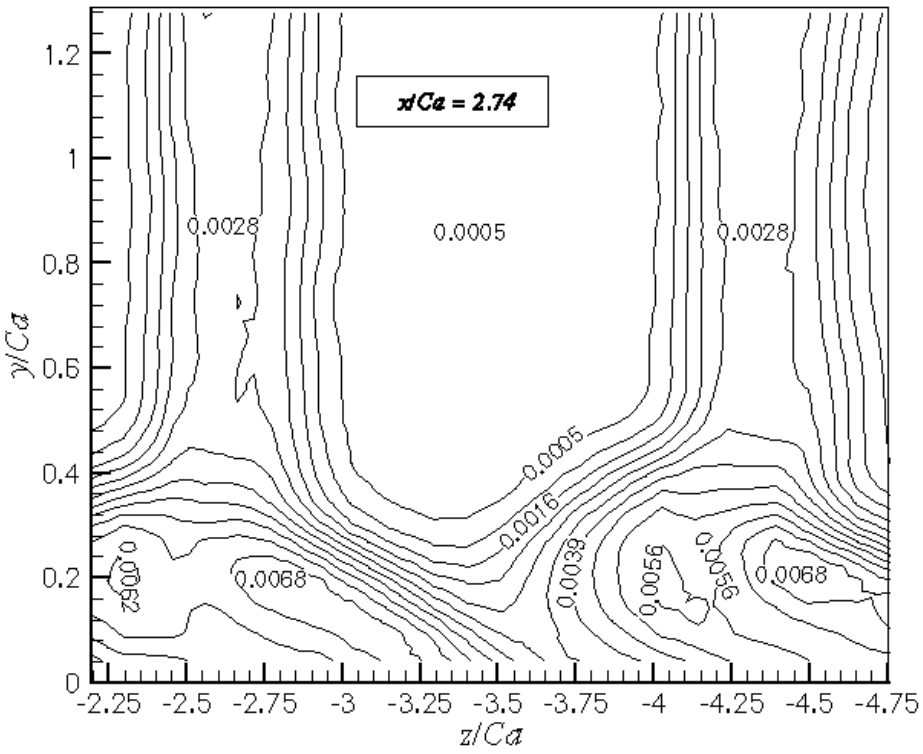

Figure 3-13 *tke* Distribution at *x/Ca =2.74* (Normalized on U_∞^2)

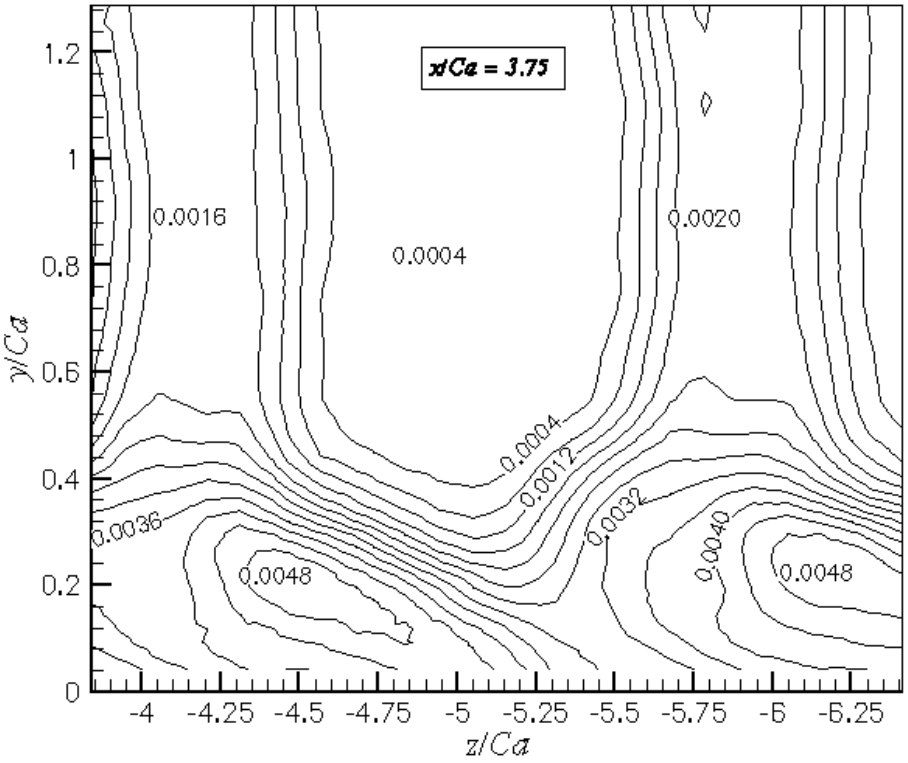

Figure 3-14 *tke* Distribution at *x/ca =3.75* (Normalized on U_∞^2)

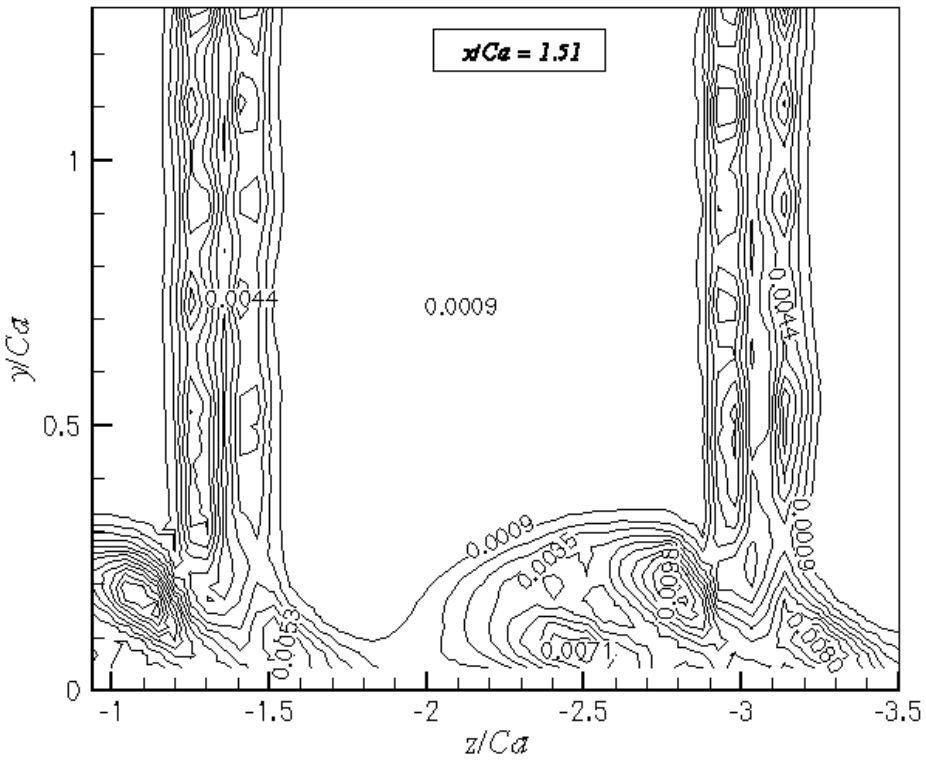

Figure 3-15 *tke* Production at *x/Ca =1.51*(Normalized on U_∞^2)

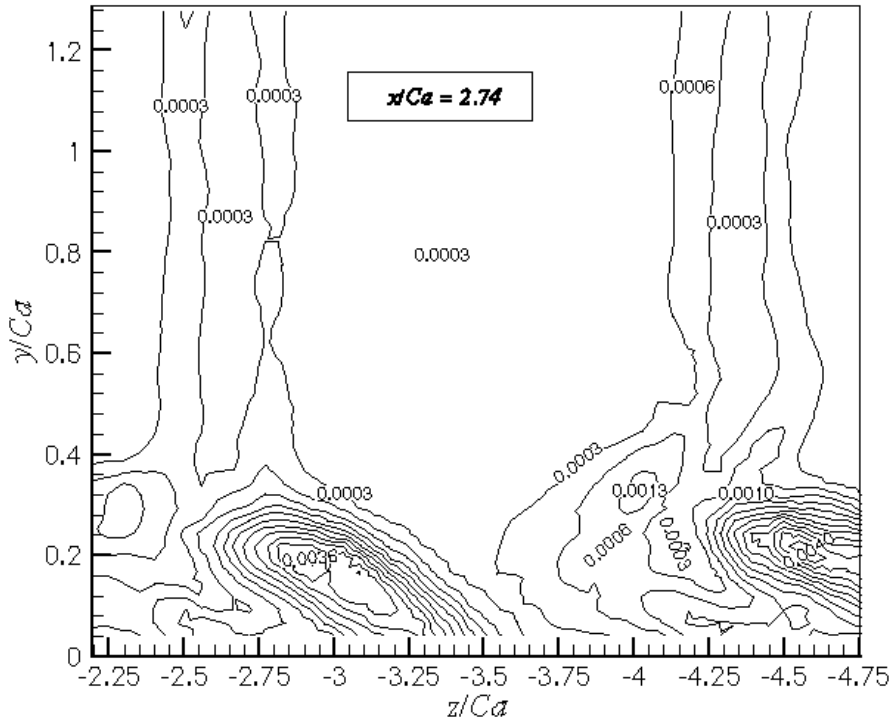

Figure 3-16 *tke* Production at *x/Ca =2.74*

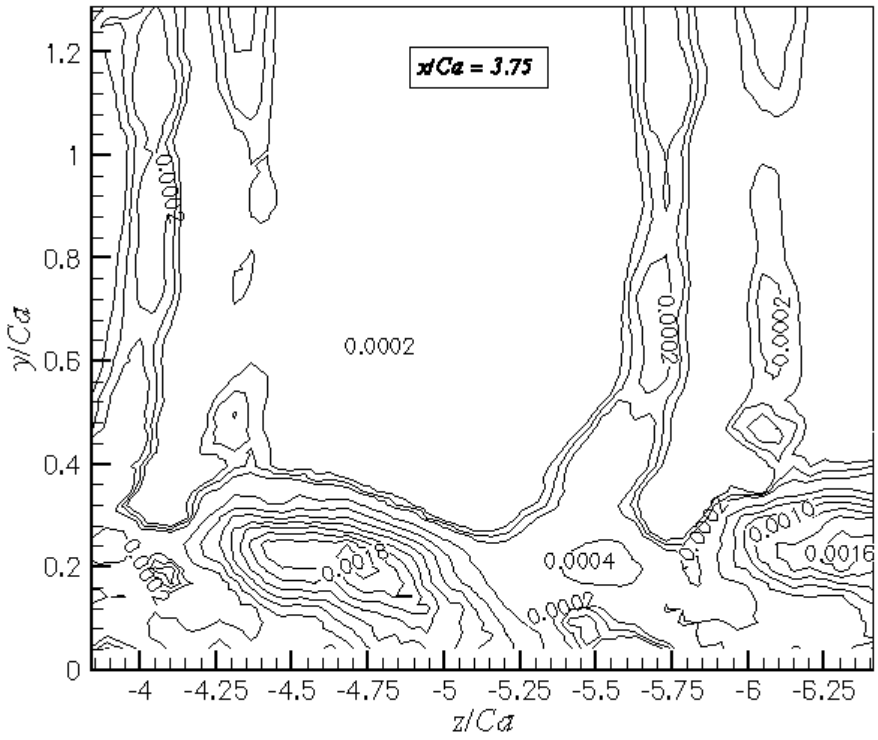

Figure 3-17 *tke* Production at *x/Ca =3.75*

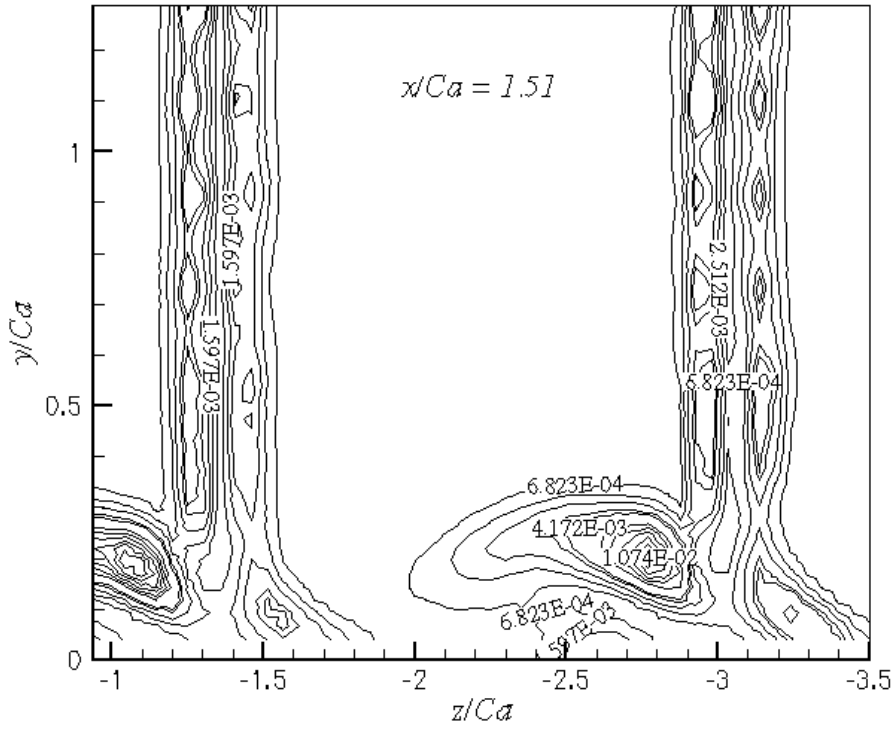

(a) Streamwise Contribution

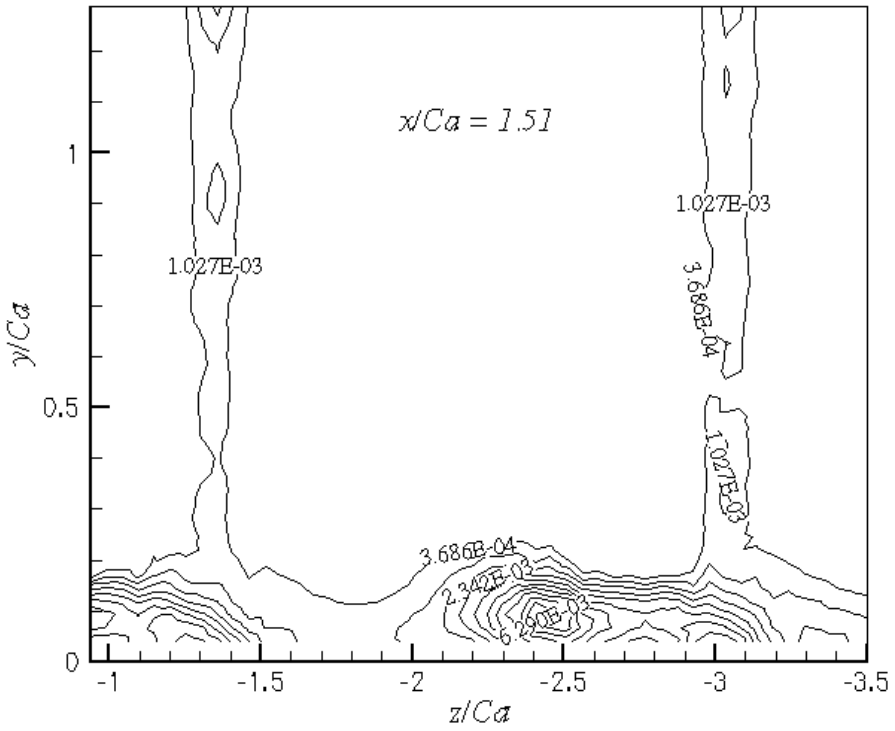

(b) Crossflow Contribution

Figure 3-18 Streamwise and Crossflow Contributions to tke production at $x/c_a = 1.51$

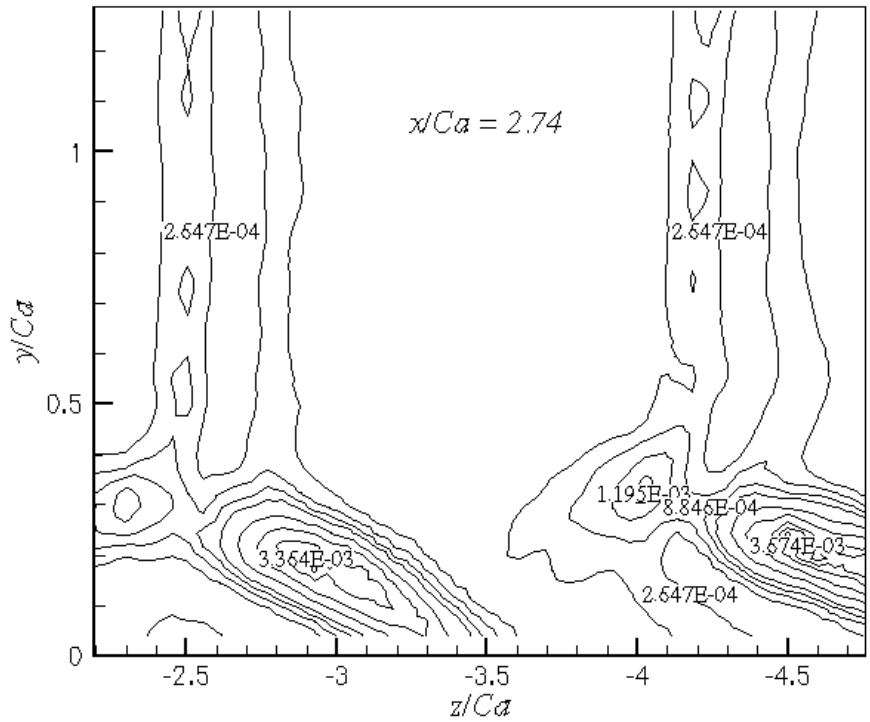

(a) Streamwise Contribution

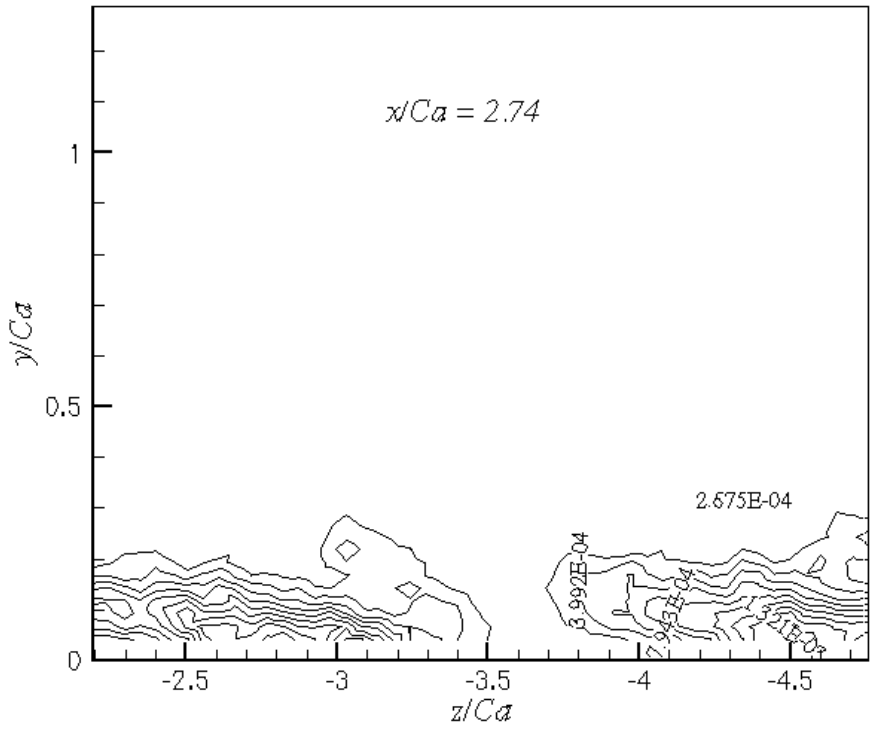

(b) Crossflow Contribution

Figure 3-19 Streamwise and Crossflow Contributions to tke production at $x/c_a = 2.74$

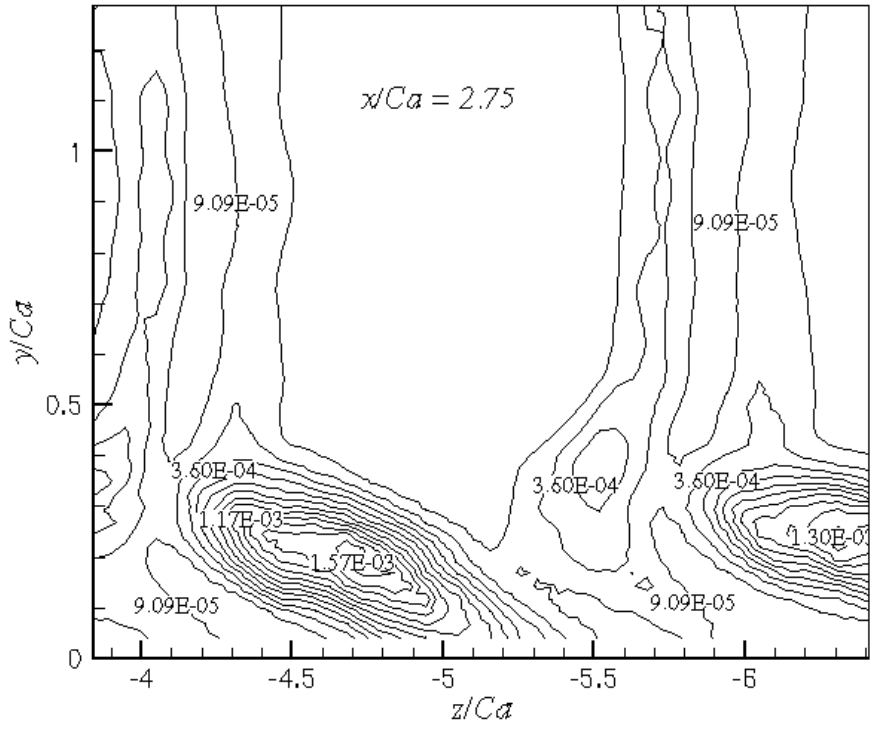

(a) Streamwise Contribution

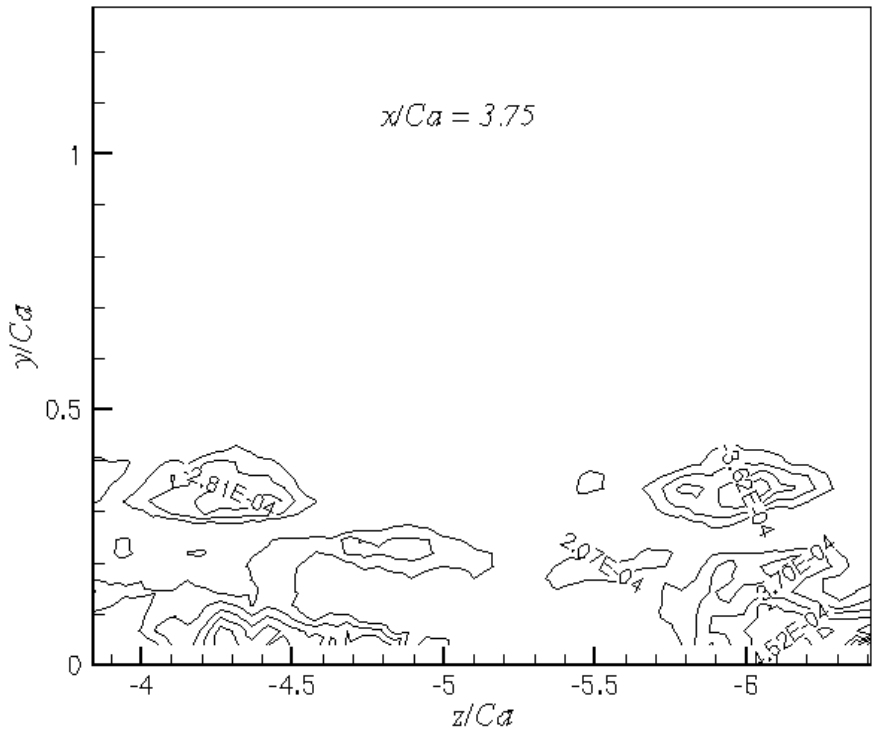

(b) Crossflow Contribution

Figure 3-20 Streamwise and Crossflow Contributions to tke production at $x/c_a = 3.75$

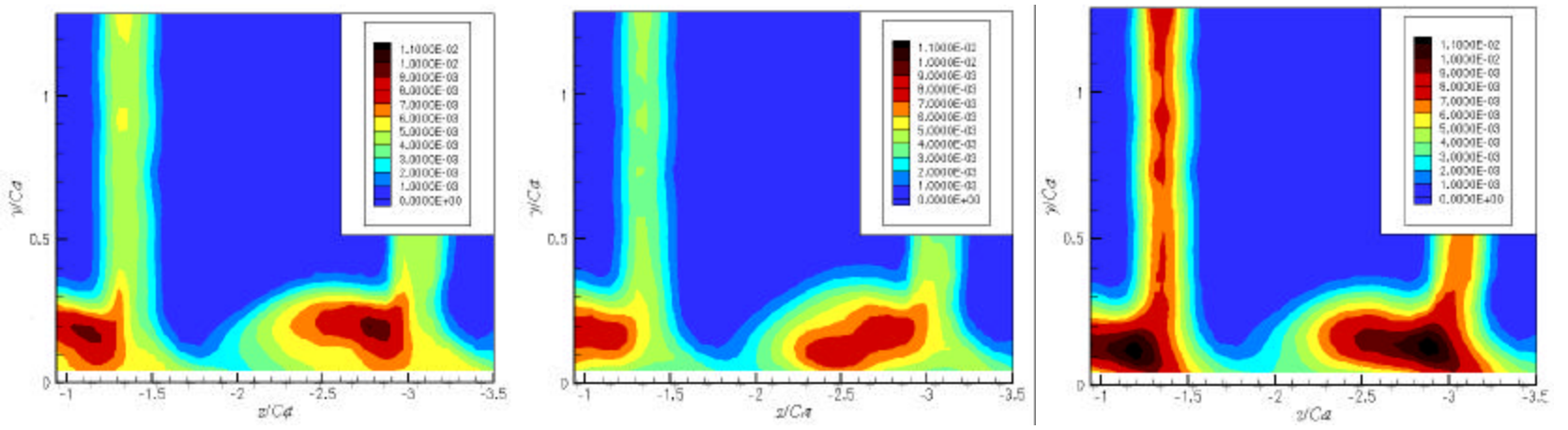

(a) $\overline{u^2}$ (b) $\overline{v^2}$ (c) $\overline{w^2}$

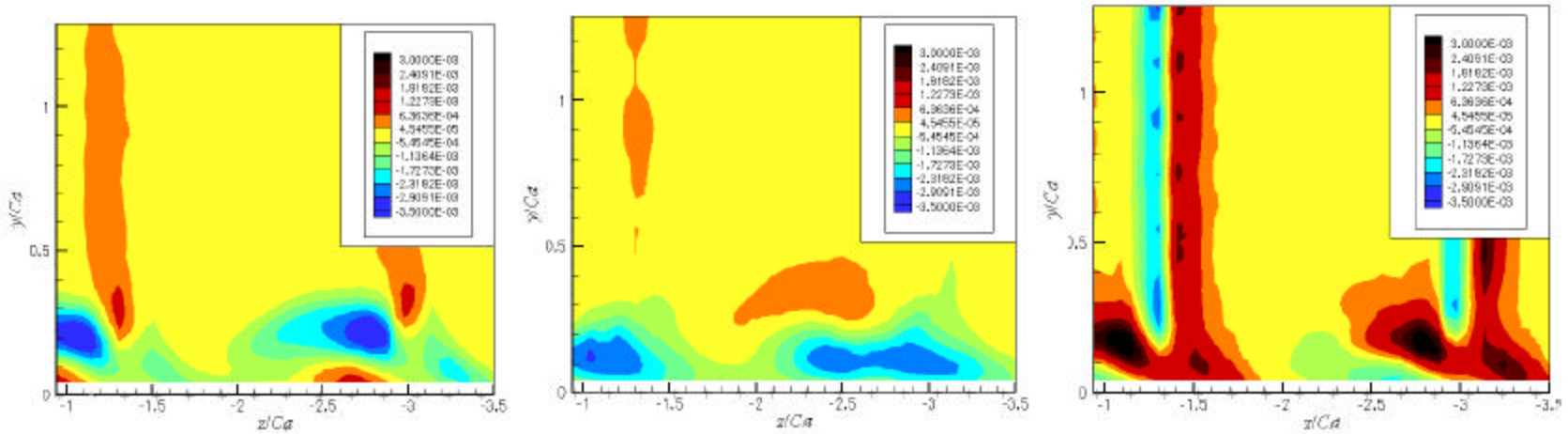

(d) $\overline{uv}$ (e) $\overline{vw}$ (f) $\overline{uw}$

Figure 3-21 Reynolds Stress at *x/Ca = 1.51*

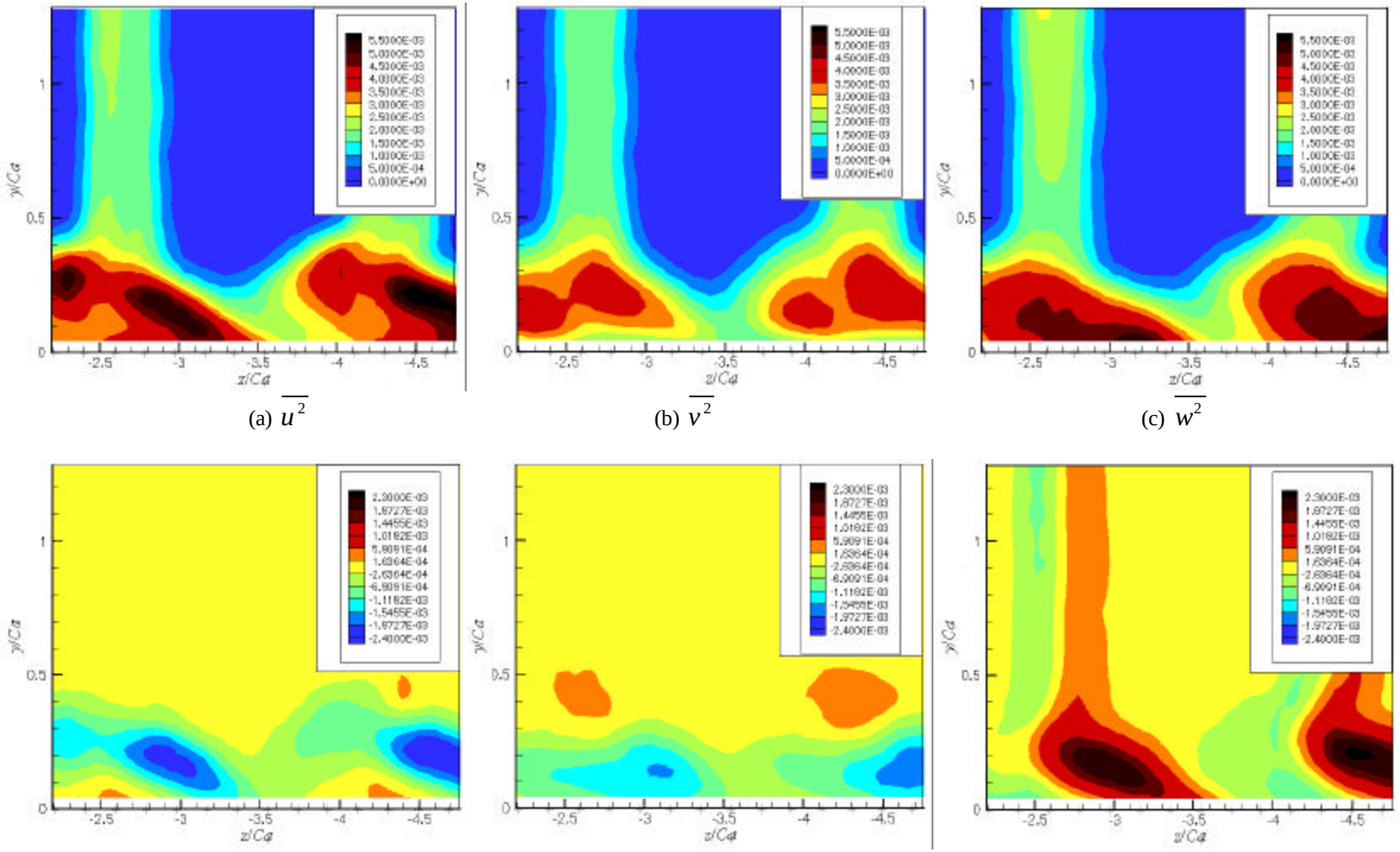

(a) $\overline{u^2}$ (b) $\overline{v^2}$ (c) $\overline{w^2}$

(d) $\overline{uv}$ (e) $\overline{vw}$ (f) $\overline{uw}$

Figure 3-22 Reynolds Stress at *x/Ca = 2.74*

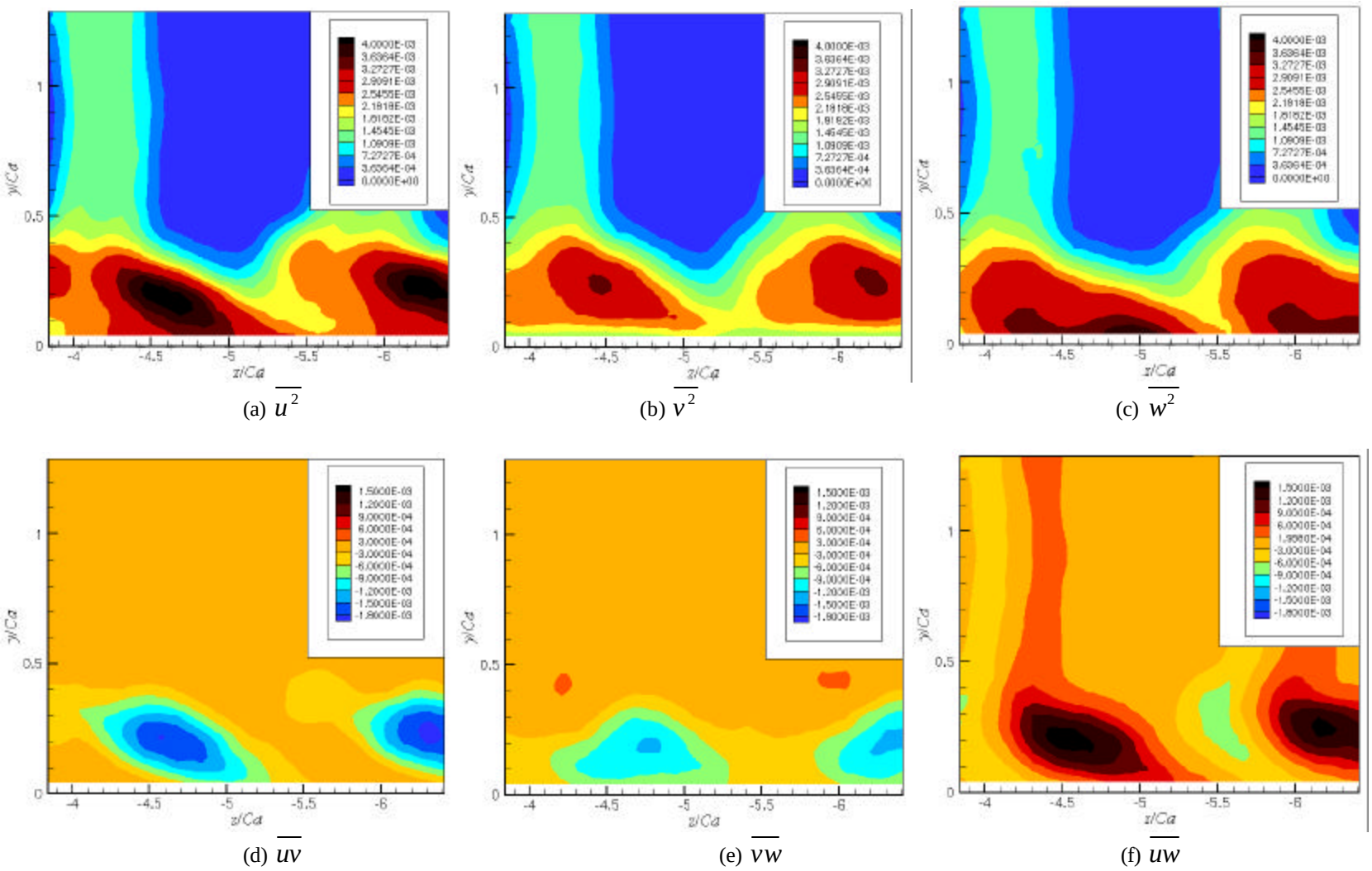

(a) $\overline{u^2}$ (b) $\overline{v^2}$ (c) $\overline{w^2}$

(d) $\overline{uv}$ (e) $\overline{vw}$ (f) $\overline{uw}$

Figure 3-23 Reynolds Stress at $x/Ca = 3.75$

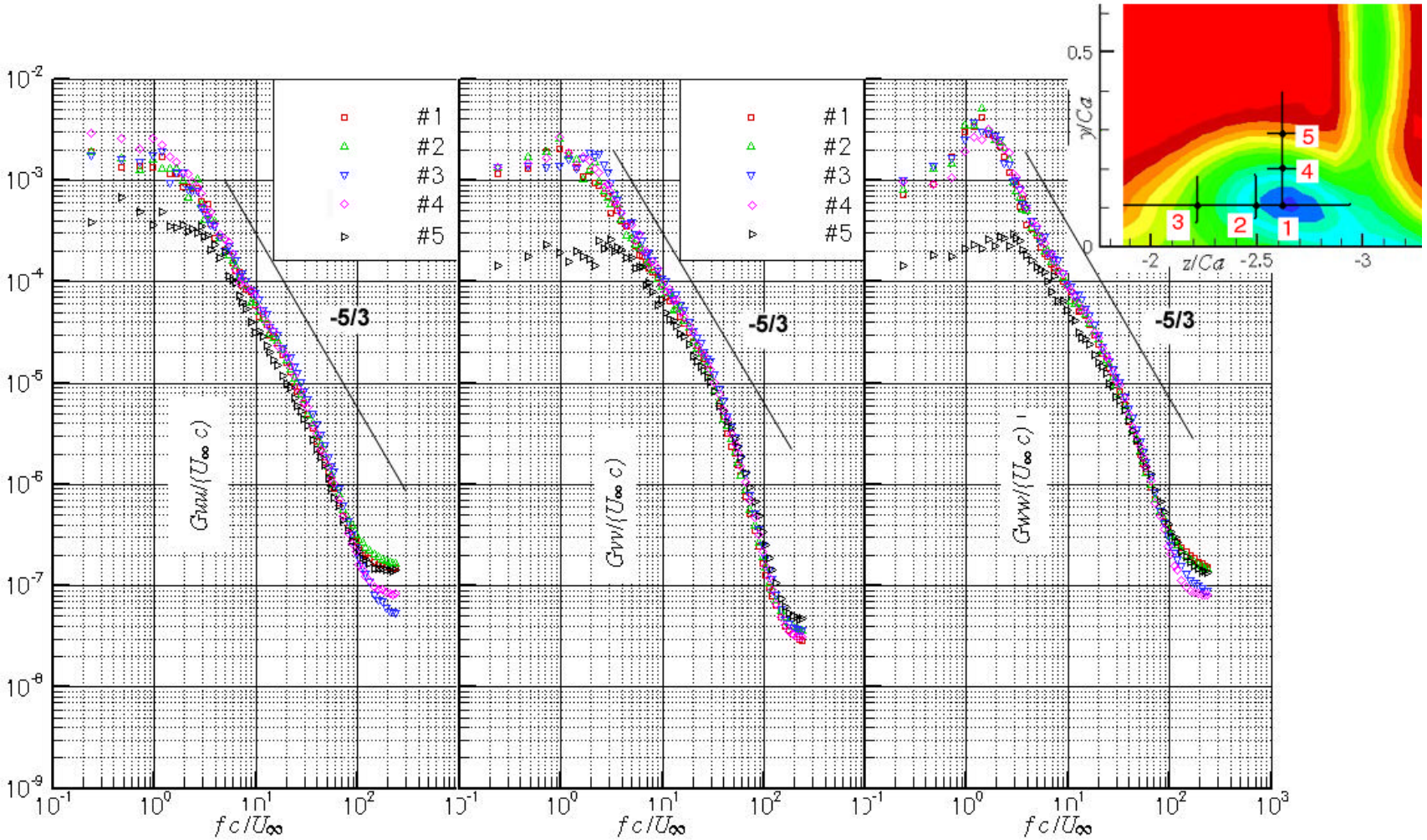

Figure 3-24 Autospectra at *x/Ca = 1.51*

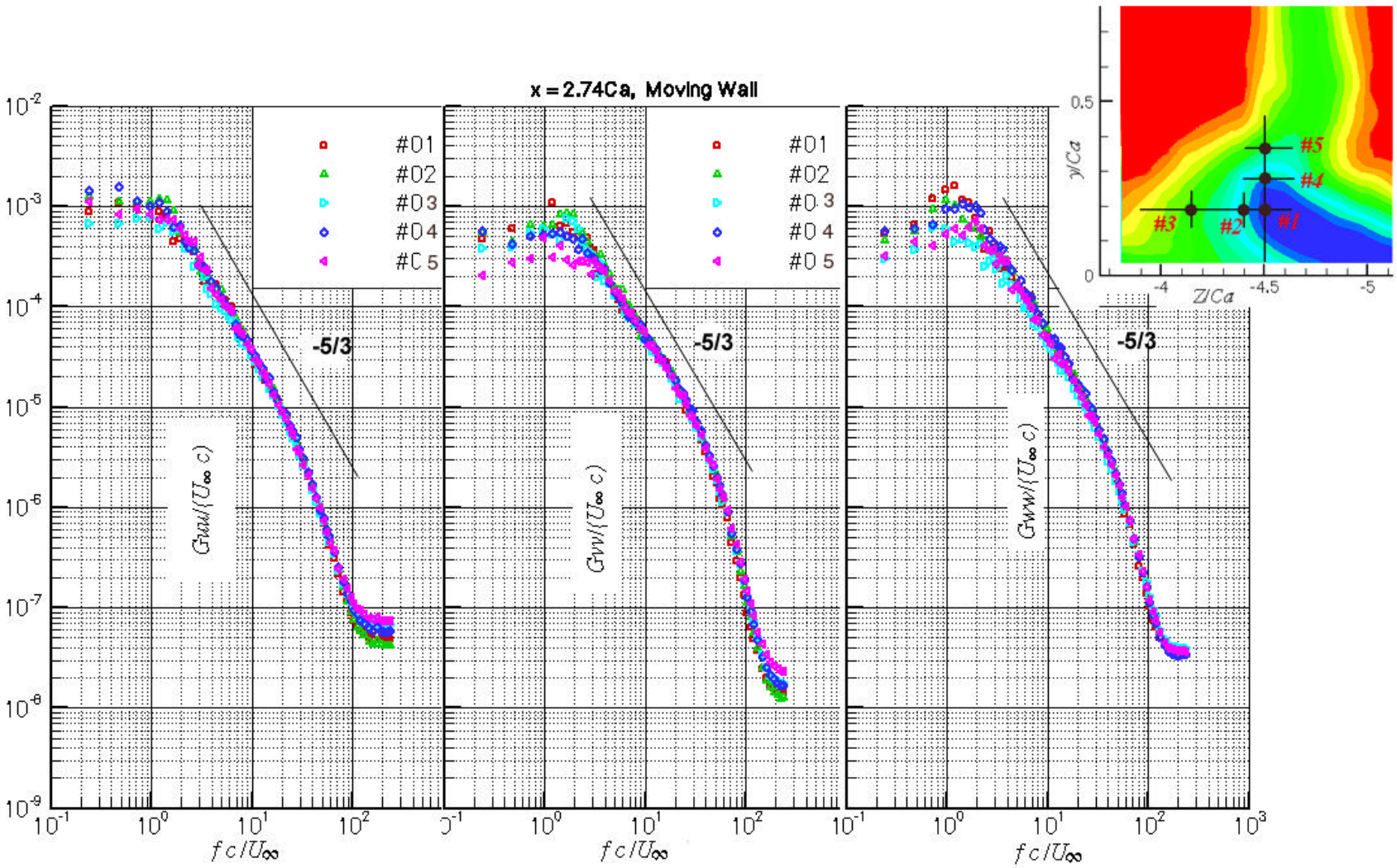

Figure 3-25 Autospectra at *x/Ca = 2.74*

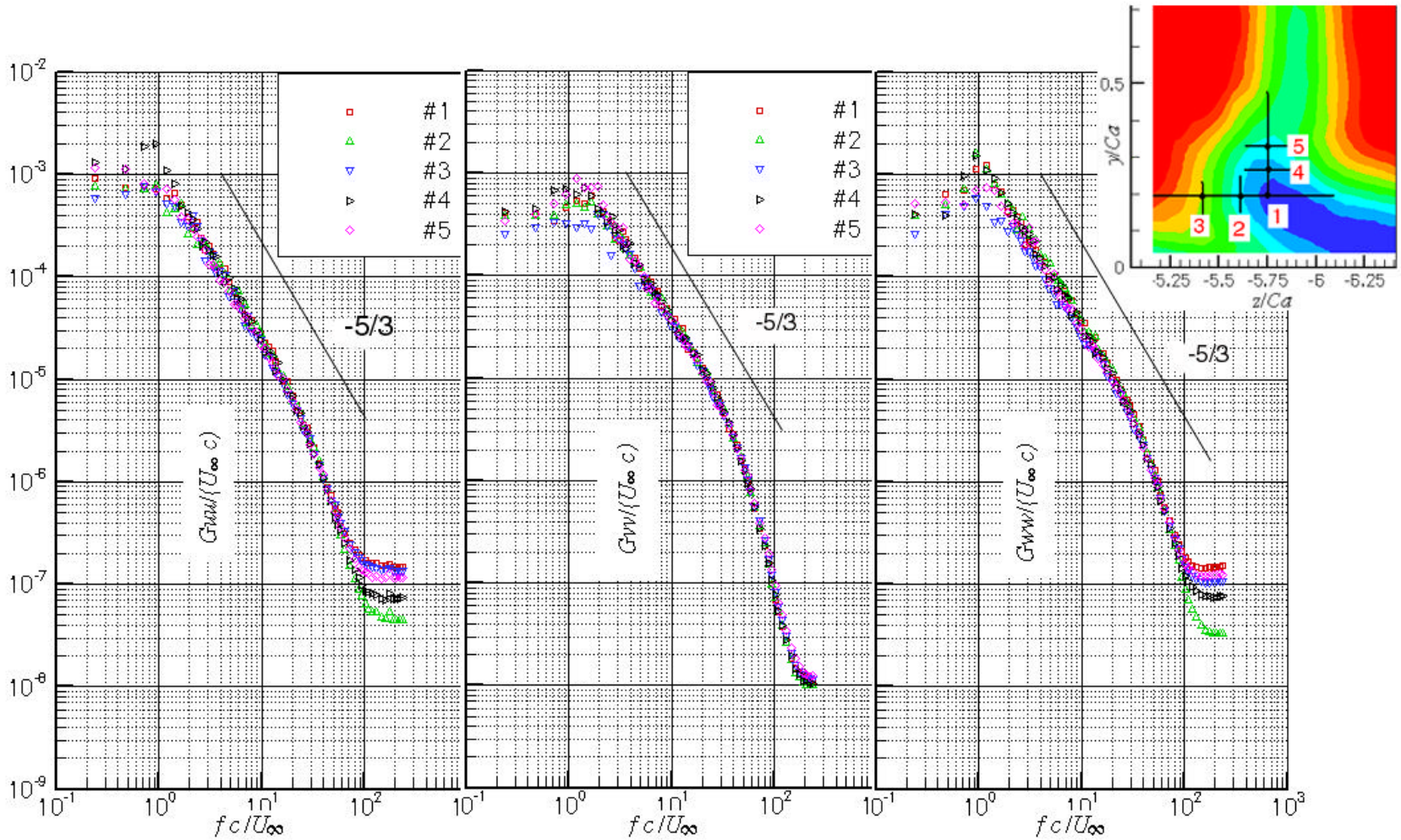

Figure 3-26 Autospectra at *x/Ca = 3.75*

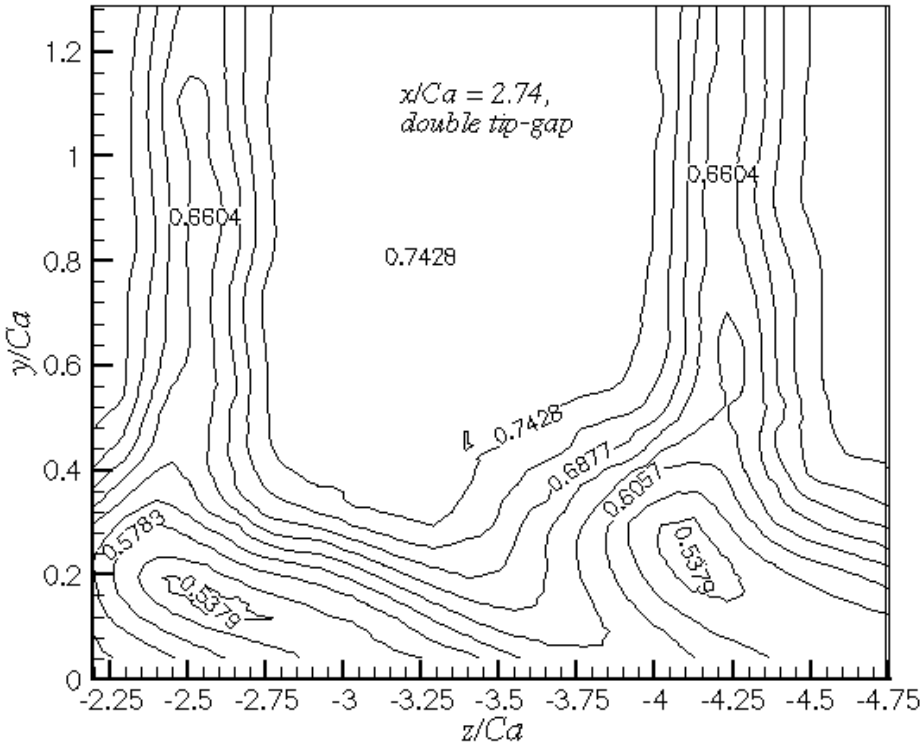

(a)

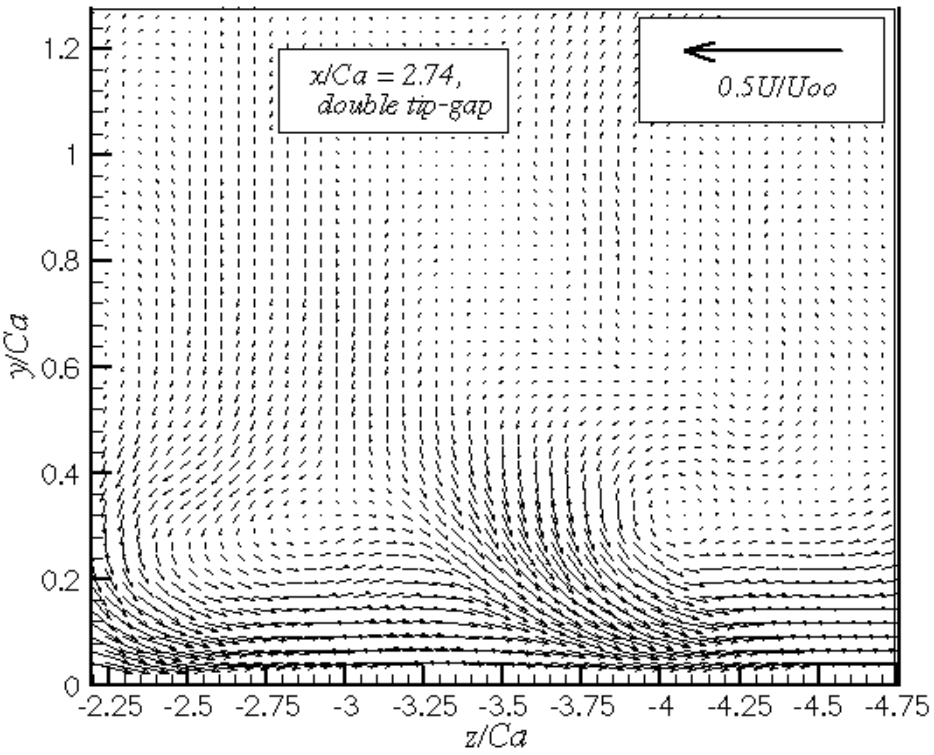

(b)

Figure 3-27 Mean Velocity with Double Tip Gap

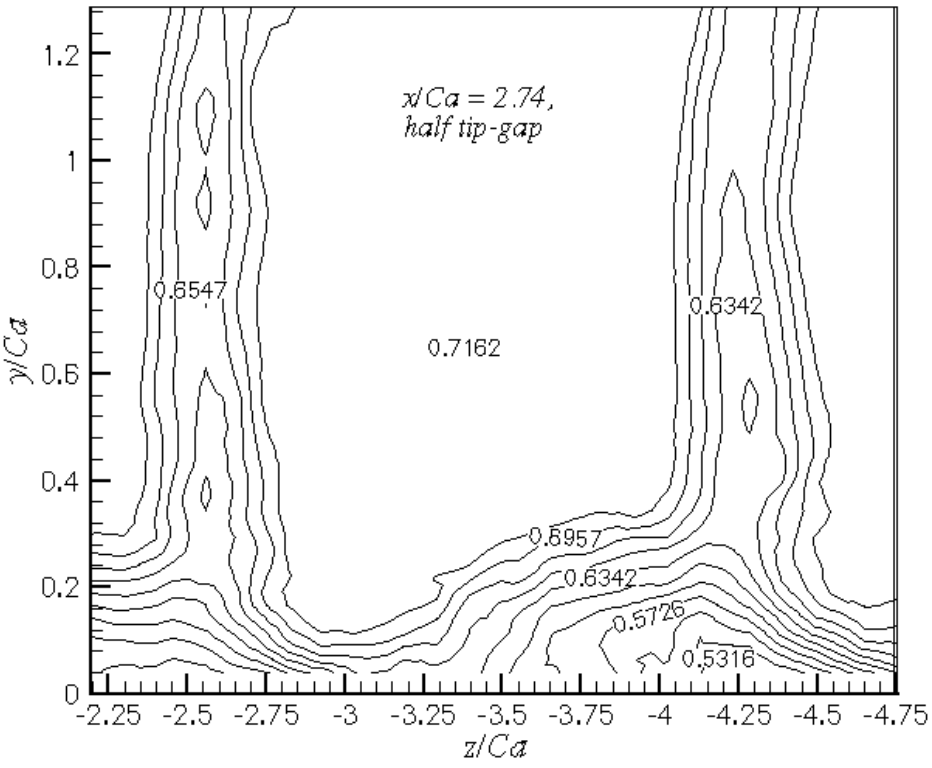

(a)

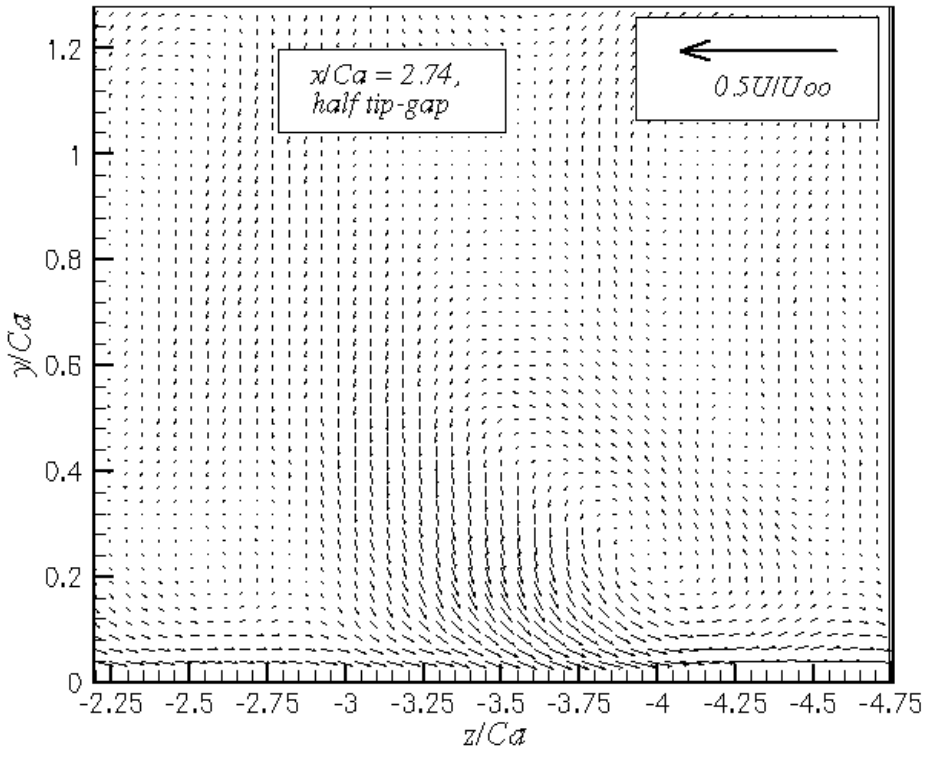

(b)

Figure 3-28 Mean Velocity with Half Tip Gap

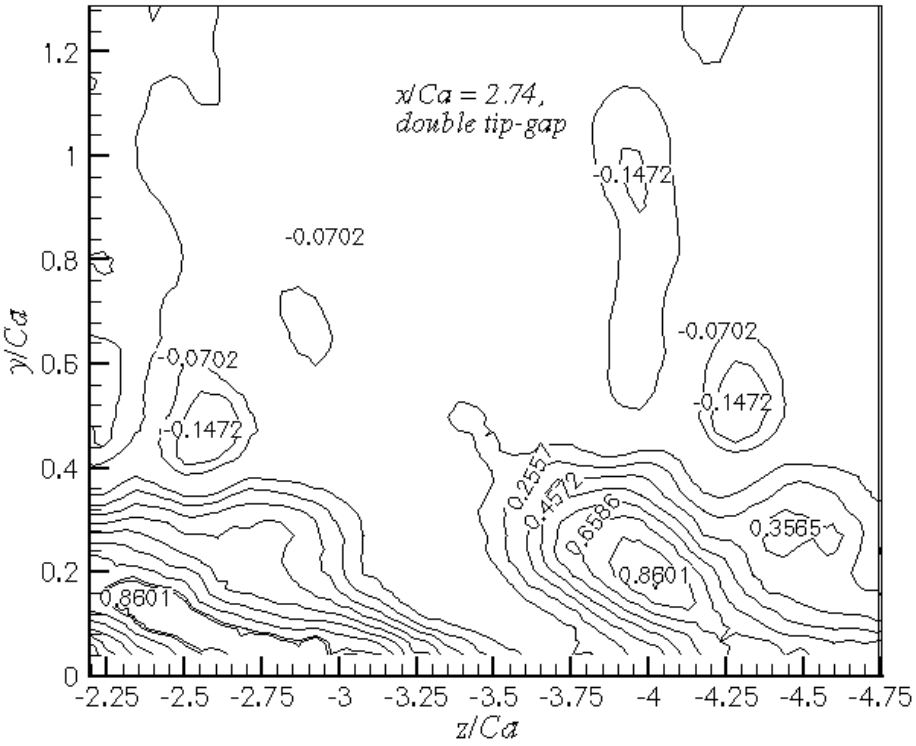

Figure 3-29 Mean Streamwise Vorticity at Double Tip Gap

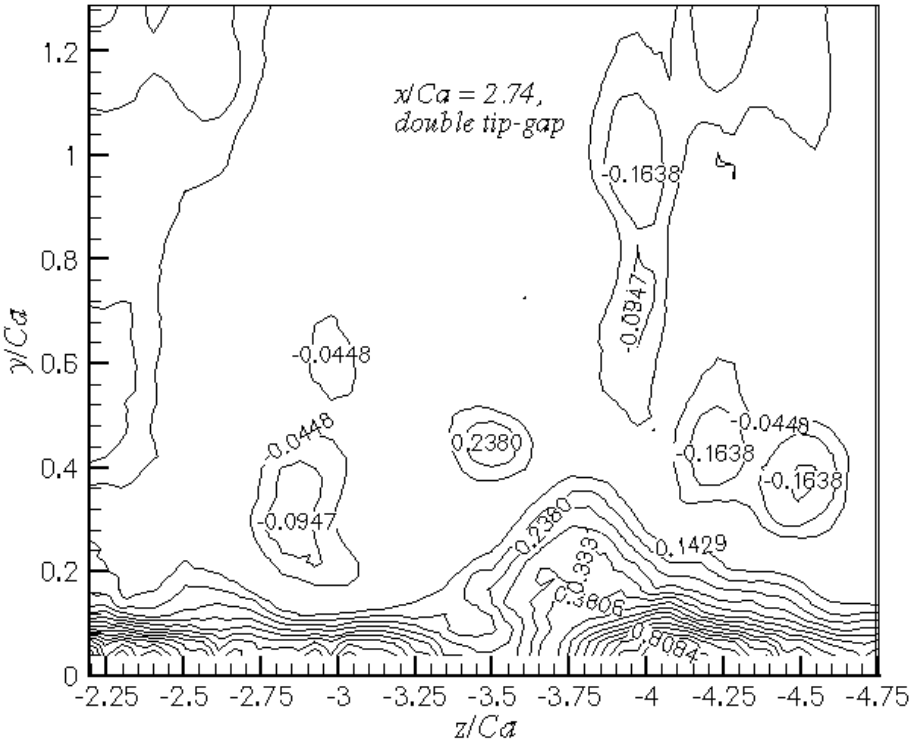

Figure 3-30 Mean Streamwise Vorticity at Half Tip Gap

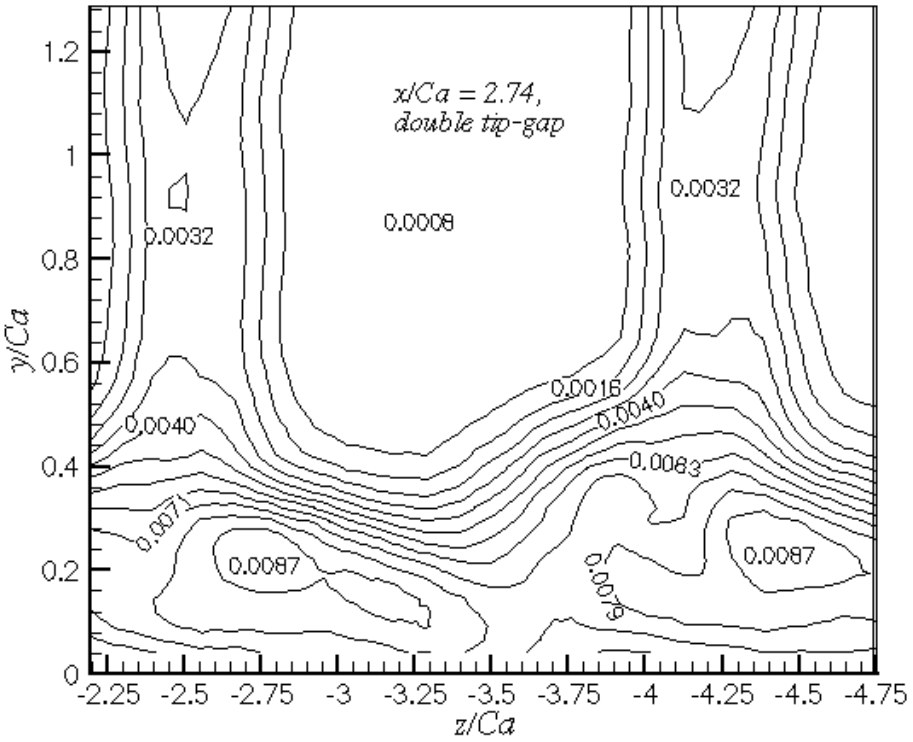

Figure 3-31 *tke* Distribution at Double Tip Gap (Normalized on U_∞^2)

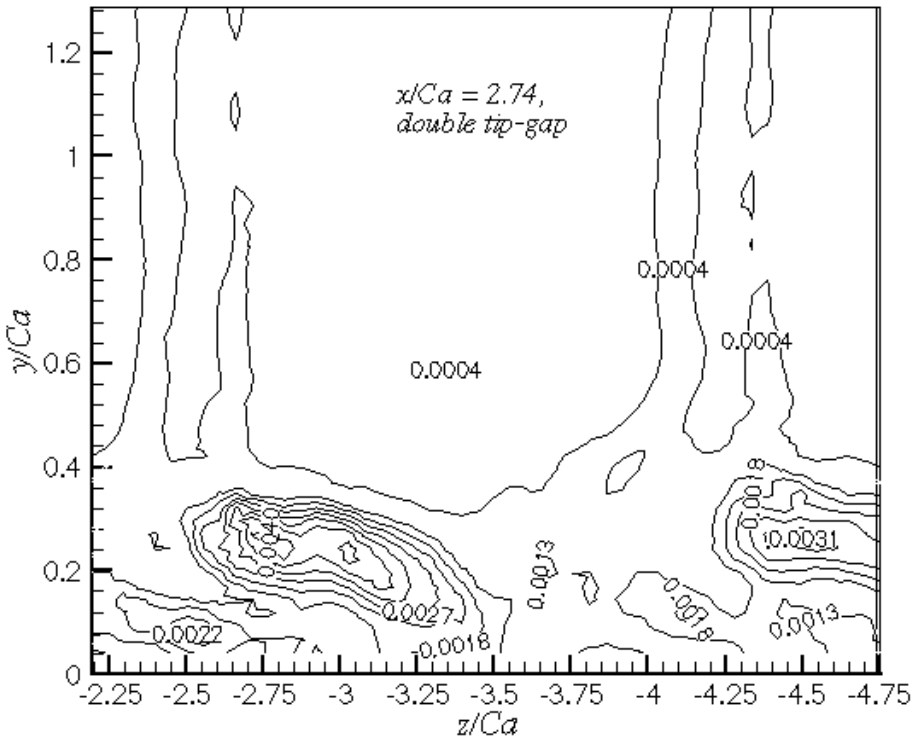

Figure 3-32 *tke* Production at Double Tip Gap (Normalized on U_∞^2)

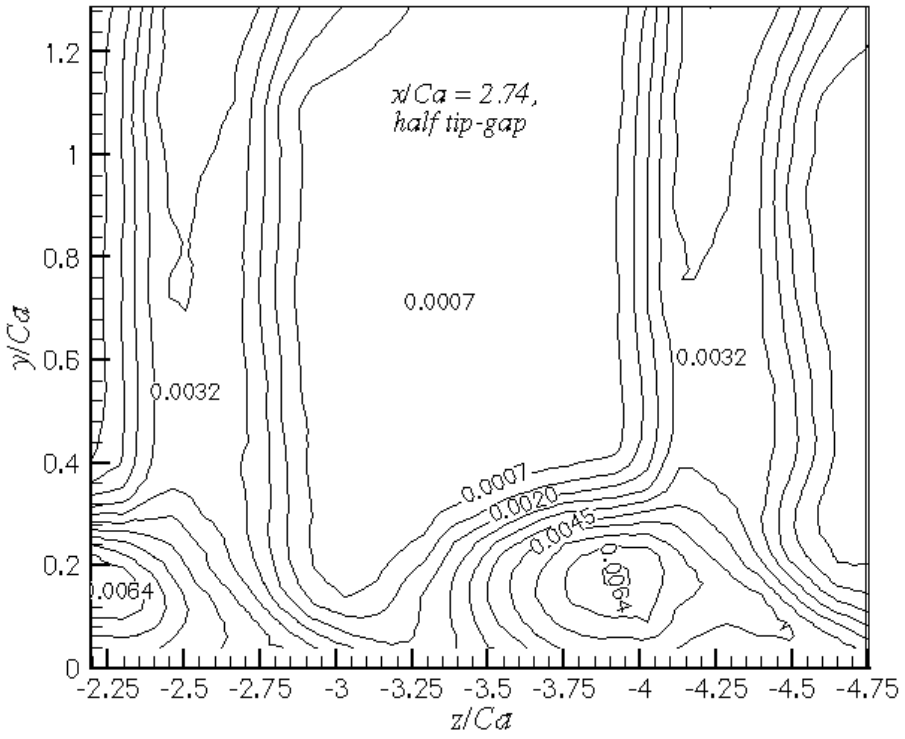

Figure 3-33 *tke* Distribution at Half Tip Gap

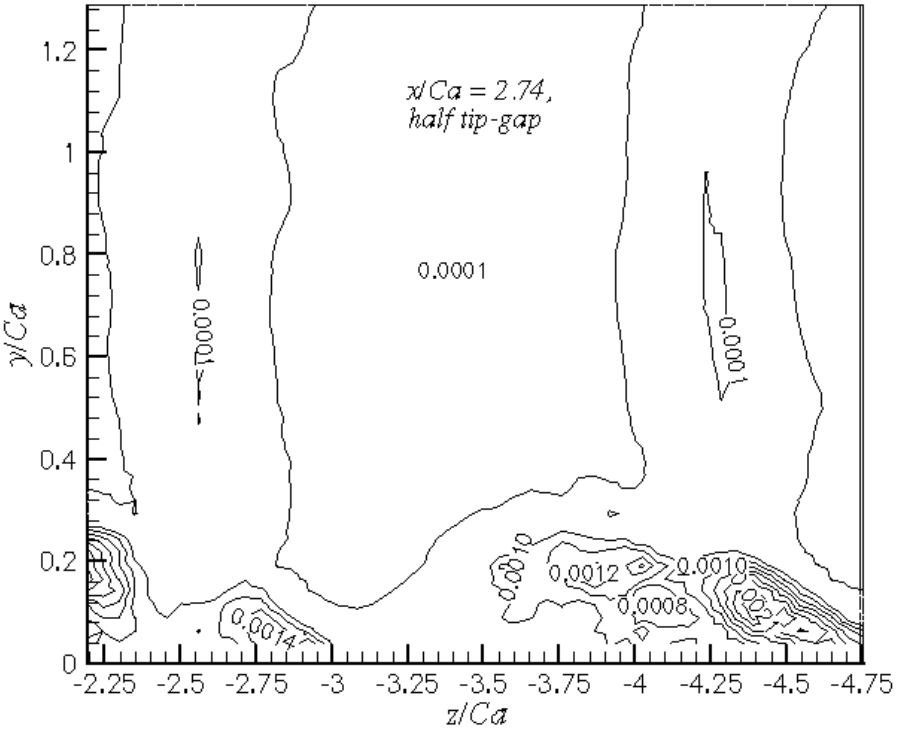

Figure 3-34 *tke* Production at Half Tip Gap

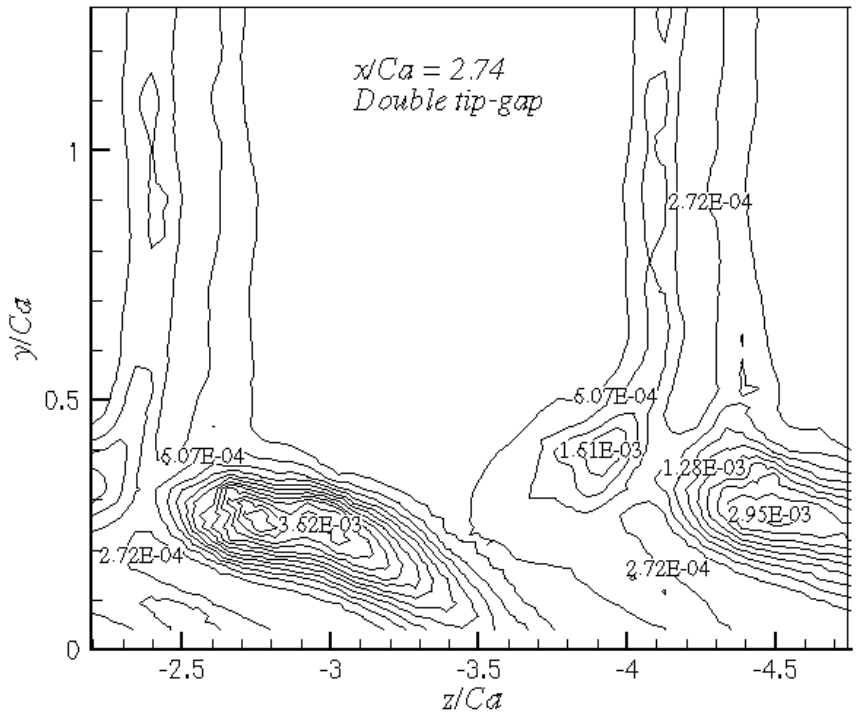

(a) Streamwise Contribution

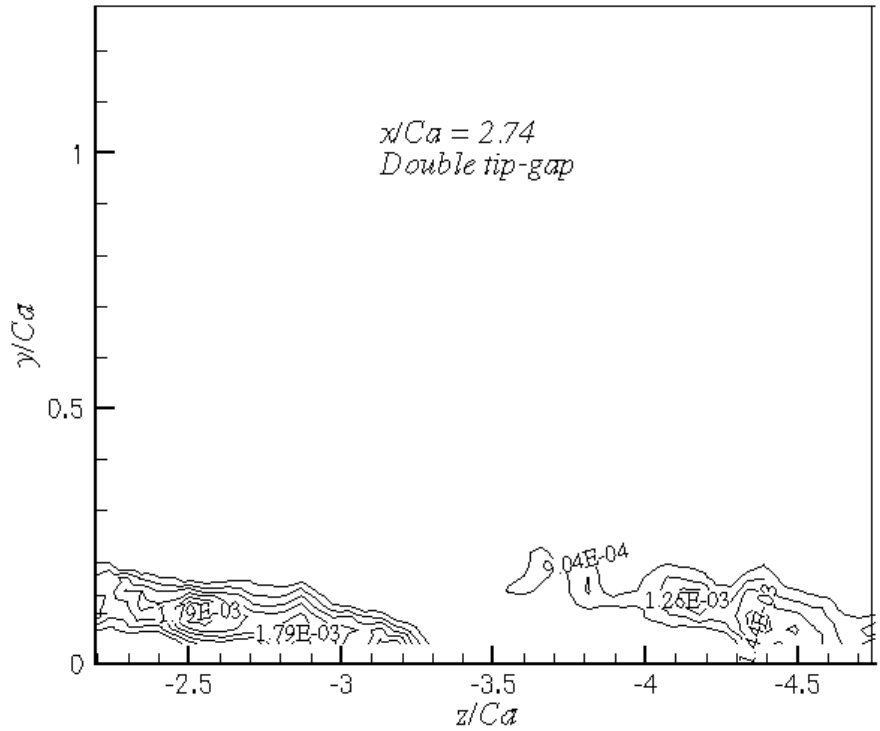

(b) Crossflow Contribution

Figure 3-35 Streamwise and Crossflow Contributions to tke production at $x/c_a = 2.74$, Double Tip Gap

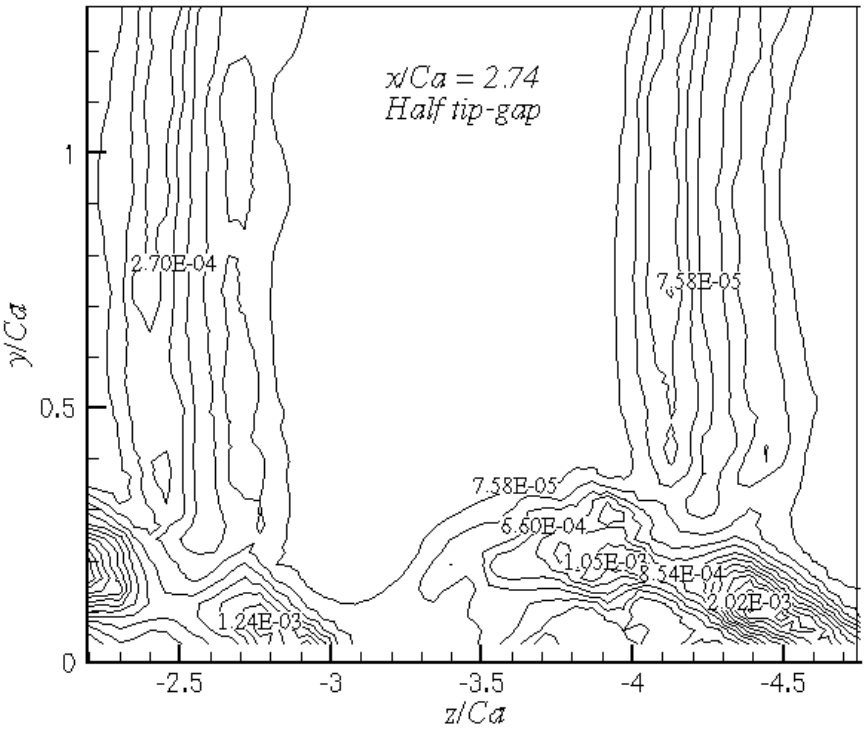

(a) Streamwise Contribution

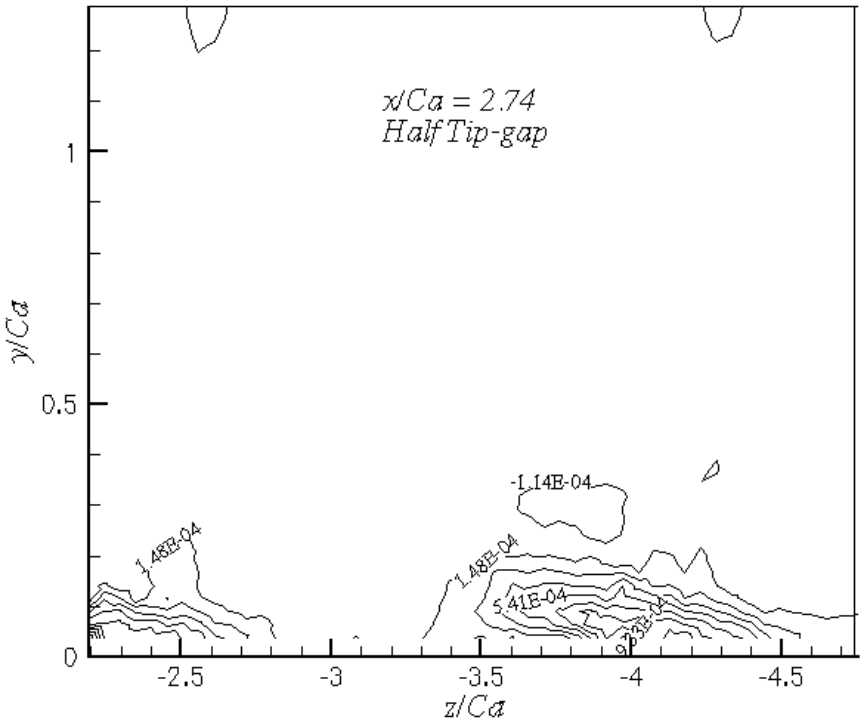

(c) Crossflow Contribution

Figure 3-36 Streamwise and Crossflow Contributions to tke production at $x/c_a = 2.74$, Half Tip Gap

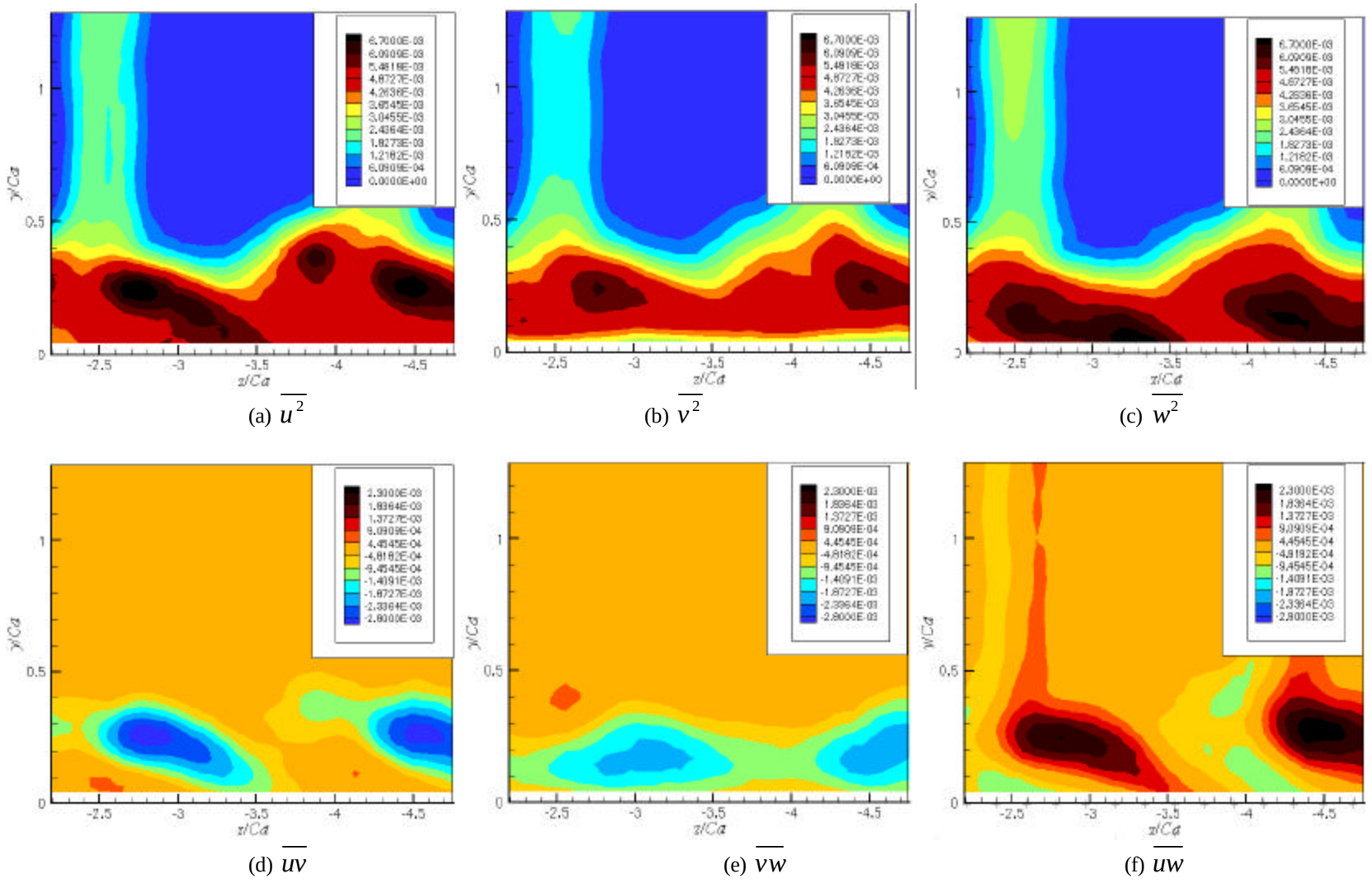

(a) $\overline{u^2}$ (b) $\overline{v^2}$ (c) $\overline{w^2}$

(d) $\overline{uv}$ (e) $\overline{vw}$ (f) $\overline{uw}$

Figure 3-37 Reynolds Stress Components at Double Tip Gap

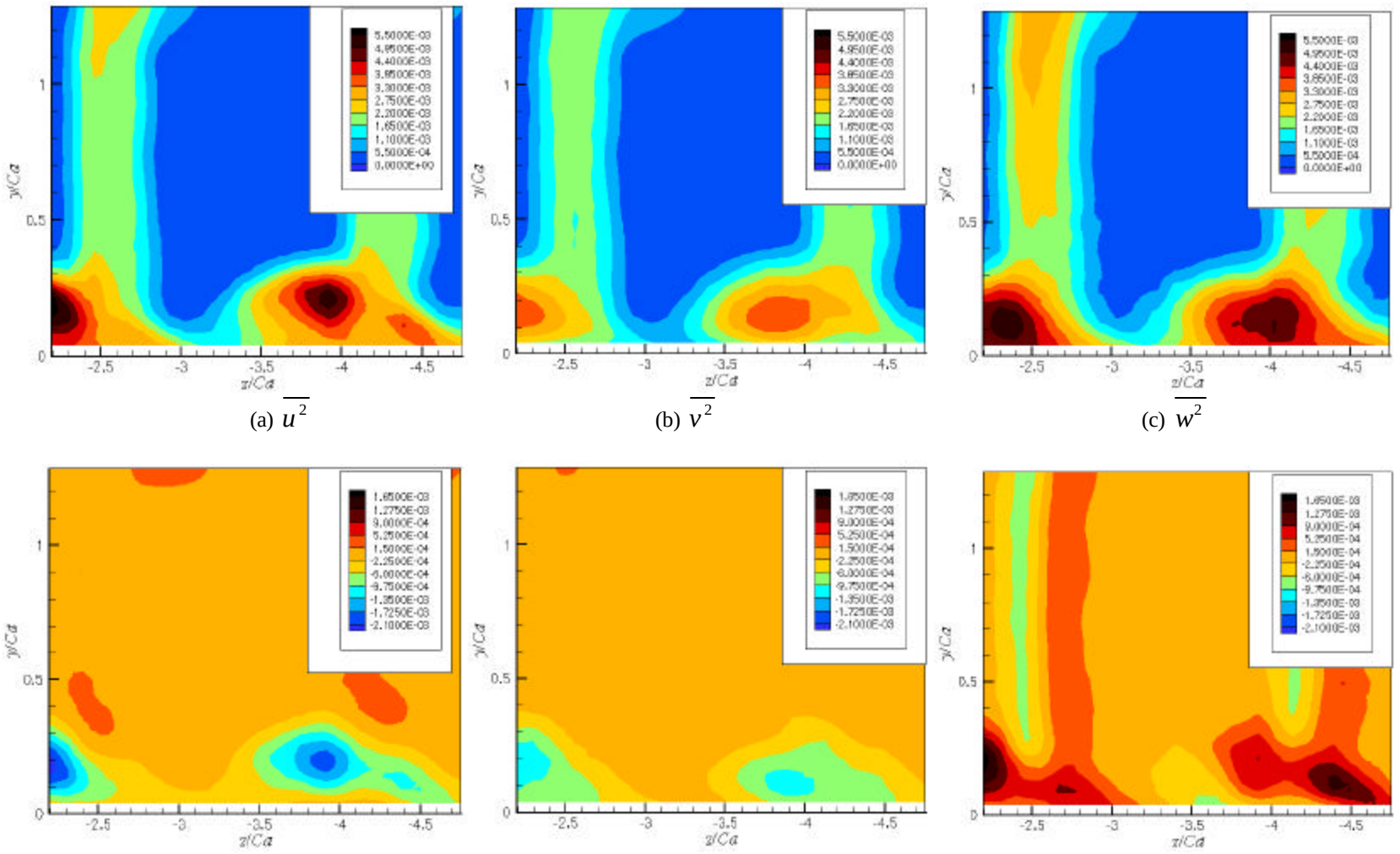

(a) $\overline{u^2}$ (b) $\overline{v^2}$ (c) $\overline{w^2}$

(d) $\overline{uv}$ (e) $\overline{vw}$ (f) $\overline{uw}$

Figure 3-38 Reynolds Stress Components at Half Tip Gap

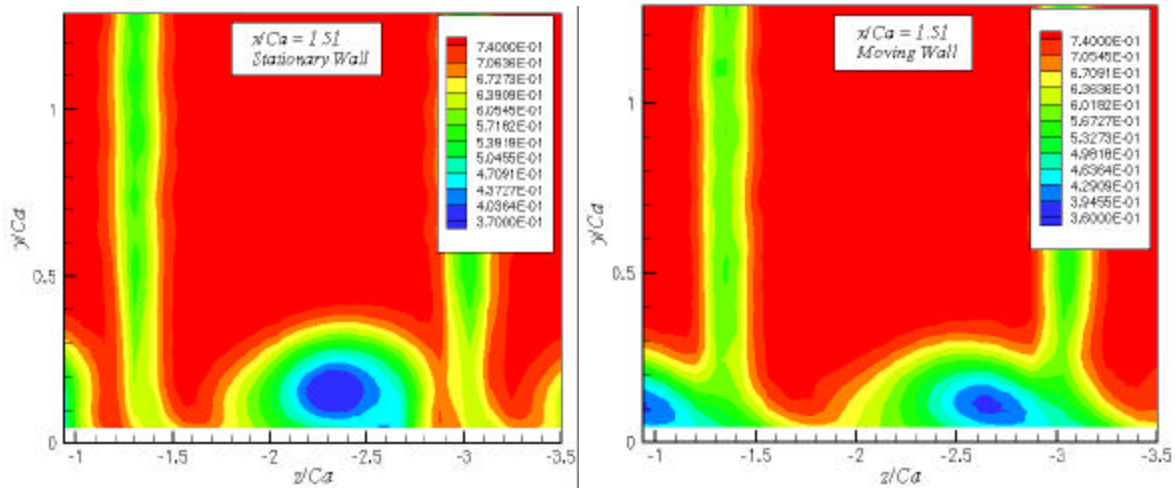

Figure 3-39 Comparison Mean stream Velocity contour at *x/Ca =1.51*

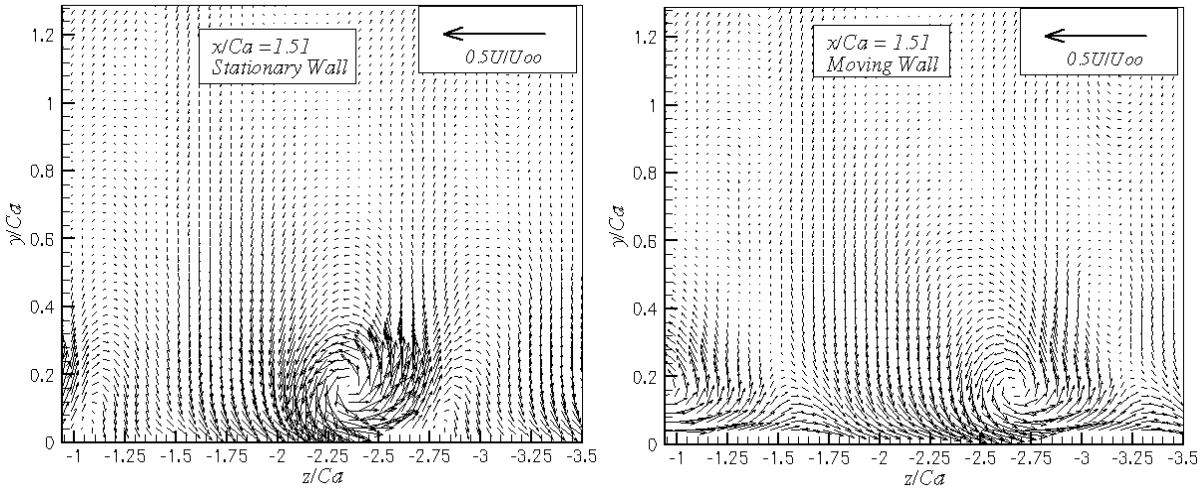

Figure 3-40 Comparison of Crosswise Velocity Vector at *x/Ca =1.51*

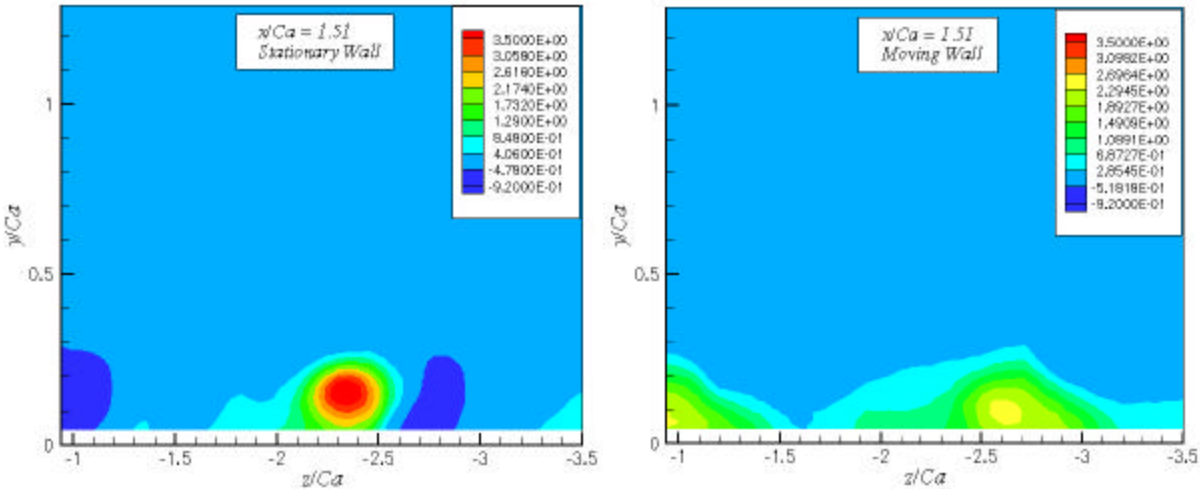

Figure 3-41 Comparison of Mean Streamwise Vorticity at *x/Ca =1.51*

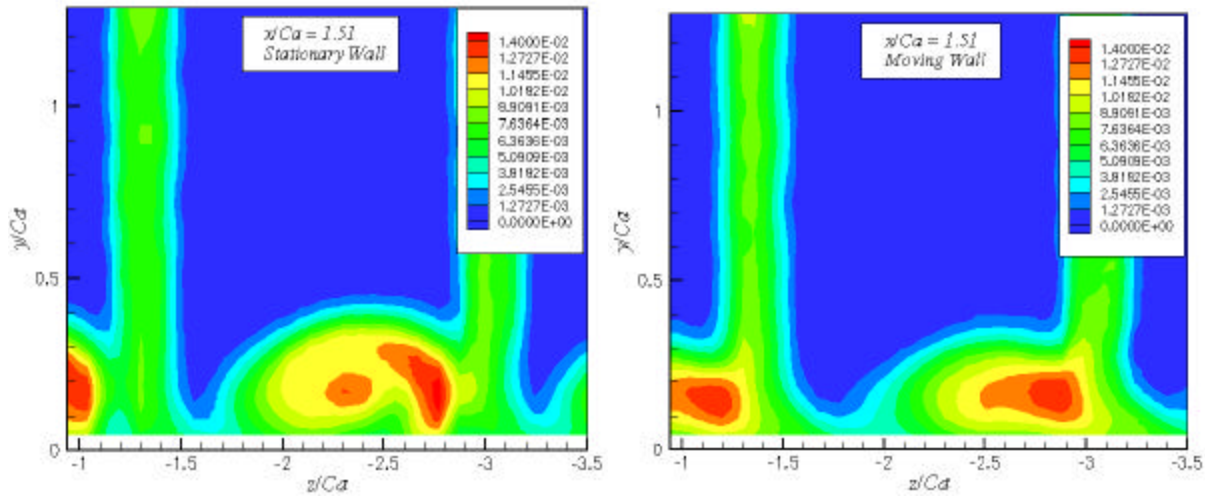

Figure 3-42 Comparison of *tke* Contour at *x/Ca=1.51*
(Normalized on U_∞^2)

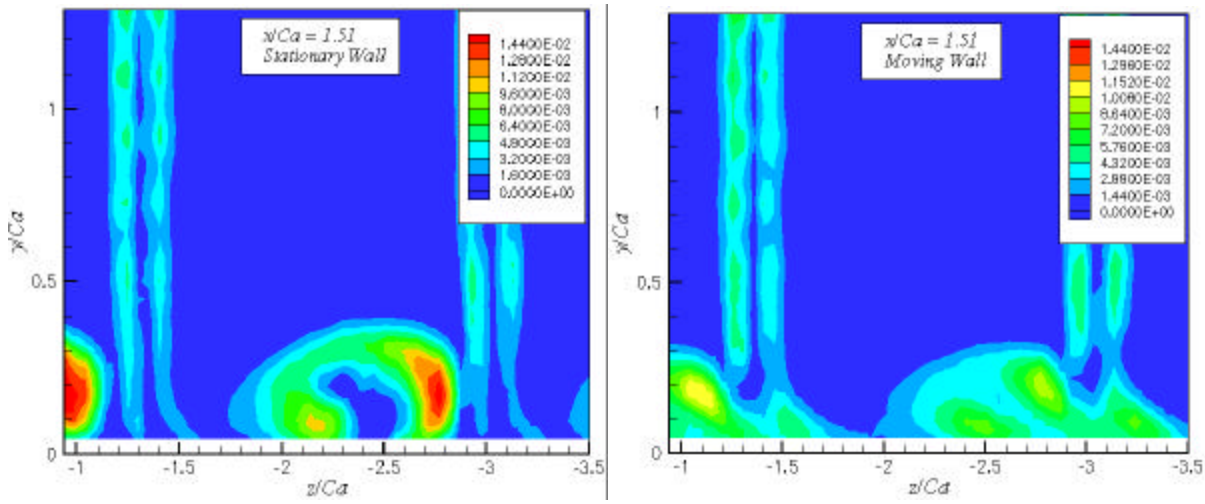

Figure 3-43 Comparison of *tke* production *at x/Ca =1.51*
(Normalized on U_∞^2)

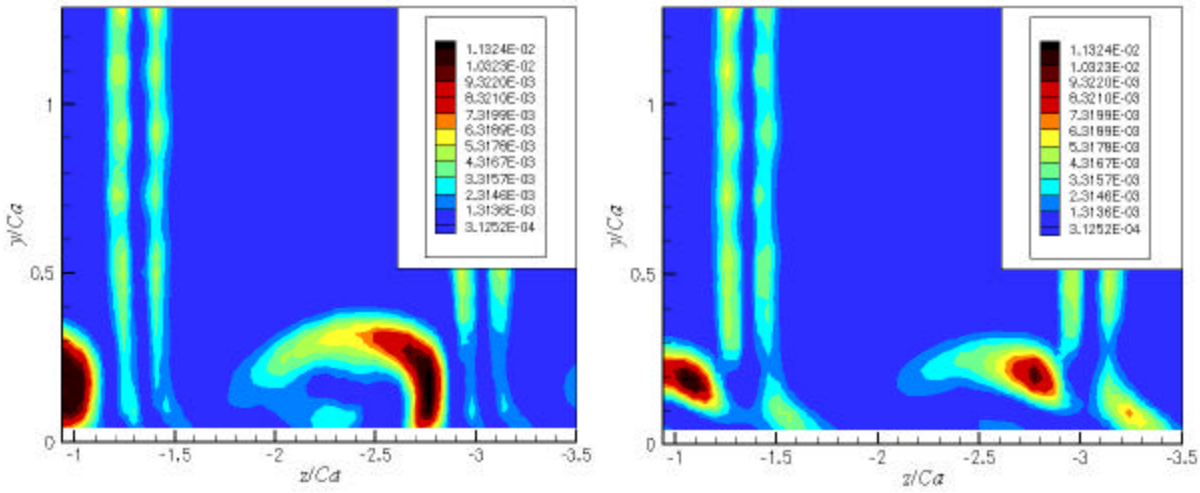

Statinary Wall Moving Wall

(a) Streamwise Contribution

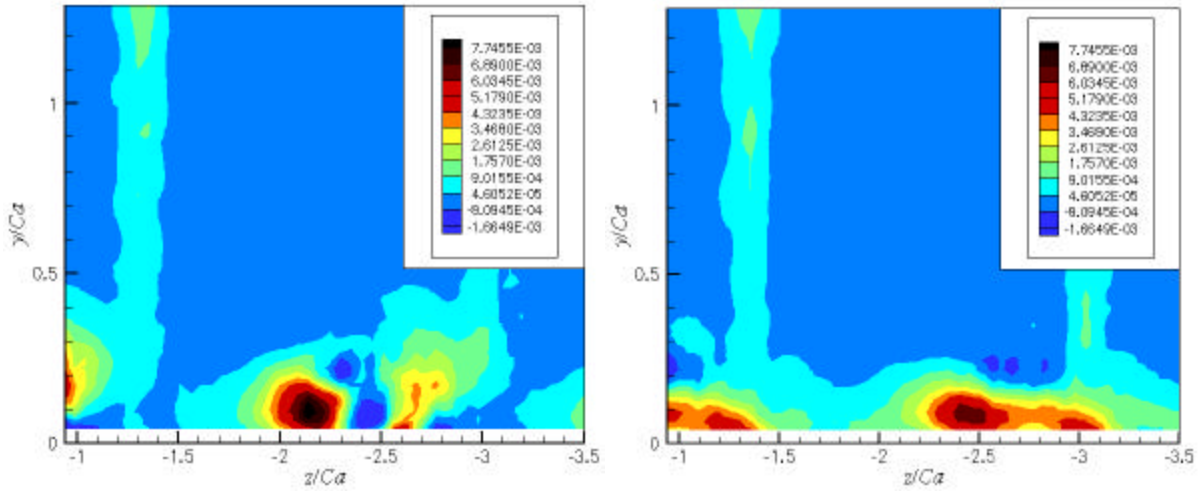

Statinary Wall Moving Wall

(b) Crossflow Contribution

Figure 3-44 Streamwise and Crossflow Contributions to tke production at $x/c_a = 1.5$

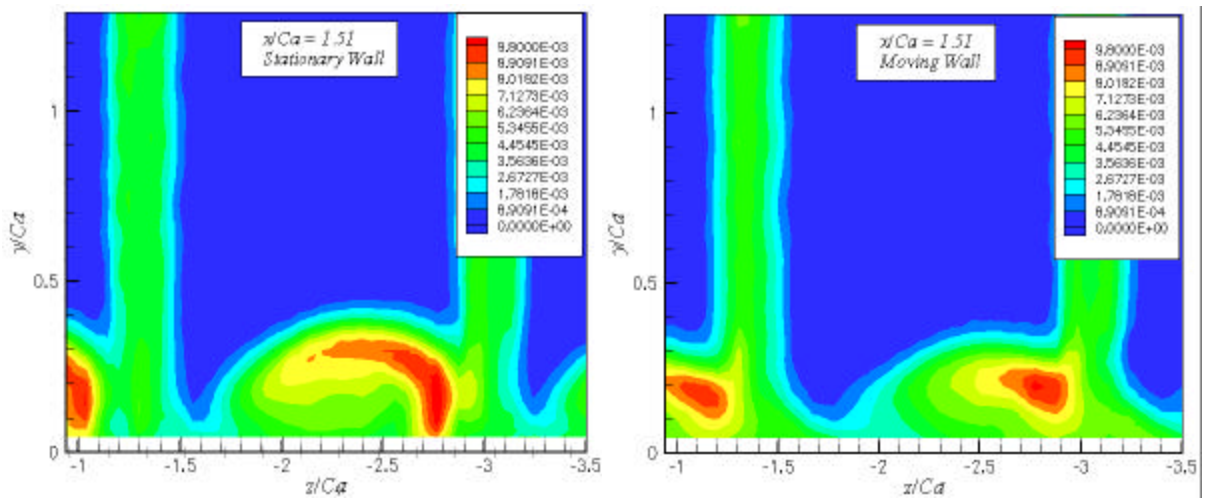

(a) $\overline{u^2}$

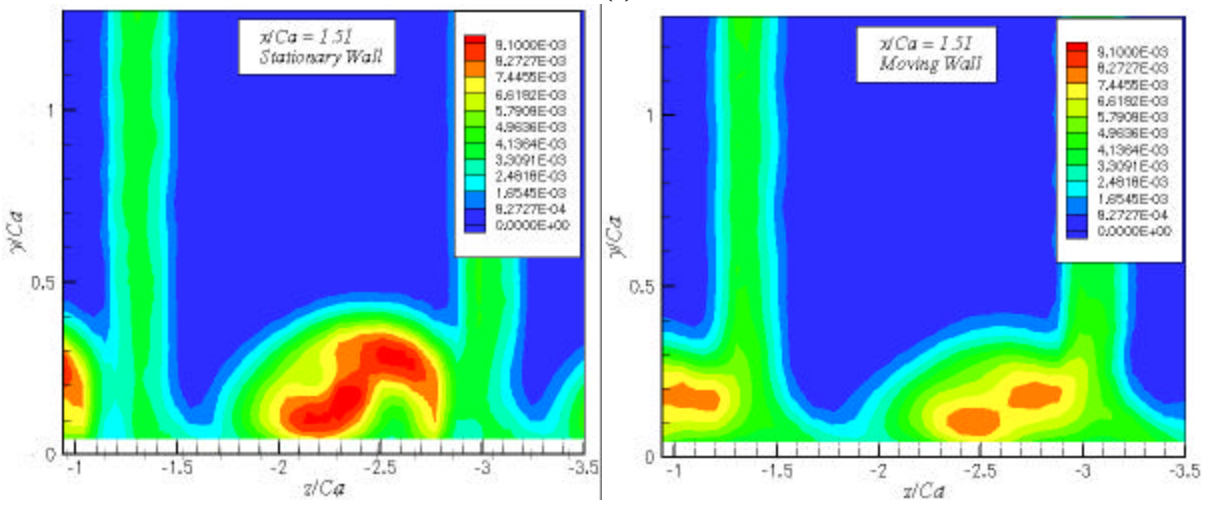

(b) $\overline{v^2}$

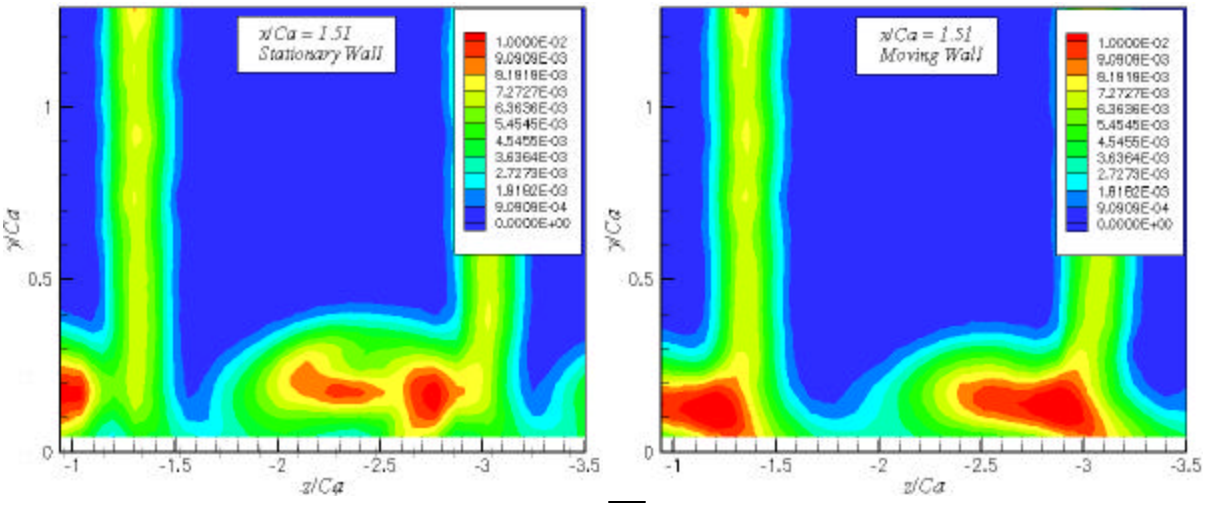

$\overline{w^2}$

Figure 3-45 Comparison of Reynolds Normal stress at *x/Ca=1.51*

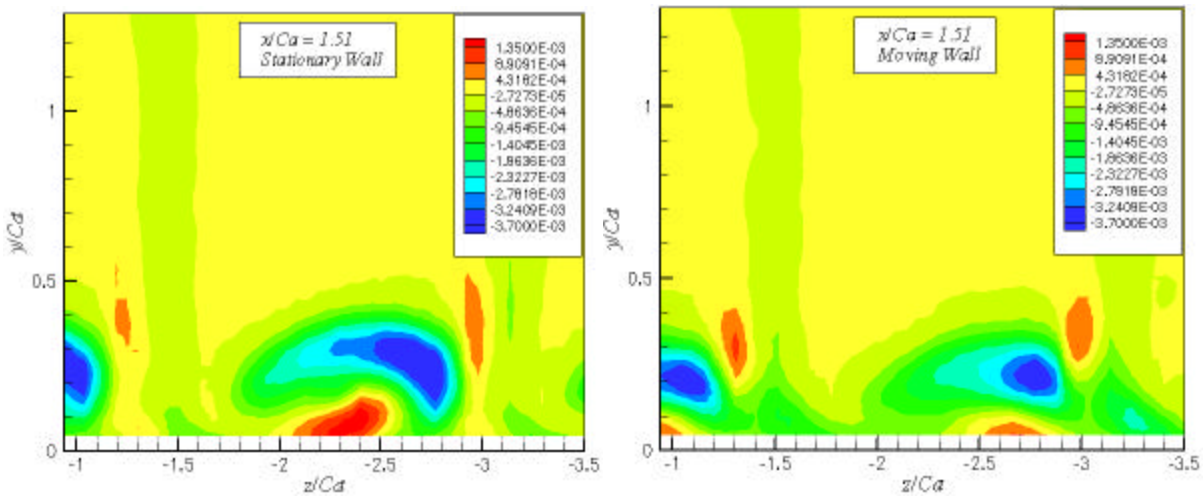

(a) $\overline{uv}$

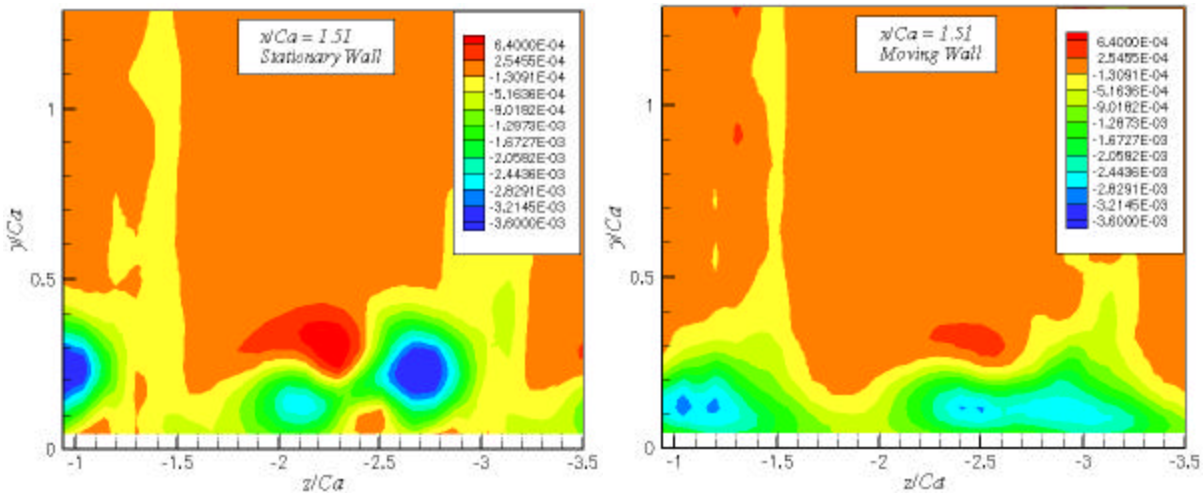

(b) $\overline{vw}$

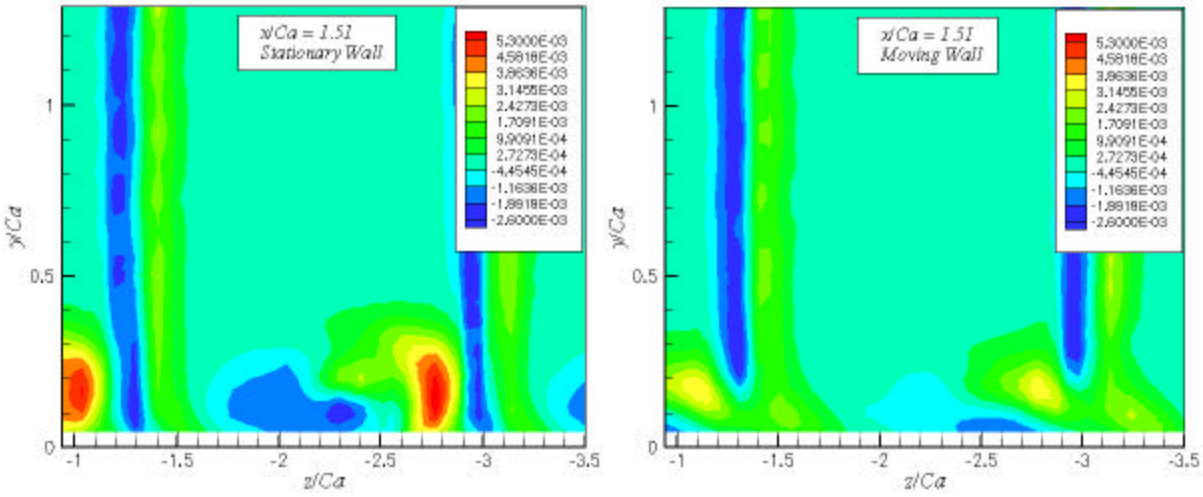

(c) $\overline{uw}$

Figure 3-46 Comparison of Reynolds Shear Stress *at x/Ca = 1*

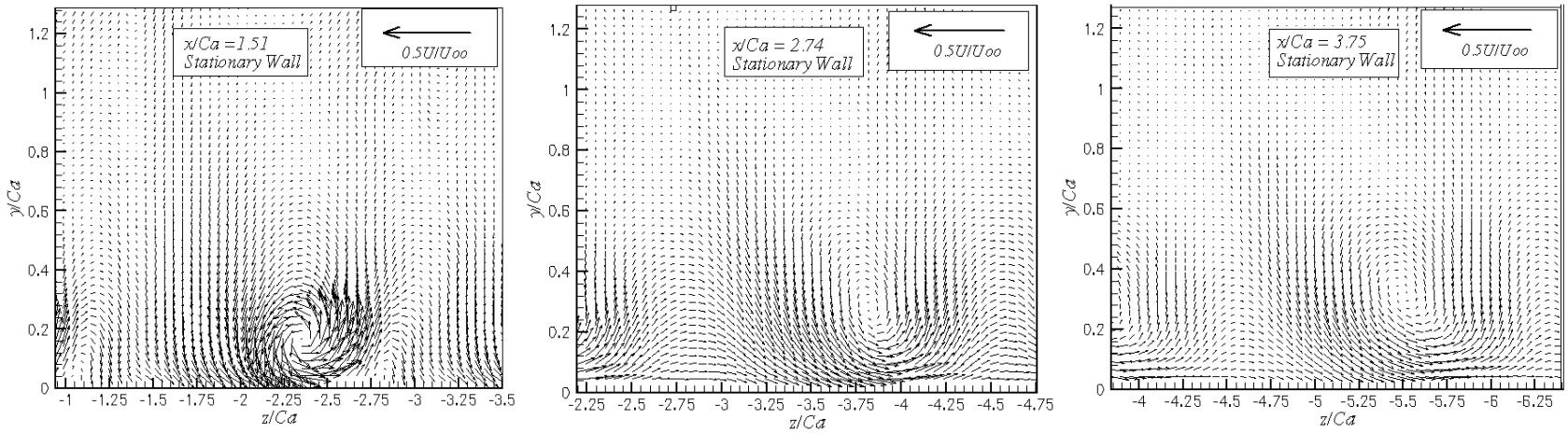

(a) With Stationary Wall

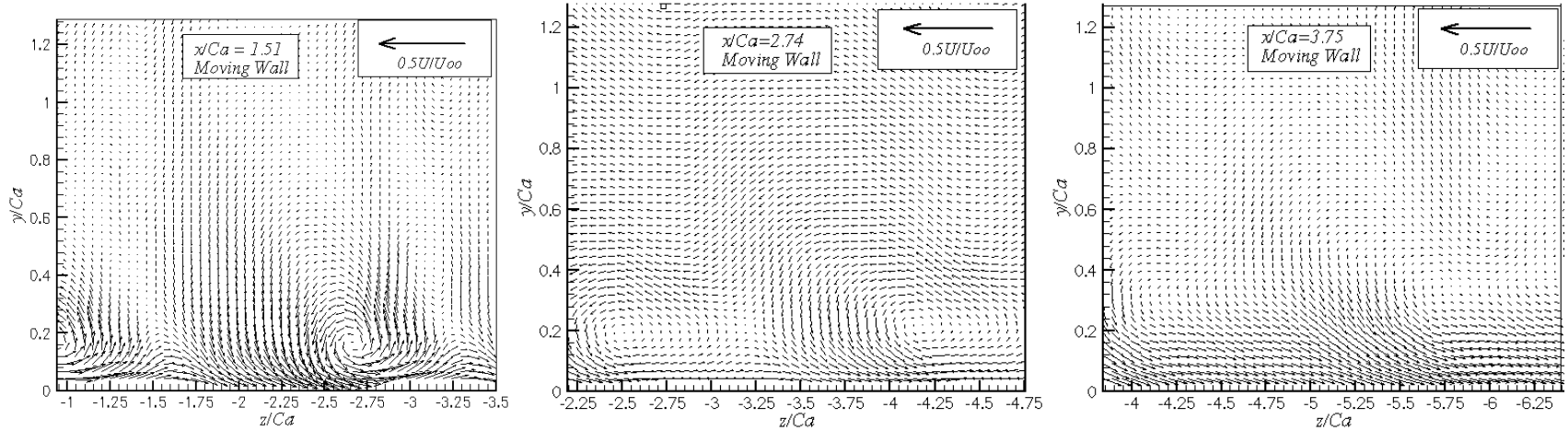

(b) With Moving Wall

Figure 3-47 Development of Crosswise Ve locity

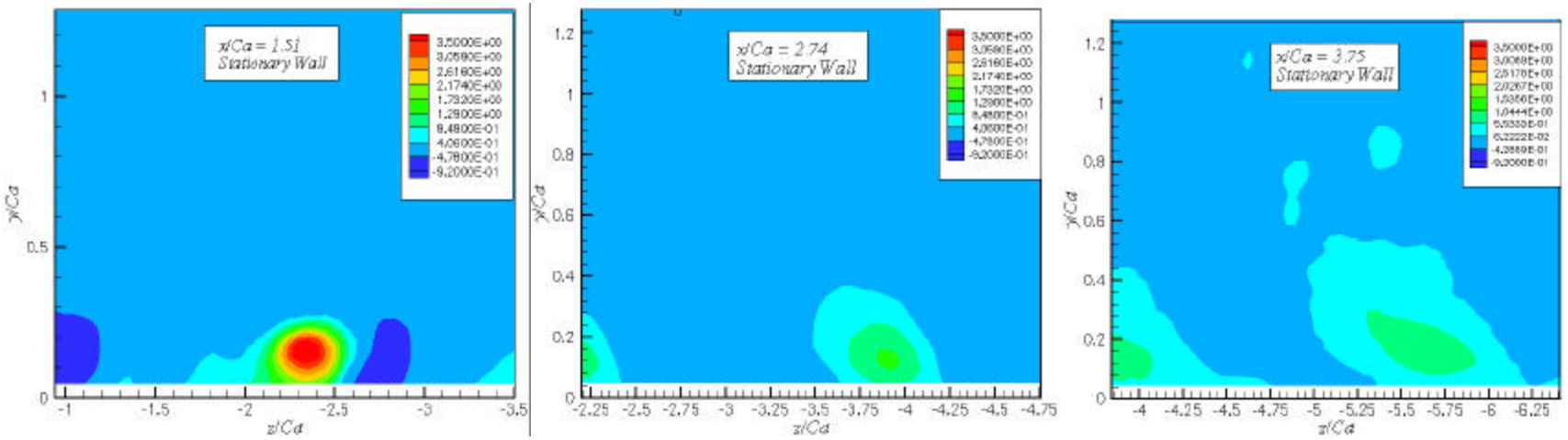

(a) With Stationary Wall

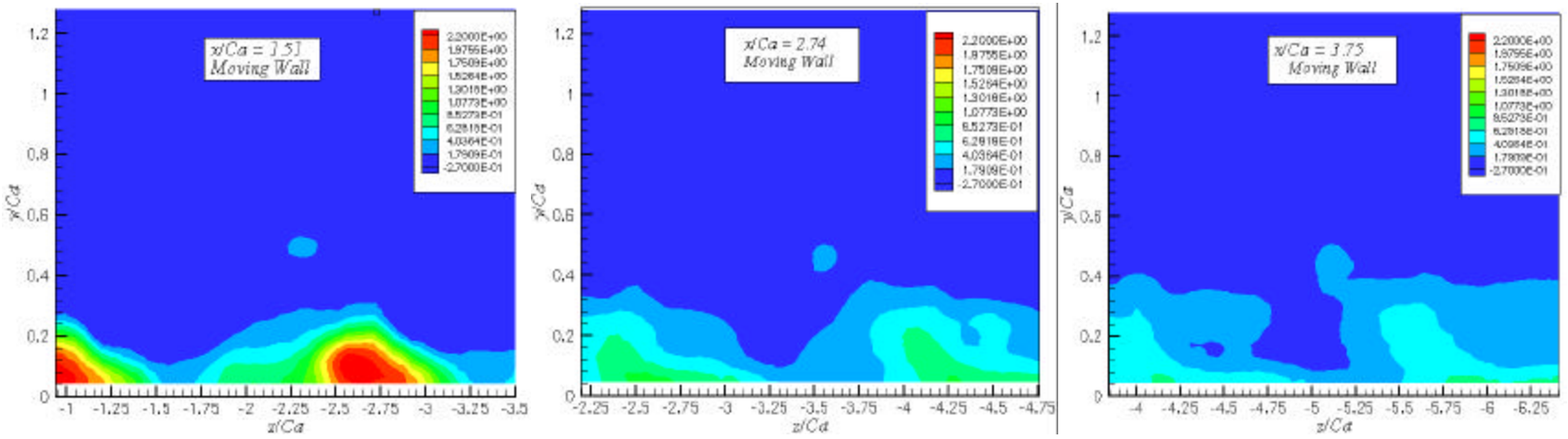

(b) With Moving Wall

Figure 3-48 Development of Mean Streamwise Vorticity

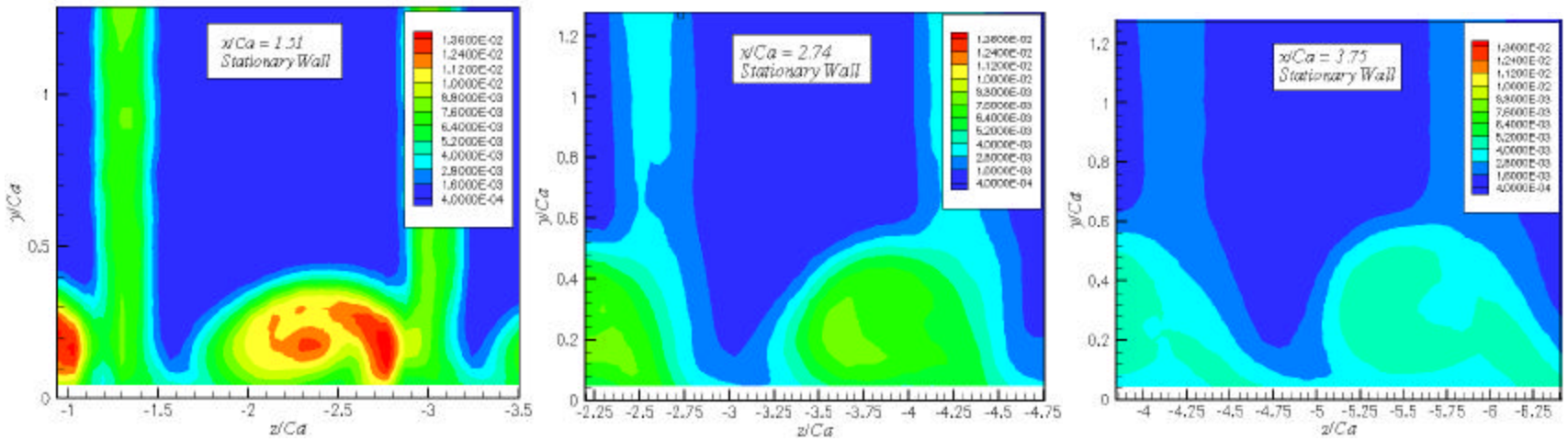

(a) With Stationary Wall

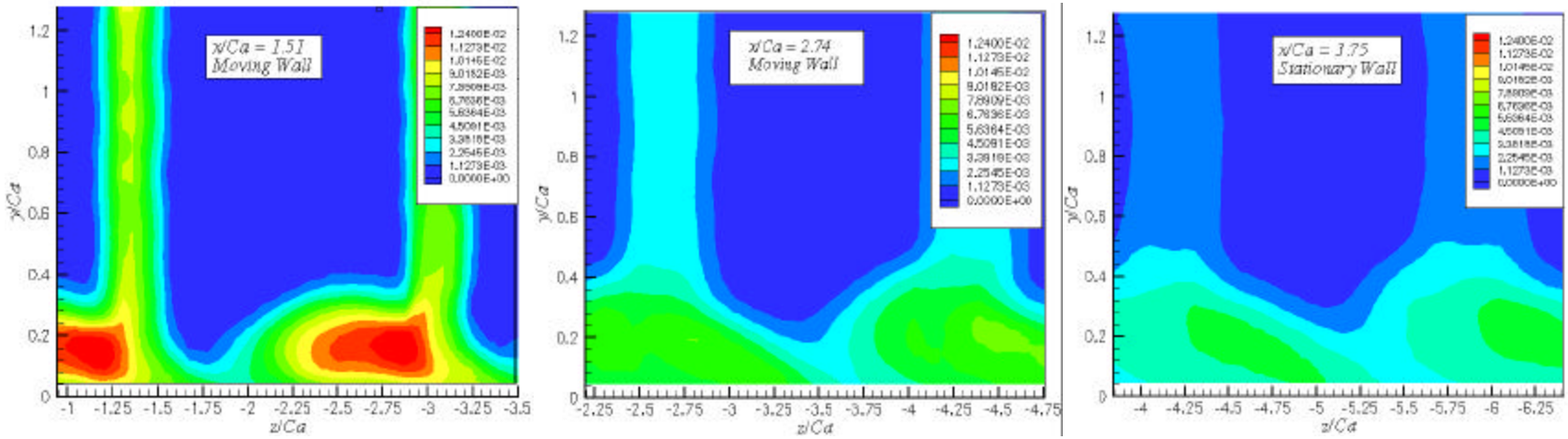

(b) With Moving Wall

Figure 3-49 Development of *tke* (Normalized on U_∞^2)